universität wien

MASTERARBEIT / MASTER'S THESIS

Titel der Masterarbeit / Title of the Master's Thesis

„Self-Consistent Quantum Tomography - An Experimental Analysis“

verfasst von / submitted by

Florian Robert Schlederer, BSc

angestrebter akademischer Grad / in partial fulfilment of the requirements for the degree of

Master of Science (MSc)

Wien, 2018 / Vienna, 2018

Studienkennzahl lt. Studienblatt / degree programme code as it appears on the student record sheet:	A 066 876
Studienrichtung lt. Studienblatt / degree programme as it appears on the student record sheet:	Masterstudium Physik
Betreut von / Supervisor:	Univ.- Prof. Dipl.-Ing. Dr. Philip Walther

Acknowledgments

It was Nakamura-Sensei's readiness to invite me to his laboratories at the RCAST, University of Tokyo, that made my ambition to write this thesis about superconducting qubits come true. His character is well-portrayed by the members of his research group: Sugiyama-San, whose structured working brought light into many obfuscations; Dany, who patiently answered the questions that others would not hear; Kono-San, on whose shoulders the experimental accuracy of my work resides; Tamate-San, who would share excitement about good experimental data after a long day; Akhil and Arnaud, with whom discussions were frequently philosophical and always rewarding; and Yamazaki-San, who sensed the perfect timing for encouragement. To all of you arigatou gozaimasu!

Equally important for the feasibility of this project was Prof. Philip Walther. He never hesitated to support my plans of going to Japan and being supervised from afar. Such flexibility makes unusual ideas and their realization possible and I am very grateful for his trust in me.

At this point, I want to thank all the spectacular teachers, who know how to bring talents to flourish and how to alleviate weaknesses. I was very fortunate to have had many of them, amongst whom my parents were the most important ones. A child can wish for nothing more then the freedom to pursue its own dreams, wherever they lie, and being loved while doing so.

Above all, the group of humorous thinkers, curious minds and faithful companions, which I am allowed to call friends, deserves my deepest gratitude. Exploring the riddles of physics, life and love with you together, has made this past years such a memorable time. Who, but you, should be mentioned here? Kathi, Claudia, Thomas, Martin, Georg, Tobias, Simon, Annie and Hanja, thank you for much more than this section offers to express.

"Like all young men I set out to be a genius,
but mercifully laughter intervened."

Lawrence Durrell in *Clea*

Abstract

Improving accuracies of quantum operations is an indispensable task for realizing a practical quantum computer. A reliable characterization method of a quantum operation is necessary to achieve that. Quantum tomography and randomized benchmarking are established means to do so, but because of high sensitivity to state preparation and measurement (SPAM) errors and multiple approximations, they lack evaluative power. Gate set tomography aims to overcome the issues by estimating the whole gate set consisting of initial state, quantum operations and measurement operators. Nonetheless, it lacks the simultaneous fulfillment of gauge-equivalence and physicality. The novel self-consistent quantum tomographic (SQCT) method, recently proposed by Sugiyama et al., *arXiv:1806.02696*, closes this deficit. The work in this thesis implements the new protocol using a transmon-type superconducting qubit. The method is contrasted to its predecessors, quantum process tomography, randomized benchmarking protocols and gate set tomography, in a detailed discussion of their respective advantage based on common quantum information processing parameters. The empirical outcome confirms many of the advantages of SCQT, but cannot to full extent reproduce the clear distinction that theory predicts for it.

Abstract

Zur Realisierung eines praktikablen Quantencomputers bedarf es Verbesserungen in der Genauigkeit von Quantenoperationen. Um das zu erreichen, ist eine verlässliche Methode zur Charakterisierung für solche Operationen unabdingbar. Quantentomographie und Randomized Benchmarking sind etablierte Methoden hierfür, vermissen jedoch evaluative Aussagekraft, bedingt durch ihre hohe Anfälligkeit für Präparations- und Messfehler (SPAM Error) und diverse Approximationen. Gate Set Tomographie zielt darauf ab, die Missstände durch eine Bestimmung des kompletten Sets an Operationen, das sind Anfangszustand, Quantenoperationen und Messoperatoren, zu beheben. Nichtsdestotrotz, sind Eichäquivalenz und Physikalität des Resultats nicht gewährleistet. Die jüngst von Sugiyama et al., *arXiv:1806.02696*, entwickelte Selbst-konsistente Quantentomographie (SCQT) schließt dieses Defizit. Die vorliegende Arbeit implementiert das neue Protokoll in einem supraleitenden Qubit des Transmontyps. Das Protokoll wird mit seinen Vorgängern, Quantentomographie, Randomized Benchmarking Protokolle und Gate Set Tomographie, kontrastiert und in einer detaillierten Diskussion auf Basis gängiger Parameter der Quanteninformationsverarbeitung analysiert. Die empirischen Resultate bestätigen viele der Vorteile von SCQT, können ihre klare theoretische Überlegenheit jedoch nicht zur Gänze reproduzieren.

Contents

Chapter 1 Introduction

The quantum computer is one of the most compelling technologies our current age is trying to engineer, merging the fields of quantum physics and computer science. It is expected to advance unstructured database searches [1], prime factorization [2], which plays a big role in today's information security, and the simulation of other complex quantum systems [3–5]. Albeit such revolutionary applications draw much attention, general quantum computing devices are going to spur a deeper understanding of quantum theory, which has maintained many of its counterintuitive mysteries since its development a century ago [6].

For years, experimental error rates of quantum operations have been detrimental to quantum protocols. As error rates approach the fault-tolerance threshold of a quantum error correction code [7], reliable characterization methods for quantum operations become essential, not only for validation of the implemented operations, but also for improving their accuracy further. This growing research field in the topos of quantum computation is referred to as quantum characterization, verification and validation (QCVV), recognized as one of the key elements towards full-fledged quantum information processing [8, 9]. There exist already several protocols: Quantum tomography, comprising quantum state tompography (QST) [10–14], quantum process tomography (QPT) [15, 16] and positive-operator valued measure (POVM) tomography [17], randomized benchmarking (RB) [18–22] and gate set tompography (GST) [23–25] have gained widespread acceptance and use, but they lack certain theoretical requirements or the ability to provide the range of necessary parameters.

The recently proposed self-consistent quantum tomography (SCQT) by Sugiyama et al. [26] attempts to overcome these weak points by estimating the whole set of involved operations, called *gate set*, and not single operators or parameters. Such a self-consistent approach is also the basis of GST; SCQT's advance is a simultaneous gauge-fixing of the estimated gate set to a gauge-equivalent estimate and its truncation to the physical region, which is considered a shortcoming of GST.

The thesis is outlined as follows. The rudiments of quantum information theory are briefly outlined in Chap. 2, where the various characterization methods are treated in Sec. 2.5. To experimentally implement the novel quantum characterization scheme, a transmon-type superconducting qubit is used. A standard approach for modeling the Hamiltonian of the system is explained in Chap. 3. A description of the experimental setup is given

in Chap. 4. Before executing the actual characterization protocols, basic parameters of the superconducting qubit must be determined in standard experiments, whose results are presented in Chap. 5. After determining the basic parameters, the various characterization protocols QPT, IRB, GST and SCQT were executed. The results are shown in Chap. 6. They will be discussed on the basis of the quantum information processing parameters gate fidelity, error generators, physicality of the estimate, noise identification of unitary and amplitude damping errors in Chap. 7, where also a proof-of-principle experiment for single-shot readout is presented. After summarizing the findings in Chap. 8, a supplementary chapter provides additional explanation for Chap. 3 and lists the gate set estimates from GST and SCQT in more detail.

Chapter 2 Quantum Information

For decades, starting with a heedless vision by Richard Feynman in the early 80ies [3], researchers have been fascinated by the idea of exploiting the nature of quantum physics for information processing.

Most generally, a computer is a calculating device. In *classical* computers the most basic unit of information is a *bit*, a binary digit, either 0 or 1. One can (1) realize it by a switch being turned on/off or with the state of a transistor, where high and low resistance represent the two states. To use it for computation, methods to (2) reset a bit to some initial value, (3) maintain this value until it is (4) accessed for the manipulation of the computation and of course (5) read this information out are needed.

DiVincenzo established the same five criteria for a *qubit*, a quantum bit [27]. It is the basic information carrier of a *quantum* computer. In contrast to its classical counterpart the qubit has two extraordinary features: *superposition* and *entanglement*. Entanglement becomes important for systems with more than one qubit, whereas this thesis treats exclusively single qubits.

When one superposes the two states 0 and 1, one receives "states in between" or "both states at the same time", whichever interpretation of the quantum formalism is preferred. To work with these concepts, the mathematical formalisms necessary are introduced in the next section.

2.1 Mathematical Preliminaries

2.1.1 The Quantum State and the Hilbert Space

Quantum states are represented by vectors $|\psi\rangle$ in Hilbert space $\mathbf{H} = \mathbb{C}^d$, a complex d-dimensional vector space, also known as the state space. Naturally, for qubits the dimension is $d = 2$. An element $|\psi\rangle$ of $\mathbf{H}$ is well-defined up to a complex number of norm one (global phase) and can be written as

$$|\psi\rangle = \alpha|0\rangle + \beta|1\rangle, \tag{2.1}$$

where $\alpha, \beta \in \mathbb{C}$, with the normalization condition $|\alpha|^2 + |\beta|^2 = 1$. The state's information is not only stored in the ratio of the basis states $|0\rangle$ and $|1\rangle$, but also in the relative phase between them, as α and β are complex values. If this phase information is lost in the process of *decoherence*, the quantum features disappear too [28].

The probability of finding the state $|\psi\rangle$ in the state $|\chi\rangle$ is the squared absolute value of the overlap

$$P = |\langle\chi|\psi\rangle|^2, \tag{2.2}$$

with $\langle\chi|$ being an element of the isomorphic dual Hilbert space[1] $\mathbf{H}^*$. Whereas in classical theory probabilities are bilinear in the elements of the sample space representing state and outcomes, quantum probabilities are biquadratic. The expectation value for an observable $\hat{A}$ is

$$\langle\hat{A}\rangle = \langle\psi|\hat{A}|\psi\rangle. \tag{2.3}$$

The normalization reduces the number of parameters for a single qubit from four (two complex numbers) to three, which could be seen as a 3D-sphere condition

$$\alpha = e^{i\gamma}\cos\left(\frac{\theta}{2}\right) \quad \text{and} \quad \beta = e^{i(\gamma+\phi)}\sin\left(\frac{\theta}{2}\right). \tag{2.4}$$

As stated above, the global phase does not possess any physical meaning, thus the state $|\psi\rangle$ can be written with only two angular parameters θ and ϕ as

$$|\psi\rangle = \cos\left(\frac{\theta}{2}\right)|0\rangle + e^{i\phi}\sin\left(\frac{\theta}{2}\right)|1\rangle. \tag{2.5}$$

This facilitates the conception of a sphere's surface, where all pure quantum states lie, called the *Bloch sphere*. For a pure state, a measurement basis can be found that yields the expectation value +1. The two basis states

$$|0\rangle = \begin{pmatrix} 1 \\ 0 \end{pmatrix} \quad \text{and} \quad |1\rangle = \begin{pmatrix} 0 \\ 1 \end{pmatrix} \tag{2.6}$$

can be defined as north and south pole, respectively, constituting the z-axis, and the equator consists of all equal superpositions

$$|x\pm\rangle = \frac{1}{\sqrt{2}}\big(|0\rangle \pm |1\rangle\big) \quad \text{and} \quad |y\pm\rangle = \frac{1}{\sqrt{2}}\big(|0\rangle \pm i|1\rangle\big). \tag{2.7}$$

Measuring equal superpositions with a projective measurement along the z-axis yields 1/2 in all cases, according to Eq. (2.2). How is it then possible to distinguish between $|x\pm\rangle$ and $|y\pm\rangle$? Measuring along the x-axis, for instance, would distinguish easily between $|x+\rangle$ and $|x-\rangle$; a measurement along the y-axis would do the same for $|y+\rangle$ and $|y-\rangle$. But indeed, without prior knowledge, a single measurement is not apt to determine an unknown state $|\psi\rangle$, lying somewhere on the Bloch sphere.

[1] The linear functional $\langle\chi|$ acts on the vector $|\chi\rangle$ such that $\langle\chi|\chi\rangle = 1$.

2.1.2 The Density Operator

Before proceeding any further, the introduction of another formalism is in order: density operators. Generally, quantum systems are found not in *pure* quantum states $|\psi\rangle$, but in probabilistic mixtures of multiple different states $|\psi_j\rangle$ with probabilities p_j. They are called *mixed* states, lie in the inner region of the Bloch sphere and they are statistical ensembles of pure states, see Fig. 2.1.

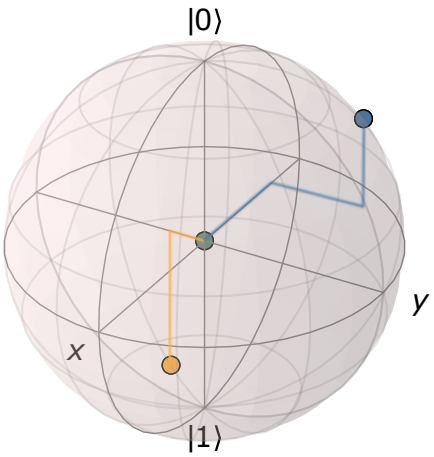

Figure 2.1: The Bloch sphere: A maximally mixed state is indicated in the center (green), a pure state on the surface (blue) and mixed state below the surface (yellow). The poles on the z-axis are defined as $|0\rangle$ and $|1\rangle$.

Pure and mixed states can be mathimatically described with the informationally richer density operator $\hat{\rho}$, which in a basis representation is the density matrix

$$\rho = \sum_j p_j |\psi_j\rangle\langle\psi_j|. \tag{2.8}$$

It is a Hermitian, $\rho = \rho^\dagger$, positive semi-definite, $\rho \geq 0$, matrix of unit trace, $\mathrm{tr}(\rho) = 1$, which is idempotent if and only if it is a pure state, $\rho^2 = \rho$, otherwise it is a mixed state. It reduces to the maximally mixed state $\rho_M = \mathbb{1}/2$, in the classical limit, corresponding to the center of the Bloch sphere. In the case of the qubit, it is represented by a 2×2 complex valued matrix. The constraints leave three real parameters $\mathbf{s} = (s_1, s_2, s_3)$ to characterize the system. For a large number of identical initial states ρ, it is easily verified from Eq. (2.3) and (2.8) that measuring an observable $\hat{A}$, represented by the

matrix A, yields

$$\langle A \rangle = tr(\rho A). \tag{2.9}$$

Projective measurements along the x-, y- or z-axis correspond to the three frequently used obversables, written here as the *Pauli matrices*

$$\begin{aligned} \sigma_1 \equiv \sigma_\mathrm{x} &= \begin{pmatrix} 0 & 1 \\ 1 & 0 \end{pmatrix}, \quad \sigma_2 \equiv \sigma_\mathrm{y} = \begin{pmatrix} 0 & -i \\ i & 0 \end{pmatrix}, \quad \sigma_3 \equiv \sigma_\mathrm{z} = \begin{pmatrix} 1 & 0 \\ 0 & -1 \end{pmatrix}, \\ \sigma_0 \equiv \mathbb{1} &= \begin{pmatrix} 1 & 0 \\ 0 & 1 \end{pmatrix}, \end{aligned} \tag{2.10}$$

which were extended by a fourth one, σ_0, the identity for posterior amenity. Applying the x, y and z Pauli operators give the expectation values along the respective axes, which are equivalent to $\mathbf{s}$. On this account, the density matrix can also be written as

$$\rho = \frac{1}{2}\left(\mathbb{1} + \mathbf{s}\,\boldsymbol{\sigma}\right) \qquad \mathbf{s} = \begin{pmatrix} \langle \sigma_\mathrm{x} \rangle \\ \langle \sigma_\mathrm{y} \rangle \\ \langle \sigma_\mathrm{z} \rangle \end{pmatrix} \qquad \boldsymbol{\sigma} = \begin{pmatrix} \sigma_\mathrm{x} \\ \sigma_\mathrm{y} \\ \sigma_\mathrm{z} \end{pmatrix}. \tag{2.11}$$

Determining an unknown quantum state ρ requires a large amount of identical copies, for there are at least measurements along three different axes, each consisting of a large enough ensemble to make a valid estimate of a single point in a continuous space.

If a measurement, described by measurement operator $\hat{M}_\mathrm{m}$, is performed upon a quantum system in the state $|\psi\rangle$, the probability for outcome m is given by

$$p(m) = \langle \psi | M_\mathrm{m}^\dagger M_\mathrm{m} | \psi \rangle. \tag{2.12}$$

Then, it is possible to define a positive operator $\hat{E}_\mathrm{m} = \hat{M}_\mathrm{m}^\dagger \hat{M}_\mathrm{m}$ such that they sum up to unity. The set of operators $\hat{E}_\mathrm{m}$ are sufficient to determine the probabilities of the different measurement outcomes [28]. The complete set of them is known as the positive-operator valued measure (POVM) Π:

$$\Pi = \{E_\mathrm{m}\}: \quad E_\mathrm{m} \geq 0, \quad \sum_m E_\mathrm{m} = \mathbb{1}. \tag{2.13}$$

Although, initially the Hilbert space was d-dimensional and repeatable measurements can only have d outcomes, quantum states form a set of dimension $d^2 - 1$. It follows that there exists no single repeatable measurement whose statistics uniquely identify arbitrary quantum states, as shortly outlined above. This stands in direct contrast to the classical situation and is the raison d'être for quantum tomography [29].

2.2 The Hilbert-Schmidt Space

A slight generalization of the previously introduced Dirac's notation is the superoperator formalism [24]. The system's Hilbert-Schmidt space is then the d^2-dimensional vector space of linear operators on the Hilbert space $\mathbf{H}$, denoted $\mathbf{B}(\mathbf{H}) = \mathbb{C}^{d\times d}$. Within this formalism, the density operator of a qubit is not represented as a 2×2-matrix, but as a 4-dimensional vector:

$$\mathbf{H} \ni \rho = \begin{pmatrix} \rho_{00} & \rho_{01} \\ \rho_{10} & \rho_{11} \end{pmatrix} \quad \rightarrow \quad \mathbf{B}(\mathbf{H}) \ni |\rho\rangle\!\rangle = \begin{pmatrix} \rho_{00} \\ \rho_{01} \\ \rho_{10} \\ \rho_{11} \end{pmatrix}. \tag{2.14}$$

The Hilbert-Schmidt space is equipped with the inner product

$$\langle\!\langle A|C\rangle\!\rangle = tr(A^\dagger C), \qquad A, C \in \mathbf{B}(\mathbf{H}) \tag{2.15}$$

and Eq. (2.9) reads

$$\langle A\rangle = \langle\!\langle \rho|A\rangle\!\rangle. \tag{2.16}$$

Let $\{B_\alpha\}$, with $\alpha = 0, 1, ..., d^2$, be an orthonormal basis of $\mathbf{B}(\mathbf{H})$, then

$$|B_\alpha\rangle\!\rangle\langle\!\langle B_\alpha| = \mathbb{1}^{d^2\times d^2} \tag{2.17}$$

and consequently

$$|A\rangle\!\rangle = \sum_\alpha |B_\alpha\rangle\!\rangle\langle\!\langle B_\alpha|A\rangle\!\rangle = \sum_\alpha |B_\alpha\rangle\!\rangle \mathrm{tr}\left(B_\alpha^\dagger A\right). \tag{2.18}$$

2.2.1 The Computational Basis

The computational basis $\{B_\alpha^c\}$ can be constructed via

$$B_\alpha^c = |i\rangle\langle j|, \tag{2.19}$$

where also $|B_\alpha^c\rangle\!\rangle = |i\rangle|j\rangle$ is a common notation. It holds then that

$$\mathrm{tr}\left(B_\alpha^{c\dagger} A\right) = \mathrm{tr}\left(|j\rangle\langle i|A\right) = \langle i|A|j\rangle = A_{\mathrm{ij}}, \tag{2.20}$$

$$|A\rangle\!\rangle = \sum_{ij} A_{\mathrm{ij}} |i\rangle|j\rangle, \tag{2.21}$$

$$(A\otimes C)\,|D\rangle\!\rangle = |ADC^\top\rangle\!\rangle. \tag{2.22}$$

2.2.2 The Normalized Pauli Basis

An alternative to the computational basis is the normalized Pauli basis $\{B_\alpha^p \equiv P_\alpha\}$. It is often used for calculations, as its basis elements are the Pauli matrices from Eq. (2.10) with a normalization

$$|P_0\rangle\!\rangle = \frac{1}{\sqrt{2}}\begin{pmatrix}1\\0\\0\\1\end{pmatrix},\ |P_1\rangle\!\rangle = \frac{1}{\sqrt{2}}\begin{pmatrix}0\\1\\1\\0\end{pmatrix},\ |P_2\rangle\!\rangle = \frac{1}{\sqrt{2}}\begin{pmatrix}0\\-i\\i\\0\end{pmatrix},\ |P_3\rangle\!\rangle = \frac{1}{\sqrt{2}}\begin{pmatrix}1\\0\\0\\-1\end{pmatrix}. \tag{2.23}$$

2.2.3 The Experimental Basis

As the previous two bases include elements, which are not physical quantum states[2], an experimental basis $\{B_\alpha^e \equiv \rho_\alpha\}$ for actual implementation is sought after. The Hilbert-Schmidt density matrices for the set of pure states $\{|0\rangle, |1\rangle, |x+\rangle, |y+\rangle\}$ is such:

$$|\rho_0\rangle\!\rangle = \begin{pmatrix}1\\0\\0\\0\end{pmatrix} \quad |\rho_1\rangle\!\rangle = \begin{pmatrix}0\\0\\0\\1\end{pmatrix} \quad |\rho_{\mathrm{x}+}\rangle\!\rangle = \frac{1}{2}\begin{pmatrix}1\\1\\1\\1\end{pmatrix} \quad |\rho_{\mathrm{y}+}\rangle\!\rangle = \frac{1}{2}\begin{pmatrix}1\\-1\\-1\\1\end{pmatrix}. \tag{2.24}$$

The other two bases from Eq. (2.19) and (2.23) are then easily recovered by linear combination.

2.3 Quantum Operations

In general, dynamical transformations of quantum states are of higher interest when it comes to computation. They are usually called *quantum operations*, *quantum maps*, *quantum processes*, *quantum channels* or, in quantum information, *quantum logical gates* or simply *gates*. In reversible dynamics, where the energy of the system is conserved, the states evolve under a unitary transformation U

$$\rho \to U\rho U^\dagger. \tag{2.25}$$

[2]The basis element $|P_0\rangle\!\rangle$ corresponds to $\mathbb{1}$, which is unphysical if considered a density matrix. This can easily be seen at the trace that is not one.

Irreversible processes can sometimes be modeled as probabilistic mixture of unitary dynamics, but more generally, any linear map on density operators can be realized as dynamical transformation

$$\rho \to G[\rho], \qquad \text{where} \qquad G[\rho_A + \rho_B] = G[\rho_A] + G[\rho_B], \tag{2.26}$$

as long as G is, first, *trace preserving* (TP) and, second, *completely positive* (CP).[3] The TP condition reads simply

$$\forall \rho : \operatorname{tr}(G[\rho]) = \operatorname{tr}(\rho). \tag{2.27}$$

The CP condition is a generalization of positivity

$$\forall \rho : (G \otimes \mathbb{1}_d)[\rho] \geq 0, \tag{2.28}$$

where $\mathbb{1}_d$ is the identity map on a d-dimensional Hilbert space. In short, all quantum dynamical transformations must be completely positive, trace-preserving linear maps (CPTP maps). Using the superoperator formalism from before, the process is conveniently written as

$$|\rho\rangle\!\rangle \to G|\rho\rangle\!\rangle. \tag{2.29}$$

Even though the TP condition is simply

$$\langle\!\langle \mathbb{1}|G = \langle\!\langle \mathbb{1}| \quad \Rightarrow \quad G^\dagger|\mathbb{1}\rangle\!\rangle = |\mathbb{1}\rangle\!\rangle, \tag{2.30}$$

no concise form of the CP criterion is known [29].

A very useful set of gates is the *Clifford group* $\mathcal{C} = \{C\}$. Its 24 elements are listed in Tab. 1. They map the Pauli operators onto themselves under conjugation [30]

$$C : \sigma_i \to \sigma_j, \qquad i,j = 0,1,2,3. \tag{2.31}$$

The average gate fidelity $\mathcal{F}^{\text{avg}}$ quantifies the accuracy of quantum maps. Between a unitary map U and a linear CPTP map G it is defined as

$$\mathcal{F}^{\text{avg}}(U,G) = \int \mu(d\psi)\, \langle\psi|U^\dagger\, G\big[|\psi\rangle\langle\psi|\big]\, U|\psi\rangle, \tag{2.32}$$

where μ is the uniform measure on pure states ψ. It is also often expressed with the average error rate r_e

$$1 - \mathcal{F}^{\text{avg}} = r_e. \tag{2.33}$$

A priori, the map from the single qubit space onto itself requires 16 parameters, but the constraints of CP and TP reduce them to 12 free parameters. How to arrange them is a question of representation and the topic of the next sections.

[3] Trace preservation means that the total probability must remain 1. However, in presence of leakage errors, this requirement is relaxed to: *The total probability must not increase.*

No.	→	Gates	→	$\langle\sigma_z\rangle$	No.	→	Gates	→	$\langle\sigma_z\rangle$
0	Id			+1	12	Y_{90}	X_{180}		0
1	Y_{90}	X_{90}		0	13	X_{-90}			0
2	X_{-90}	Y_{-90}		0	14	X_{90}	Y_{-90}	X_{-90}	+1
3	X_{180}			-1	15	Y_{-90}			0
4	Y_{-90}	X_{-90}		0	16	X_{90}			0
5	X_{90}	Y_{-90}		0	17	X_{90}	Y_{90}	X_{90}	-1
6	Y_{180}			-1	18	Y_{-90}	X_{180}		0
7	Y_{-90}	X_{90}		0	19	X_{90}	Y_{180}		0
8	X_{90}	Y_{90}		0	20	X_{90}	Y_{-90}	X_{90}	-1
9	X_{180}	Y_{180}		+1	21	Y_{90}			0
10	Y_{90}	X_{-90}		0	22	X_{-90}	Y_{180}		0
11	X_{-90}	Y_{90}		0	23	X_{90}	Y_{90}	X_{-90}	+1

Table 1: The 24 Clifford gates and the gate sequences realizing them, consisting of rotations N_θ of angle θ around the axis N. The temporal order of gate action progresses from left to right. The last column shows the theoretical expectation value, when applied to ground state $|0\rangle$ and measured along the z-axis. [7]

2.4 The Representation of a Quantum Map

The four most common representations of quantum maps are introduced here, even though for the experiments of this thesis in Chap. 6, mostly χ and Pauli transfer matrix are employed. By the means of typical processes the respective informative value of each representation is highlighted [24]. They comprise:

1. **Depolarization $G_{\mathbf{dep}}$**
   The input state is replaced with a completely mixed state with probability p, and remains unaltered with probability $1-p$. It describes a noise process, where information is completely lost with probability p.

$$G_{\mathrm{dep}}[\rho] = \left(1 - \frac{3p}{4}\right)\rho + \frac{p}{4}\left(\sigma_x\rho\sigma_x + \sigma_y\rho\sigma_y + \sigma_z\rho\sigma_z\right). \tag{2.34}$$

2. **Dephasing $G_{\mathbf{Z}}$**
   Dephasing occurs when the energy splitting of a qubit fluctuates as a function of time due to coupling to the environment. In a transmon

qubit, charge noise does this. With a probability p the phase information is lost, which can be described as a phase flip channel that projects the state onto the z-axis with p:

$$G_{\mathrm{Z}}[\rho] = \left(1 - \frac{p}{2}\right)\rho + \frac{p}{2}\sigma_{\mathrm{z}}\rho\sigma_{\mathrm{z}}. \tag{2.35}$$

3. **Spontaneous emission / amplitude damping $G_{\mathbf{amp}}$**
With a probability p, some energy loss occurs. The process is easily depicted in the Kraus representation, see Eq. (2.43), whereas a general expression looks less succinct

$$\begin{aligned} G_{\mathrm{amp}}[\rho] =& \frac{p}{4}\left(\sigma_{\mathrm{x}}\rho\sigma_{\mathrm{x}} + \sigma_{\mathrm{y}}\rho\sigma_{\mathrm{y}} + i\sigma_{[\mathrm{y}}\rho\sigma_{\mathrm{x}]} + \{\rho, \sigma_{\mathrm{z}}\}\right) \\ &+ \frac{\left(1 + \sqrt{1-p}\right)^2}{2}\rho + \frac{\left(1 - \sqrt{1-p}\right)^2}{2}\sigma_{\mathrm{z}}\rho\sigma_{\mathrm{z}}, \end{aligned} \tag{2.36}$$

where $a_{[\mathrm{i}}Aa_{\mathrm{j}]} = a_{\mathrm{i}}Aa_{\mathrm{j}} - a_{\mathrm{j}}Aa_{\mathrm{i}}$ is the index commutator and $\{a, b\} = ab + ba$ is the usual anti-commutator. Amplitude damping will be used in the noise identification protocols of this thesis.

4. **Rotation / Unitary error G_θ**
A rotation about axis $\mathbf{n}$, where $|\mathbf{n}| = 1$, by θ is written as

$$G_\theta[\rho] = e^{-i\frac{\theta}{2}\mathbf{n}\sigma}\rho e^{i\frac{\theta}{2}\mathbf{n}\sigma}, \tag{2.37}$$

which is simplified by choosing $\mathbf{n}$ to be along the z-axis, such that

$$e^{-i\frac{\theta}{2}\mathbf{n}\hat{\sigma}} = \mathbb{1}\cos\left(\frac{\theta}{2}\right) - i\sigma_{\mathrm{z}}\sin\left(\frac{\theta}{2}\right). \tag{2.38}$$

Unitary errors are treated further in Sec. 2.7, where the basis for the noise identification protocols is laid out.

2.4.1 Kraus Operators

The Kraus representation uses the Kraus operators $\hat{K}_{\mathrm{i}}$, which are not unique and need not be unitary, hermitian, nor invertible. By expressing them in a particular basis, they can be fixed, and a typical choice is once again the Pauli basis in Eq. (2.10). As for requirements, a quantum map G is CP if and only if it can be written as

$$G[\rho] = \sum_i K_{\mathrm{i}}\rho K_{\mathrm{i}}^\dagger, \tag{2.39}$$

and TP if and only if it fulfills the completeness condition

$$\sum_i K_i^\dagger K_i = \mathbb{1}. \tag{2.40}$$

Even though the CPTP conditions are easily stated, the disadvantage of the Kraus representation is that while the map G is linear, it is not linear in the Kraus operators. This makes it inconvenient for tomography [29].

Kraus operators of the representative quantum maps introduced in the beginning of Sec. 2.4 are given below.

1. **Depolarization**

$$K_0 = \sqrt{1 - \frac{3p}{4}}\,\mathbb{1}, \qquad K_1 = \frac{\sqrt{p}}{2}\sigma_x, \qquad K_2 = \frac{\sqrt{p}}{2}\sigma_y, \qquad K_3 = \frac{\sqrt{p}}{2}\sigma_z. \tag{2.41}$$

2. **Dephasing**

$$K_0 = \sqrt{1 - \frac{p}{2}}\,\mathbb{1}, \qquad K_1 = \sqrt{\frac{p}{2}}\sigma_z. \tag{2.42}$$

3. **Amplitude Damping**

$$K_0 = \begin{pmatrix} 1 & 0 \\ 0 & \sqrt{1-p} \end{pmatrix}, \qquad K_1 = \begin{pmatrix} 0 & \sqrt{p} \\ 0 & 0 \end{pmatrix}. \tag{2.43}$$

4. **Rotation**: The single Kraus operator is already given by Eq. (2.38)

$$K_0 = \begin{pmatrix} \cos\left(\frac{\theta}{2}\right) - i\sin\left(\frac{\theta}{2}\right) & 0 \\ 0 & \cos\left(\frac{\theta}{2}\right) + i\sin\left(\frac{\theta}{2}\right) \end{pmatrix}. \tag{2.44}$$

2.4.2 Process or χ-matrix

The χ-matrix is a unique $d^2 \times d^2$ matrix, Hermitian, positive semidefinite and completely determines the quantum map G. The expansion of the Kraus operators K_i in terms of the Pauli operator basis (2.10) as

$$K_i = \sum_{j=0}^{d^2-1} a_{ij}\hat{\sigma}_j \tag{2.45}$$

leads to the expression

$$G[\rho] = \sum_{j,k=0}^{d^2-1} \chi_{ij}\sigma_j\rho\sigma_k, \tag{2.46}$$

where

$$\chi = (\chi_{\mathrm{jk}}) = \left(\sum_i (a_{\mathrm{ij}})(a^*_{\mathrm{ik}}) \right) \tag{2.47}$$

are the entries of the process matrix. The CP condition comes along with the definition on the basis of the Kraus operators and the TP condition reads

$$\sum_{j,k} \chi_{jk} \sigma_k \sigma_{\mathrm{j}} = \mathbb{1}. \tag{2.48}$$

For a CPTP map, the χ-matrix has $d^2(d^2-1)$ free parameters[4] for a qubit that is 12. From that it is also seen that characterizing a quantum map will at minimum require 12 measurements.

In the following the collection of quantum maps introduced in the beginning of Sec. 2.4 are given in the χ-matrix representation.

1. **Depolarization**: Easily read off from Eq. (2.34) or (2.41) as

$$\chi = \begin{pmatrix} 1-\frac{3p}{4} & 0 & 0 & 0 \\ 0 & \frac{p}{4} & 0 & 0 \\ 0 & 0 & \frac{p}{4} & 0 \\ 0 & 0 & 0 & \frac{p}{4} \end{pmatrix}. \tag{2.49}$$

2. **Dephasing**: Similary, from Eq. (2.35) or (2.42),

$$\chi = \begin{pmatrix} 1-\frac{p}{2} & 0 & 0 & 0 \\ 0 & 0 & 0 & 0 \\ 0 & 0 & 0 & 0 \\ 0 & 0 & 0 & \frac{p}{2} \end{pmatrix}. \tag{2.50}$$

3. **Amplitude Damping**: Expanding the Kraus operators in Eq. (2.43)

$$\chi = \frac{1}{2} \begin{pmatrix} (1+\sqrt{1-p})^2 & 0 & 0 & \frac{p}{2} \\ 0 & \frac{p}{2} & -i\frac{p}{2} & 0 \\ 0 & i\frac{p}{2} & \frac{p}{2} & 0 \\ \frac{p}{2} & 0 & 0 & (1-\sqrt{1-p})^2 \end{pmatrix}. \tag{2.51}$$

4. **Rotation**: Derived from Eq. (2.37) and (2.38)

$$\chi = \begin{pmatrix} \cos^2\left(\frac{\theta}{2}\right) & 0 & 0 & i\sin\left(\frac{\theta}{2}\right)\cos\left(\frac{\theta}{2}\right) \\ 0 & 0 & 0 & 0 \\ 0 & 0 & 0 & 0 \\ -i\sin\left(\frac{\theta}{2}\right)\cos\left(\frac{\theta}{2}\right) & 0 & 0 & \sin^2\left(\frac{\theta}{2}\right) \end{pmatrix}. \tag{2.52}$$

[4] A $d^2 \times d^2$ complex hermitian matrix has d^4 parameters. The completeness condition adds d^2 constraints.

2.4.3 Hilbert-Schmidt (HS) and Pauli Transfer Matrix

Using the Hilbert-Schmidt notation from Sec. 2.2, the Hilbert Schmidt-matrix HS is defined as

$$|G[\rho]\rangle\!\rangle = HS(G)|\rho\rangle\!\rangle, \quad \forall \rho \in \mathbb{C}^{d\times d}, \tag{2.53}$$

also referred to as *superoperator* representation. The HS-matrix is unique, not generally symmetric, and, in contrast to the previous representations, satisfies multiplicability

$$HS(G_A \circ G_B) = HS(G_A)HS(G_B). \tag{2.54}$$

The HS-matrix in the normalized Pauli basis, Eq. (2.23), is called the *Pauli transfer matrix* and its entries

$$HS_{\alpha\beta} = \langle\!\langle P_\alpha|HS(G)|P_\beta\rangle\!\rangle = \langle\!\langle P_\alpha|G[P_\beta]\rangle\!\rangle = tr\left(P_\alpha^\dagger G[P_\beta]\right) \tag{2.55}$$

are the coefficients of the linear combination

$$HS = \sum_{\alpha,\beta} HS_{\alpha\beta}|P_\alpha\rangle\!\rangle\langle\!\langle P_\beta|. \tag{2.56}$$

In here, the terms HS-matrix and Pauli transfer matrix will be used interchangbly, else the basis will be noted. The TP condition takes a simple form, as it is a first row of constant entries $(1,0,0,0) = (1,\mathbf{0}^\intercal)$. The CP constraint, however, cannot be expressed in terms of the HS-matrix directly. Instead, it is transformed into the Choi-Jamilkowski (CJ) matrix, see Sec. 2.4.4, which must then be positive-semidefinite.

Since all the entries of the HS-matrix are real values in $[-1,1]$, the 12 free parameters from above are rediscovered; 3 of them comprise the vector $\mathbf{v}$ related to decoherence, and the 3×3 assemble a matrix $\mathbf{R}$,

$$HS = \begin{pmatrix} 1 & \mathbf{0}^\intercal \\ \mathbf{v} & \mathbf{R} \end{pmatrix}. \tag{2.57}$$

The matrix $\mathbf{R}$ can for instance be a rotation, Eq. (2.62), or a shrinkage, Eq. (2.59). The action on the Bloch vector $\mathbf{s}$ from Eq. (2.11) is then simply

$$HS|\rho\rangle\!\rangle = \begin{pmatrix} 1 \\ \mathbf{R}\mathbf{s}+\mathbf{v} \end{pmatrix}. \tag{2.58}$$

The HS-matrices of the representative quantum maps of the beginning of Sec. 2.4 are provided below.

1. **Depolarization**

$$HS = \begin{pmatrix} 1 & 0 & 0 & 0 \\ 0 & 1-p & 0 & 0 \\ 0 & 0 & 1-p & 0 \\ 0 & 0 & 0 & 1-p \end{pmatrix}. \tag{2.59}$$

2. **Dephasing**

$$HS = \begin{pmatrix} 1 & 0 & 0 & 0 \\ 0 & 1-p & 0 & 0 \\ 0 & 0 & 1-p & 0 \\ 0 & 0 & 0 & p \end{pmatrix}. \tag{2.60}$$

3. **Amplitude Damping**: In the HS representation the non-unitality becomes apparant in the **v** vector,

$$HS = \begin{pmatrix} 1 & 0 & 0 & 0 \\ 0 & \sqrt{1-p} & 0 & 0 \\ 0 & 0 & \sqrt{1-p} & 0 \\ p & 0 & 0 & 1-p \end{pmatrix}. \tag{2.61}$$

4. **Rotation**: The HS matrix reduces to a block matrix with an inner 2×2 rotation matrix,

$$HS = \begin{pmatrix} 1 & 0 & 0 & 0 \\ 0 & \cos\theta & -\sin\theta & 0 \\ 0 & \sin\theta & \cos\theta & 0 \\ 0 & 0 & 0 & 1 \end{pmatrix}. \tag{2.62}$$

2.4.4 Choi-Jamiolkowski (CJ) Matrix

The Choi-Jamiolkowski isomorphism states that the set of linear CPTP quantum maps on a d-dimensional system is in direct correspondence with a subset of the quantum states on a d^2-dimensional system. In other words, for each CPTP map G acting on $\mathbf{B(H)}$, there exists a corresponding Jamiolkowski state $\rho_J(G) \equiv CJ(G)$ on $\mathbf{H} \otimes \mathbf{H}$ [29]. It is given by

$$CJ(G) = (G \otimes \mathbb{1}) |\Psi\rangle\!\rangle\langle\!\langle \Psi|, \tag{2.63}$$

with $|\Psi\rangle\!\rangle = \left(1/\sqrt{d}\right) \sum_i^{d-1} |i\rangle|i\rangle$ being the maximally entangled state. For the single qubit that is $|\Psi\rangle\!\rangle = |P_0\rangle\!\rangle$. The elements of CJ and the χ-matrix that

defines G are identical up to a factor of $1/d$, which can be seen from the transformation between them

$$\chi_{\alpha\beta} = \langle\langle P_\alpha | CJ(G) | P_\beta \rangle\rangle. \tag{2.64}$$

It is therefore superfluous to write all standard processes once more.

The CP constraint reads equivalently to that of quantum states, $CJ \geq 0$. Processes are slightly more constrained than states, which is why the equivalent to the unit trace $tr(\rho) = 1$ is the stricter TP contraint $tr_1 [CJ(G)] = \mathbb{1}_2/d$, where indices correspond to Hilbert subspaces.

2.5 Characterization of Quantum Processes

As stated in the introduction, characterizing the states of and processes on quantum systems is a key share to the advancement of quantum technologies. The simplest protocols to do so are quantum tomographies on states, layed out in Sec. 2.5.1, and processes, Sec. 2.5.2. More elaborate schemes comprise randomized benchmarking, Sec. 2.5.3, and gate set tomography, Sec. 2.5.4. Their respective strengths and weaknesses corroborate self-consistent quantum tomography (SCQT) as a new mean of state evaluation, Sec. 2.5.5.

2.5.1 Quantum State Tomography (QST)

Quantum state tomography is a basic method for determining the quantum state of a system. Recall Eq. (2.11), where the density matrix of a single qubit is expressed as

$$\rho = \frac{1}{2} (\mathbb{1} + \mathbf{s}\, \sigma) . \tag{2.65}$$

By measurement of $\mathbf{s}$, one can estimate the density matrix of a given state. With the initial state ρ this reads in the superoperator notation

$$s_\mathrm{i} = \langle\langle \sigma_\mathrm{i} | \rho \rangle\rangle, \qquad \mathrm{i} = 1, 2, 3. \tag{2.66}$$

However, there are two underlying assumptions. First, access to an exhaustive number of identically prepared states to determine an expectation value is presumed. If the prepared states fluctuate, the errors propagate into the density matrix. Second, the protocol considers perfectly calibrated measurement gates. As explained in Sec. 2.1.1, in order to project a state on the respective axis, quantum gates are employed and they may introduce further errors. Both assumptions face their limits, when it comes to high

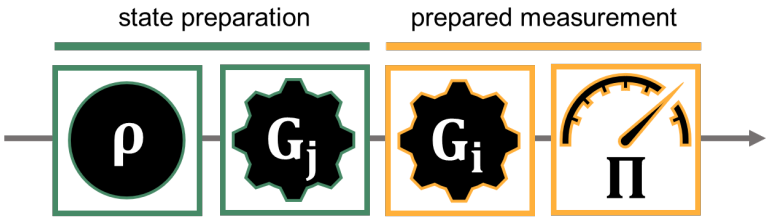

Figure 2.2: Quantum state tomography (QST) protocol: An initial state ρ is prepared with a gate G_j into an arbitrary state (green). QST finds an estimate on this state with a gate G_i and a measurement (yellow). The measurement Π is along a certain axis. For a single qubit QST preparation gates with $i = 1, 2, 3$ facilitate measurements along three axes, which is sufficient to find a point in or on the Bloch sphere.

fidelity experiments and are summarized by the term *state preparation and measurement* (SPAM) errors.

High fidelity state preparation and control gates, as well as a large amount of experiments support these assumptions. An error value of 10^{-4} per gate is typically quoted as the necessary threshold for fault-tolerant quantum computation, although more recent work using two-dimensional codes place this level closer to 10^{-3} [31–33]. As quantum technologies approach this threshold for quantum error corrections (QEC) protocols, more refined schemes are necessary [28].

Another disadvantage of a full tomography is its scalability. The computational cost scales exponentially with the number of quantum systems, which makes such a procedure impossible even for moderately sized architectures [34].

2.5.2 Quantum Process Tomography (QPT)

Quantum process tomography is a more ambitious, but closely related procedure to state tomography. It completely characterizes the dynamics of a quantum system by finding the $d^4 - d^2$ free parameters of a quantum map, from which any of the representations in Sec. 2.4 can be calculated. Besides obvious applications to quantum computation and quantum information, it has significant impact as diagnostic tool to aid improvement of primitive operations in any field of science and technology, in which quantum effects play a role.

Practically, for a qubit, one prepares all 4 of the experimental basis states ρ_β, given in Eq. (2.24), acts the process G on each of them and carries out the 3 measurements of a quantum state tomography on the resultant state

$G[\rho_\beta] = \rho'_\beta$. The protocol is sketched in Fig. 2.3. It yields the expected $3 \times 4 = 12$ parameters for a single qubit process and by linear combination of the ρ'_β, one can recover the action of $G[P_\beta] \equiv P'_\beta$ on the normalized Pauli matrices from Eq. (2.23). This gives the Pauli transfer matrix by definition (2.55) straight away

$$HS_{\alpha\beta} = \langle\langle P_\alpha | P'_\beta \rangle\rangle. \tag{2.67}$$

Either by transformation or direct calculation [28] other quantum map representations are found.

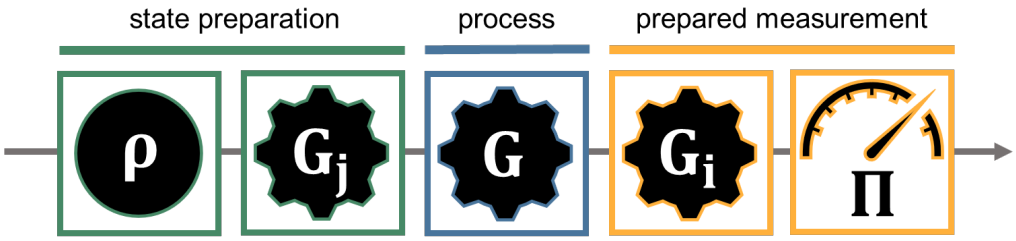

Figure 2.3: Quantum process tomography (QPT) protocol: The initial state $\{\rho\}$ is prepared with a gate G_j into one of the experimental basis states ρ_β (green). The process under inspection changes the state (blue), followed by a QST (yellow).

Similarly to QST, QPT suffers from the problem of scalability and - the more fundamental issue - SPAM errors [35]. The following three protocols were designed to bypass them by considering all processes on the system as principally error receptible.

2.5.3 Randomized Benchmarking (RB)

Standard randomized benchmarking is limited to evaluate elements C of the Clifford group $\mathcal{C}$ from Tab. 1. In RB a number m of randomly chosen Clifford gates C are applied to the initial state ρ, assumingly the ground state. Finally, the sequence is analytically mapped back to the intial state with one additional Clifford gate C_{m+1}, where the group property guarantees that this is possible. The working principle is depicted in Fig. 2.4 and can be written as

$$\left(G_{\mathrm{m}+1} \circ G_\mathrm{m} \circ \ldots \circ G_2 \circ G_1\right)[\rho] = \rho', \tag{2.68}$$

where ρ' should ideally be equal to ρ. Yet, each process $G_\mathrm{i} = \mathcal{E}_\mathrm{i} \circ C_i$ consists of the action of the ideal Clifford gate C_i and its error $\mathcal{E}_\mathrm{i}$. For longer sequences

with increasing m, these errors cause a decay of the probability of finding the initial state

$$\langle\langle \rho | \rho' \rangle\rangle = A_0 \cdot p^m + B_0, \qquad A_0, B_0 \in \mathbb{R}, \tag{2.69}$$

with two coefficients A_0 and B_0, and the decay rate p [22]. The coefficients absorb SPAM errors as well as errors on the final gate[5]. From the decay rate p the *average gate fidelity* $\mathcal{F}^{\text{avg}}$ of Eq. (2.32) is found to be

$$\mathcal{F}^{\text{avg}} = \frac{1+p}{2}. \tag{2.70}$$

Since this method only outputs a single parameter $\mathcal{F}^{\text{avg}}$ for the whole group, the more advanced protocol of *interleaved* randomized benchmarking (IRB) is used to determine single gate fidelities. In IRB, the sequence of Eq. (2.68) is interleaved with a certain target Clifford gate C_{t} with quantum process $G_{\text{t}} = \mathcal{E}_{\text{t}} \circ C_{\text{t}}$:

$$(G_{\text{m+1}} \circ (G_{\text{t}} G_{\text{m}}) \circ \ldots \circ (G_{\text{t}} G_2) \circ (G_{\text{t}} G_1))[\rho] = \rho'. \tag{2.71}$$

From Eq. (2.69) the reduced decay rate p_{t} for each interleaved target gate is used to compare to the standard RB decay rate p, and a value $\mathcal{F}_{\text{t}}$ for the gate fidelity of the target gate is

$$\mathcal{F}_{\text{t}} = \frac{1}{2}\left(1 - \frac{p_{\text{t}}}{p}\right). \tag{2.72}$$

RB does not assume any gates, but state initialization and measurement to be ideal, which leaves still a call for truly SPAM free characterization protocols. Furthermore, it is constrained to the useful, but limited set of Clifford gates, for which only a single metric can be determined[6]. Also, RB assumes the errors on subsequent gates are independent, which fails in the presence of non-Markovian or time-dependent noise. Recently, doubts have been raised that RB does not even measure average gate fidelity at all [36, 37] or that high average gate fidelity does not entail applicability to QEC when coherent errors exist [40]. Despite all these drawbacks, it is due to its simplicity that RB has become a regular benchmarking tool to quantify gate accuracy [21, 22].

[5] This defining property of RB is recently questioned in [36, 37]

[6] For non-Clifford RB schemes the reader is directed to [38, 39]

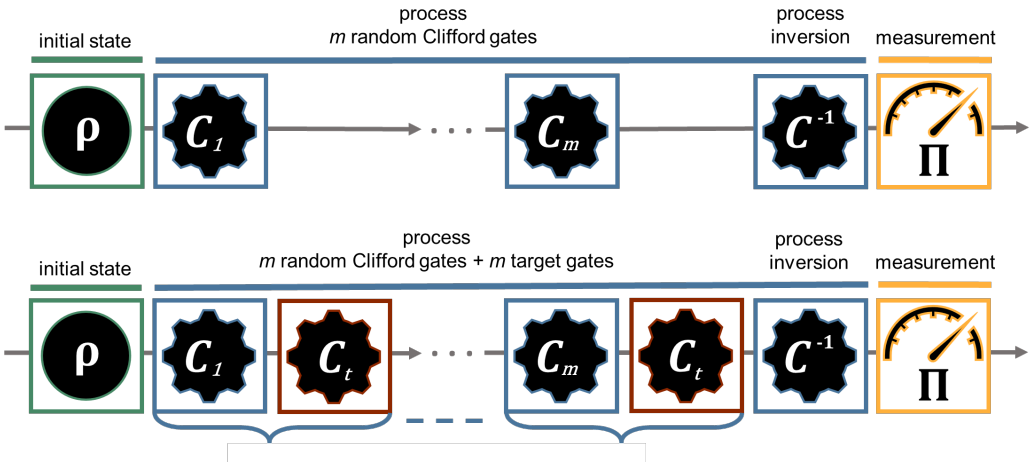

Figure 2.4: (Top) In randomized benchmarking (RB) a sequence of m randomly chosen Clifford gates $C_{\mathrm{m}} \circ ... \circ C_1$ acts on the inital state. The whole sequence is then inverted by one additional $C_{\mathrm{m+1}} = C^{-1}$. Repeating these steps for various m yields an exponential decay that is representative for the average gate fidelity $\mathcal{F}^{\mathrm{avg}}$ of the Clifford group. (Bottom) Interleaved RB (IRB) interleaves the standard RB with a target set. Now, m is the number of gate pairs $C_{\mathrm{t}} \circ C_{\mathrm{i}}$. The new decay rate is then compared with the previous one. The decline in accuracy is connected to the specific gate fidelity $\mathcal{F}_{\mathrm{t}}$.

2.5.4 Gate Set Tomography (GST)

Gate set tomography (GST) grew out of QPT and can be seen as a self-consistent extension of it, meaning that SPAM errors, which made QST and QPT inherently faulty, are avoided. GST involves a higher number of experiments[7] and - in its state of the art form - a refined post-processing for a significant estimate on all the involved operations.

GST assumes (I) the system in question to be a qubit and (II) each gate to be stationary and Markovian[8]. It then puts forward an estimate $\tilde{s}$ of a so-called *gate set* s

$$s = \{\rho, G_0, ..., G_{\mathrm{m}}, \Pi\}, \tag{2.73}$$

consisting of linear CPTP maps $G_{\mathrm{i}} \in \mathbf{B(H)}$, the inital qubit's state $\rho \in \mathbf{H}$ and a 2-outcome POVM $\mathbf{H}^* \ni \Pi = \{E, \mathbb{1} - E\}$.

[7] A GST is polynomially worse than QPT, with a single qubit LGST requiring 40 experiments, whereas QPT only needs 12. Depending on the order of preciseness, further experiments are added.

[8] GST can also detect and quantify violations of these assumptions.

Data stems from gate sequences, each including (a) initialization, (b) a series of gates, and (c) measurement, see Fig. 2.5. The series of gates are conceptually separated in *fiducial gates* $\mathcal{F}_g$ and *germ sequences* $\mathcal{K}$, both based on the fundamental gates G_i in the gate set.

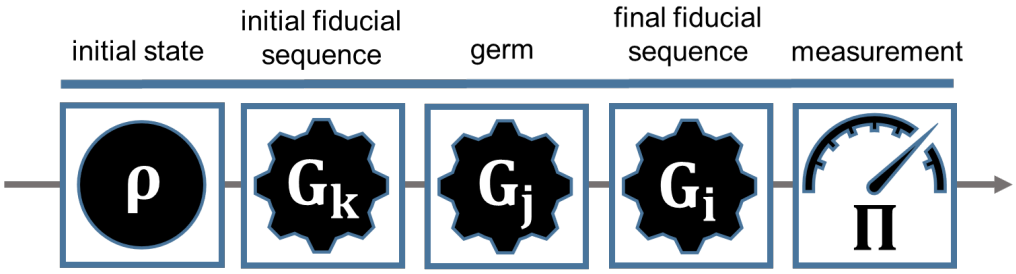

Figure 2.5: Gate set tomography (GST) protocol: The fiducial sequences are generally a sequence of gates, chosen such that they are informationally complete to allow an estimate on the complete gate set $s = \{\rho, G_0, ..., G_m, \Pi\}$ can be made. For more extended GST protocols, the length of the germ sequence in the middle increases considerably.

The fiducials $\mathcal{F}$ facilitate sufficiently diverse input states and measurements to completely probe the operation sandwiched between them, a notion referred to as *informationally complete* (IC). A set of matrices is IC, if and only if it spans the vector space $\mathbf{B(H)}$, which requires at least d^2 linearly independent matrices, for instance

$$\mathcal{F} = \big\{\{\}, X_{90}, Y_{90}, X_{90}X_{90}\big\} = \big\{G_0, G_1, G_2, G_1 \circ G_1\big\}, \tag{2.74}$$

with the null gate $\{\}$. The null gate is distinct from an idle gate Id of waiting period equal to the gate action time t_g. This choice resembles the complete basis of input states from Eq. (2.24). Certainly, it could include X_{180} as a fourth gate. The fiducial gates $\mathcal{F}$ would then be free of products. The cost of estimating a fourth gate is however higher then the gain by avoiding a product gate [24].

Then again, it is preferable to choose them uniformly distributed [25] and experimental convenience suggests therefore the 6 sequences that prepare eigenstates of the Pauli operators

$$\mathcal{F} = \big\{\{\},\ X_{90},\ Y_{90},\ X_{90}X_{90},\ Y_{90}Y_{90},\ X_{90}X_{90}X_{90},\ Y_{90}Y_{90}Y_{90}\big\}. \tag{2.75}$$

The germs $\mathcal{K}$ define the operations of interest. They are sandwiched by an exhaustive set of fiducial combinations, not different from a process tomography on them. The obvious choice are the gates G_j itself; if the

sequence is repeated N times with the number of 0 and 1 counts recorded, the gate accuracy is estimated with $\mathcal{O}\left(1/\sqrt{N}\right)$. For better accuracy, powers of G_j are probed. However, more sophisticated combinations are necessary to amplify every possible error as each germ is sensitive to some nontrivial linear combination of gate set parameters.

How does a GST analysis work now? In the first step, a linear inversion estimate is retrieved from data of sequences that purely consist of fiducials (no germs yet). This is a very rough guess about the gates and SPAM operations that will serve as a starting point for further improvements. Before that, however, the unavoidable *gauge degrees of freedom* of this estimate are of concern. Every experimentally accessible probability p is invariant under a transformation of s by any invertible matrix M,

$$p = tr\left(\Pi G[\rho]\right) = tr\left(\Pi M^{-1} \circ M \circ G \circ M^{-1} \circ M[\rho]\right). \tag{2.76}$$

That could be for instance a unitary gauge, an expansion, an extraction or an origin shift. Therefore, the protocol needs a *target gate set* s_t, which in this thesis is chosen as

$$s_t = \left\{\rho = |0\rangle\langle 0|,\ G_0 = Id,\ G_1 = X_{90},\ G_2 = Y_{90},\ \hat{E} = |0\rangle\langle 0|\right\}. \tag{2.77}$$

The preliminary gauge-fixing makes the *linear inversion* estimate $\tilde{s}$ as similar to the target gate set s_t as possible. The gauge-fixed result is then truncated to the nearest CP map to ensure *physicality* for the next steps.

Iteratively more data is added. In the n^{th} iteration, data from sequences including germs of length 2^{n-1} are injected. In every step, the estimate is numerically adjusted to minimize the χ^2-divergence between observed and estimated count rates. This χ^2-estimate poses the seed for the numerical *Maximum Likelihood Estimation* (MLE), after which a last gauge optimization is performed to maximize similarity to the targets.

A derivation of GST with detailed discussions of its various optimizations is found in its original form in [23], reviewed in [24] and summarized in a recent implementation [25].

The gauge-fixing and physicality are not treated in the same step, hence, GST does not guarantee its estimate to fulfill both at the same time. With the self-consistent quantum tomography of the next section a novel alternative is presented.

2.5.5 Self-Consistent Quantum Tomography (SCQT)

As GST lacks to provide a gauge independent and physical estimate simultaneously, self-consistent quantum tomography (SCQT) has been introduced [26]. It assumes that the dimension of the system is finite and known

(here: single qubit) and that noises are purely Markovian[9]. It estimates and regularizes simultenously based on the estimator

$$\tilde{s} = \underset{s:\text{phys}}{\operatorname{argmin}} \left(\sum_{i=1}^{49} \|\mathbf{p}_\text{i}(s) - \mathbf{f}_\text{i}\|_2^2 + \lambda \|s - s_\text{t}\|_2^2 \right), \tag{2.78}$$

where the 2-norm is defined as

$$\|\mathbf{x}\|_2 = \sqrt{\sum_i x_\text{i}^2}. \tag{2.79}$$

The probability distribution $\mathbf{p}_\text{i} = (p_\text{i,g}, p_\text{i,e})$ of finding the ground state for the gate sequence with ID = 1, 2, ..., 49 (see Fig. 2.6)[10], is calculated from the gate set s in question; the probability distribution $\mathbf{f}_\text{i} = (f_\text{i,g}, f_\text{i,e})$ is retrieved from the experimental data directly. The constant

$$\lambda = \frac{\beta}{N^\alpha} \tag{2.80}$$

is set by choosing α and β appropriately, where

$$N = \frac{1}{49} \sum_{i=1}^{49} N_\text{i}. \tag{2.81}$$

Here, $\lambda = \infty$ causes the estimated gate set $\tilde{s}$ to be identical with the target gate set s_t, whereas small λ shift the emphasis onto the experimental data. The 2-norm of the gate set is further expanded into

$$\begin{aligned} \|s - s_\text{t}\|_2^2 = \frac{1}{2}\|\rho - \rho_\text{t}\|_2^2 + \frac{1}{4} \sum_{i=0,1} \|\Pi_\text{i} - \Pi_\text{i}^{(\text{t})}\|_2^2 \\ + \frac{1}{2d^2} \sum_{i=0}^{2} \|HS(G_\text{i}) - HS\left(G_\text{i}^{(\text{t})}\right)\|_2^2 \end{aligned} \tag{2.82}$$

and handles the gauge-fixing. The whole argument of Eq. (2.78) is minimized with a constraint to physical gate sets. Through this a gauge-equivalent and physical $\tilde{s}$ is found.

These are the five characterization methods treated in this thesis, summarized in Tab. 2. Before the realm of quantum information is relinquished in favor of circuit quantum electrodynamics, two more useful notions will be introduced in the last two parts of this chapter: a model of decoherence and error generators.

[9] Time-dependent noises like warming of the dilution refrigerator for instance are common in the setup and violate the Markovian assumption.

[10] The first line in Fig. 2.6 is one epxeriment, the second are three, the third nine, the fourth 27, and the last one nine, which sums up to 49 distinct experiments.

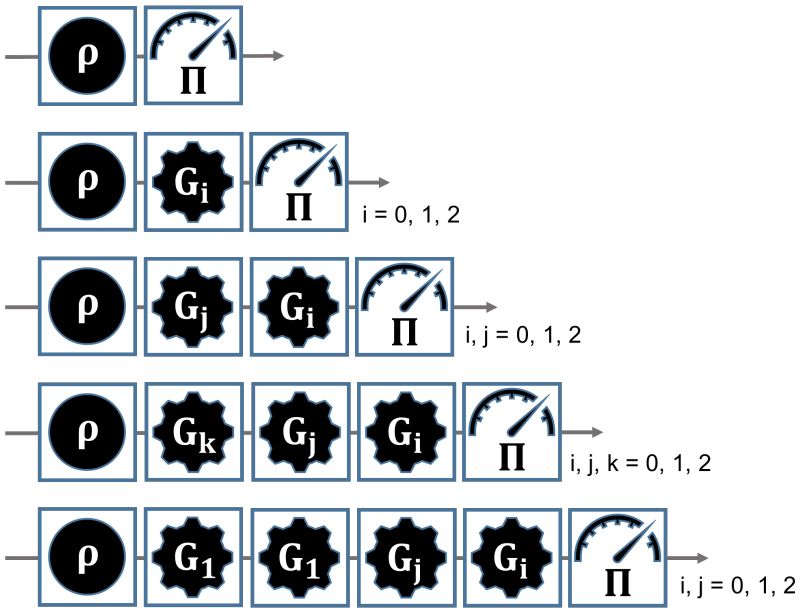

Figure 2.6: The 49 experiments of self-consistent quantum tomography.

	objects	limitation	SPAM errors	gauge-equiv.	physical	cost
RB	p	Cliff. gates	Robust	—	Depol.	Poly
QT	$\rho/G/\Pi$	—	✗	—	✓	Exp
LGST	$\{\rho, G_\mathrm{i}, \Pi\}$	—	✓	✓	✗	Exp
PGST	$\{\rho, G_\mathrm{i}, \Pi\}$	—	✓	✗	✓	Exp
SCQT	$\{\rho, G_\mathrm{i}, \Pi\}$	—	✓	✓	✓	Exp

Table 2: Characterization methods in a nutshell: Randomized benchmarking (RB) estimates only the decay rate p on Clifford gates, is non SPAM-error free, but robust to them and captures mainly depolarizing errors. Quantum tomographies (QT) for state, process and POVM scale as badly as linear and projected gate set tomography (LGST and PGST), but do not provide a full gate set. The novel self-consistent quantum tomography (SCQT) scales equally disadvantageous, but has the strongest theoretical backbone.

2.6 A Decoherence Model

The interaction of quantum systems with their environment imposes certain limits and constraints in the study of their dynamics. The level of isolation of a quantum system dictates the rate at which it can exchange energy with its

environment. This means that a quantum system will not hold a particular state for an arbitrary time, but will in general interact with its environment and relax (or excite) to another state with different energy. This brings a trade-off in terms of controllability: a system that does not exchange much energy with the environment will keep its state for longer, but that will exacerbate access and manipulation, which need such coupling.

Interaction with the environment can also result in decoherence, a process that does not result in energy exchange but that transforms quantum coherent states (superpositions) into classical mixed states. The process of decoherence will be modeled through the dynamics of [41]

$$\begin{aligned}\frac{d\rho}{dt} = &-\frac{\Gamma_+}{2}\left(\sigma_-\sigma_+\rho + \rho\sigma_-\sigma_+ - 2\sigma_+\rho\sigma_-\right)\\ &-\frac{\Gamma_-}{2}\left(\sigma_+\sigma_-\rho + \rho\sigma_+\sigma_- - 2\sigma_-\rho\sigma_+\right)\\ &-\Gamma_0\left(\rho - \sigma_3\rho\sigma_3\right),\end{aligned} \tag{2.83}$$

where Γ_- is the rate at which relaxation processes prematurely bring the qubit from the excited to ground state. If the qubit is in contact with a bath of non-zero temperature, there will be excitation at rate Γ_+, leading to an energy relaxation time T_1 of [42]

$$\frac{1}{T_1} := \Gamma_+ + \Gamma_-. \tag{2.84}$$

T_1 is a measure of how long an excited state remains. It is also called *qubit lifetime* or simply, but ambiguously, *coherence time*[11]. Since the system exchanges some energy with its sorroundings, the qubit will gradually reach a classical mixed state, associated with thermal equilibrium. The dilution fridge cools below this state and reestablishes the ground state of the qubit. Typical values for superconducting qubits are $5 \sim 100\,\mu s$ [42–45].

T_2 on the other hand is the exponential decay rate of the off-diagonal elements of a density matrix. It quantifies how long a superposition is stable, or equivalently, how long the relative phase between the pure states of the superposition is maintained. It is the primary parameter to be called *coherence time*[12], subsuming relaxation (T_1) and dephasing (T_ϕ) by

$$\frac{1}{T_2} = \frac{1}{2T_1} + \frac{1}{T_\phi}. \tag{2.85}$$

[11] In terms of nuclear magnetic resonance (NMR), it is referred to as the *longitudinal relaxation time* or the *spin-lattice relaxation time* and is a constant associated with the loss of signal intensity.

[12] In NMR T_2 is called *transversal coherence time* or *spin-spin relaxation time*.

If $T_\phi \to \infty$, meaning pure dephasing is absent, then $T_2 = 2T_1$. In the Bloch sphere picture, T_1 pushes the state towards the center, where the maximally mixed state lies, and T_ϕ involves the diffusing along a parallel of the sphere.

To find the χ-matrix representation for a decoherence process, another parameter will be practical

$$\alpha := \frac{\Gamma_+ - \Gamma_-}{\Gamma_+ + \Gamma_-}. \tag{2.86}$$

While the energy relaxation time T_1 and the dephasing time, or coherence time, T_2 are measured directly with the protocols from Sec. 5.2, α needs to be determined indirectly by evaluating the steady state ratio Γ_+/Γ_-.

The process matrix of the decoherence model is then

$$\chi(t) = \frac{1}{4}\begin{pmatrix} 1+e^{-t/T_1}+2e^{-t/T_2} & 0 & 0 & \alpha(1-e^{t/T_1}) \\ 0 & 1-e^{t/T_1} & -i\alpha(1-e^{t/T_1}) & 0 \\ 0 & i\alpha(1-e^{t/T_1}) & 1-e^{t/T_1} & 0 \\ \alpha(1-e^{t/T_1}) & 0 & 0 & 1+e^{-t/T_1}-2e^{-t/T_2} \end{pmatrix} \tag{2.87}$$

and the Pauli transfer matrix is

$$HS^{gb}(t) = \begin{pmatrix} 1 & 0 & 0 & 0 \\ 0 & -e^{t/T_2} & 0 & 0 \\ 0 & 0 & -e^{t/T_2} & 0 \\ \alpha(1-e^{t/T_2}) & 0 & 0 & e^{-t/T_1} \end{pmatrix}. \tag{2.88}$$

Constraning the discussion to the single qubit case and identifying the depolarizing channel as the prevalent source of decoherence (Sec. 2.4), the depolarizing ratio r reads

$$r = \frac{d^2(1-\chi_{00})}{d^2-1} = \frac{4}{3}p \tag{2.89}$$

and the average gate fidelity is

$$\mathcal{F}^{\text{avg}} = 1 - \frac{r}{2} = \frac{1+2\chi_{00}}{3} = \frac{1}{2} + \frac{1}{6}e^{-t/T_1} - \frac{1}{3}e^{-t/T_2}. \tag{2.90}$$

This model predicts a superposed exponential decay for $\mathcal{F}^{\text{avg}}$ in the time scale of coherence and puts an upper theoretical bound on the fidelity of any gate, simply due to the gate's non-zero action time t_g.

Experimentally, this can be evaluated by a quantum process tomography after various idle times, from which a series of process matrices can be analyzed. The protocol is depicted in Fig. 2.7.

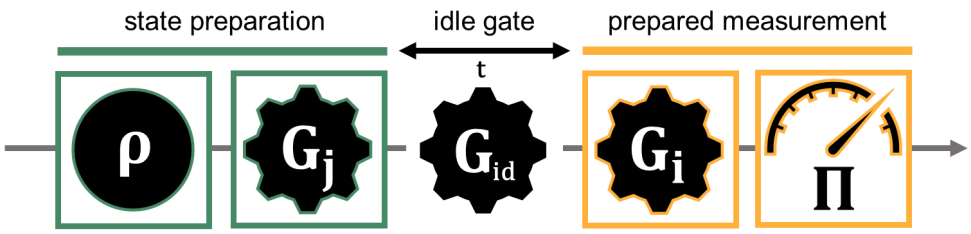

Figure 2.7: The experimental protocol to test the decoherence model in a series of quantum process tomographies.

2.7 Error Generators

Time-independent Liouvillian dynamics are captured in the Master equation

$$\frac{d\rho}{dt} = -i\,[H,\rho] + \{J,\rho\} + \sum_{\alpha,\beta=1,2,3} K_{\alpha\beta}\sigma_\alpha\rho\sigma_\beta^\dagger, \tag{2.91}$$

where H, J and K are the dynamics generators, the Hamiltonian and the two dissipation generators respectively. In the Hilbert-Schmidt notation, this is

$$\frac{d}{dt}|\rho\rangle\!\rangle = G|\rho\rangle\!\rangle \tag{2.92}$$

with the generator G in the computational basis being

$$G^c = -i(H\otimes\mathbb{1} - \mathbb{1}\otimes H^\top) + (J\otimes\mathbb{1} + \mathbb{1}\otimes J^\top) + \sum_{\alpha,\beta} K_{\alpha\beta}\sigma_\alpha\otimes\sigma_\beta^\top. \tag{2.93}$$

After idle time t, the state is

$$|\rho(t)\rangle\!\rangle = HS(t)|\rho(0)\rangle\!\rangle = e^{tG}|\rho(0)\rangle\!\rangle. \tag{2.94}$$

Calculating the matrix logarithm, the generator G^c is obtained,

$$G^c = \frac{1}{t}\log\big(HS(t)\big). \tag{2.95}$$

From the decoherence model in Sec. 2.6 the dissipators are derived to be

$$J = -\frac{1}{4}\left(\frac{1}{T_\phi} + \frac{1}{T_1}\right)\sigma_0 - \frac{1}{2}\frac{\alpha}{T_1}\sigma_z \tag{2.96}$$

and

$$K = \frac{1}{4}\begin{pmatrix} 1/T_1 & i\alpha/T_1 & 0 \\ -i\alpha/T_1 & 1/T_1 & 0 \\ 0 & 0 & 2/T_2 - 1/T_1 \end{pmatrix}. \tag{2.97}$$

Unitary errors are one special error source with impact on the average gate fidelity $\mathcal{F}^{\text{avg}}$. They will be used in protocols for noise identification in Sec. 7.4. For a normalized vector $\mathbf{n}$, a unitary transformation U can be defined as rotation with angle θ around this axis

$$U(\mathbf{n},\theta) := e^{-i\frac{\theta}{2}\mathbf{n}\sigma} = \cos\left(\frac{\theta}{2}\right)\mathbb{1} - i\sin\left(\frac{\theta}{2}\right)\mathbf{n}\sigma. \tag{2.98}$$

Because of the entry $\chi_{00} = \cos^2\left(\frac{\theta}{2}\right)$, the decoherence model from Sec. 2.6 yields the relation

$$\theta = 2\arcsin\left(\sqrt{\frac{3}{2}(1-\mathcal{F}^{\text{avg}})}\right). \tag{2.99}$$

With this formula one can choose an angle of over/under-rotation to target a specific average gate fidelity.

Chapter 3 Superconducting qubits

The quantum counterpart of the classical bit in the common computer is the qubit, the quantum bit. Once again, this is (1) a two-level quantum system that (2) maintains its quantum information over time (coherence) and allows for (3) state initialization, (4) gate operations as well as (5) measurement of the final state [27]. These requirements inspired an assortment of schemes and physical platforms to realize a qubit. *Microscopic* quantum systems such as nuclear and electronic spins, photon polarization, electronic levels in trapped ions and in crystal defects have been shown to work as qubits [28].

The *macroscopic* phenomenon of superconductivity has inspired the so-called superconducting qubit. Unlike its microscopic competitors it can be engineered to desirable specifications, because it is not a *natural* quantum system, but an engineered one, hence its classification as *artificial* atom. They are produced by using the familiar infrastructure of micro- and nano-fabrication techniques. The strong interaction with the environment that is caused by its macroscopicity was, at first, a major obstacle, but clever designs reduced it to a workable level. In fact, now the remaining coupling proves convenient for gate operation and readout, making the superconducting qubit nowaday's most promising candidate for full-fledged quantum computing [46, 47].

Historically, there are three major distinctions in superconducting qubits, the *charge*, the *flux* and the *phase* qubit. They obtained their names from the respective degree of freedom which is used for coupling or interaction [47].

The transmission line shunted plasma oscillation qubit, called *transmon qubit* [48], attempts the tightrope walk over the aforementioned requirements. It is a hybrid form, though traditionally considered a charge qubit, because it extends the fundamental circuit of a prototypical charge qubit, the *Cooper Pair Box* (CPB)[13]. In this thesis, all experiments were conducted on a transmon qubit.

In order to brew the effective Hamiltonian broth $\mathcal{H}$ of the sample used here, four ingredients are infused:

1. *Resonator* (=cavity): quantized LC oscillator with $\mathcal{H}_\mathrm{r}$ in Sec. 3.1.

2. *Artificial atom* (=qubit): anharmonic oscillator with $\mathcal{H}_\mathrm{a}$ in Sec. 3.2.

[13] A similar picture exists for the other two superconducting qubits. The prototypical flux qubit is the *RF-SQUID* and the prototypical phase qubit is the *current-biased junction*

3. *Interaction* between them: matter-light coupling (=atom-field interaction) with $\mathcal{H}_{\text{int}}$ in Sec. 3.3.

4. *Drive*: another interaction with $\mathcal{H}_{\text{d}}$ in Sec. 3.4.

At last, in Sec. 3.5 and Sec. 3.6, the control and readout mechanism is outlined. The discussion follows mainly [49–51].

3.1 The Resonator $\mathcal{H}_{\text{r}}$

3.1.1 Electrical Circuits

An electrical circuit is a network of nodes that are joined by resistors, capacitors and inductors. For circuits made from superconductors, the resistances are negligible, so the focus here lies therefore on capacitors and inductors. Each component i carries the current $I_i(t)$ and causes a voltage drop $V_i(t)$. For the derivation of the Hamiltonian, it is more convenient to work with charges $Q_i(t)$ and fluxes $\Phi_i(t)$, given by

$$Q_{\text{i}}(t) = \int_{-\infty}^{t} dt' I_{\text{i}}(t'), \tag{3.1}$$

$$\Phi_{\text{i}}(t) = \int_{-\infty}^{t} dt' V_{\text{i}}(t'). \tag{3.2}$$

It is assumed that any external bias is switched on at $t = -\infty$. In the following, the Hamiltonian of the parallel LC oscillator will be derived classically. Via quantization, the quantum version is subsequently retrieved.

3.1.2 The Quantum LC Oscillator

The parallel LC oscillator is the simplest circuit containing a single capacitor with capacitance C and a single inductor with inductance L. The classical Hamiltonian of the circuit is derived from the Lagrangian formulation

$$\mathcal{L}(\Phi_1(t), \dot{\Phi}_1(t), ...) = T - V, \tag{3.3}$$

where commonly T comprises the *kinetic* and V the *potential* energy terms. For the LC oscillator, this translates to *capacitive* energy terms for T and *inductive* ones for V. The LC circuit has only one active node, indices are therefore omitted. Abiding Kirchhoff's laws, the Lagrangian is

$$\mathcal{L}(\Phi, \dot{\Phi}) = \frac{C\dot{\Phi}^2}{2} - \frac{\Phi^2}{2L}. \tag{3.4}$$

The charge $Q = \partial\mathcal{L}/\partial\dot{\Phi}$ is defined as the conjugate momentum of the flux Φ. A Legendre transformation $\mathcal{H}(\Phi, Q) = \dot{\Phi}Q - \mathcal{L}$ yields the classical resonator Hamiltonian

$$\mathcal{H}_{\mathrm{r}}^{(cl)} = \frac{Q^2}{2C} + \frac{\Phi^2}{2L}. \tag{3.5}$$

The quantization is carried out by replacing the classical variables $\{\Phi, Q\}$ with their corresponding quantum operators $\{\hat{\phi}, \hat{q}\}$. Then the commutation relation

$$[\phi, q] = i\hbar \tag{3.6}$$

holds. With the introduction of the resonator's angular resonance frequency

$$\omega_{\mathrm{r}} = \frac{1}{\sqrt{LC}} \tag{3.7}$$

and its impedance

$$Z = \sqrt{\frac{L}{C}} \tag{3.8}$$

it also holds that

$$\phi = \sqrt{\frac{\hbar Z}{2}}\left(a + a^\dagger\right), \qquad q = -i\sqrt{\frac{\hbar}{2Z}}\left(a - a^\dagger\right). \tag{3.9}$$

The creation and annihilation operator can be defined as

$$a^\dagger = \frac{1}{\sqrt{2Z\hbar}}(\phi - iZq), \qquad a = \frac{1}{\sqrt{2Z\hbar}}(\phi + iZq), \qquad \left[a, a^\dagger\right] = 1. \tag{3.10}$$

The resonator's Hamiltonian is then quantized in the ordinary way

$$\mathcal{H}_{\mathrm{r}} = \hbar\omega_{\mathrm{r}}\left(a^\dagger a + \frac{1}{2}\right). \tag{3.11}$$

This is the expression that will later be used as one part of the Hamiltonian $\mathcal{H}$ of the whole system.

The time-independent Schrödinger equation

$$\mathcal{H}_{\mathrm{r}}|\psi\rangle = E|\psi\rangle \tag{3.12}$$

gives a set of energy eigenvalues

$$E_{\mathrm{n}} = \hbar\omega_{\mathrm{r}}\left(n + \frac{1}{2}\right), \tag{3.13}$$

which are equally spaced by multiples of $n = a^\dagger a$, which is the photon number in the LC circuit.

3.1.3 A Chain of LC Oscillators

The described resonator models both a coplanar waveguide resonator and the three-dimensional cavity used in this thesis. They have multiple modes, of which only one will be of interest. The discussion is identical: Independent from transmission or reflection measurement they can be treated as the continuum limit of a sequence of LC oscillators. The effective Hamiltonian

$$\mathcal{H} = \hbar \sum_m \omega_{\mathrm{r,m}} \left(a_{\mathrm{m}}^\dagger a_{\mathrm{m}} + \frac{1}{2} \right) \tag{3.14}$$

employs the resonance frequencies $\omega_{\mathrm{r,m}} = m\pi v_{\mathrm{ph}}/l$ with the harmonic mode number m, the phase velocity v_{ph} and the length of the resonator l. However, for the scope of this thesis it is adequate to examine only a single mode, which lies in the vicinity of a particular frequency ω_{r} [50]. Near resonance $\mathcal{H}_{\mathrm{r}}$ of a single LC oscillator, Eq. (3.11), sufficiently reproduces the phenomena in the chain of LC oscillators.

3.2 The Artificial Atom $\mathcal{H}_{\mathrm{a}}$

3.2.1 A Josephson Junction for Anharmonicity

In atomic and molecular spectra mostly non-equally spaced energy gaps of the eigenvalues occur. Common electrical elements (capacitors, inductors and resistors) are all linear, hence, circuits built from these elements are linear as well and show equidistant energy levels like the ones in Eq. (3.13). To access only two levels of the energy spectrum, a nonlinear element is indispensable. Additionally, it must be non-dissipative. The *Josephson junction* provides exactly that, see Fig. 3.1a.

The Josephson junction consists of two superconducting electrodes (e.g. Aluminum), separated by a thin insulating barrier (e.g. Aluminum Oxide, $\approx 1\,\mathrm{nm}$). At low temperatures the fermionic electrons that obey Fermi-Dirac statistics and the Pauli exclusion principle form pairs. These so-called *Cooper pairs* behave as bosons and can occupy the same quantum state, surmounting in the phenomenon of superconductivity.

The junction behaves as a pure non-linear inductance (Josephson element) with the characteristic Josephson energy E_{J} in parallel with a capacitance C_{J} corresponding to the parallel plate capacitor formed by the two overlapping films of the junction, see Fig. 3.1c [47, 52].

In the Josephson junction the collective superconducting order of one electrode, parametrized by a phase δ_1, coherently connects with that of the other electrode, δ_2, via the elastic tunneling of Cooper pairs through the

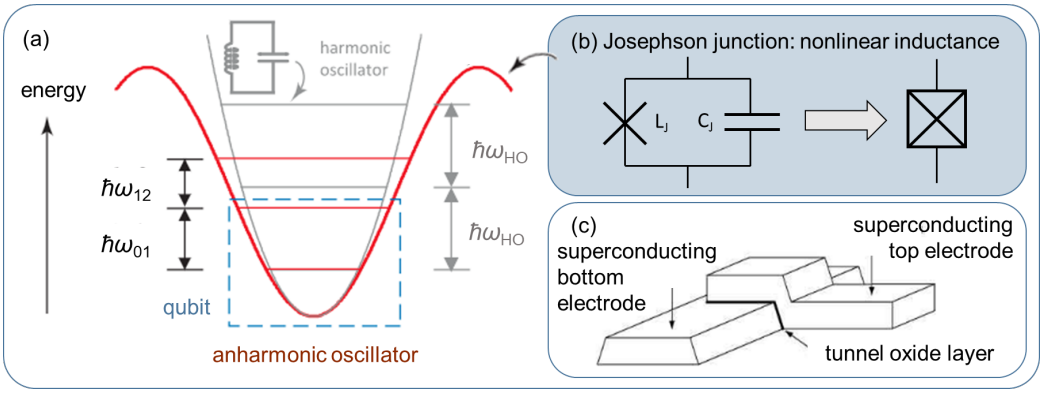

Figure 3.1: (a) As the Josephson junction inductance is nonlinear the potential becomes anharmonic (red), the quantized harmonic oscillator with equadistant energy spacing is shown for comparison (grey). The two lowest levels constitute the qubit (blue) with resonance frequency ω_{01}. (b) Circuit representation of a Josephson tunnel junction. The irreducible Josephson element is represented by a cross. (c) Josephson tunnel junction of two superconducting electrodes, separated by a thin oxide layer. Adapted from [47, 52].

barrier. As Josephson showed, the energy E of the Josephson element is connected to the phase difference $\delta = \delta_1 - \delta_2$ of the superconducting condensate across the junction via

$$E = -E_J \cos\delta. \tag{3.15}$$

E_J is the Josephson energy, a property of the junction depending on the superconducting gap and the barrier transparency [53, 54]. The resulting supercurrent I and the junction voltage V are also related to the phase difference δ,

$$I = I_C \sin\delta \tag{3.16}$$

and

$$V = \frac{\Phi_0}{2\pi}\frac{d\delta}{dt}. \tag{3.17}$$

Here, I_C is the junction critical current, determined by junction area and barrier transparency, and $\Phi_0 = h/2e$ is the superconducting flux quantum. It sets the scale of the nonlinearity. Using the standard relation for inductance

$$V = L_J \frac{dI}{dt}, \tag{3.18}$$

one can identify a Josephson inductance L_J that is nonlinear in δ,

$$L_J = \frac{\Phi_0}{2\pi I_C \cos\delta}. \tag{3.19}$$

The nonlinear inductance combined with the self-capacitance C_J makes for the anharmonic oscillator [53].

The derivation from circuit theory with branch flux $\Phi(t) = \int_{-\infty}^{t} dt' V(t')$ results in the phase

$$\delta = \frac{2\pi}{\Phi_0}\Phi. \tag{3.20}$$

The Josephson element behaves as a nonlinear inductor, with an energy $E = -E_J \cos(2\pi\Phi/\Phi_0)$ that, due to the discreteness of the Cooper pair charge, is periodic in the flux [54]. In short, the nonlinearity of the Josephson junction originates from Cooper pairs crossing the insulating barrier.

A few comments are in order. First, unpaired electrons are negligible as long as the voltage V is small compared to the energy gap Δ of the superconductor: $V \ll \Delta/e$. Aluminum becomes superconducting below $T_c = 1.2\,\mathrm{K}$, the energy gap at $T \ll T_c$ is $\Delta \approx 0.2\,\mathrm{meV}$. For $T \ll 1\,\mathrm{K}$ and $V \ll 0.2\,\mathrm{mV}$ ignoring unpaired electrons is valid [52].

Second, detection of a single tunneled pair necessitates the capacitive energy of one electron $E_C = e^2/2C$ to exceed the thermal energy $k_B T$. Current nanofabrication methods provide such structures with $C \approx 1\,\mathrm{fF}$, meaning that $T < 1\,\mathrm{K}$. The low temperatures pose no exceptional challenge, because cryogenic temperatures are needed anyways to exhibit quantum effects in nano-circuits [53] and common commercial equipment reaches $T \ll 1\,\mathrm{K}$.

3.2.2 The Cooper Pair Box

The Cooper Pair Box (CPB) is the prototypical charge qubit, see Fig. 3.2. One of the Josephson junction's electrodes has an external voltage V_g applied that serves for gate actions. The total capacitance of the island is $C_\Sigma = C_g + C_J$, the sum of the two involved capacitances. The CPB can equivalently be seen as a LC oscillator, where the linear inductor is replaced by the Josephson junction, which is reflected in its Hamiltonian (compare with Eq. (3.5))

$$\mathcal{H}_{\mathrm{CPB}} = \frac{q^2}{2C_\Sigma} - E_J \cos\delta. \tag{3.21}$$

By introducing the number operator $\hat{N} = -\hat{q}/2e$, which counts how many Cooper pairs have crossed the junction, and the charging energy $E_C = e^2/2C_\Sigma$,

the Hamiltonian reads

$$\mathcal{H}_{\mathrm{CPB}} = 4E_{\mathrm{C}}N^2 - E_{\mathrm{J}}\cos\delta. \tag{3.22}$$

However, there might be some effective offset charge $N_{\mathrm{g}} = C_{\Sigma}V_{\mathrm{g}}/(2e)$ in units of Cooper pair charge. The offset charge is due to the capacitively coupled gate electrode of the CPB with a DC bias voltage. The Hamiltonian for the Cooper Pair Box is therefore

$$\mathcal{H}_{\mathrm{CPB}} = 4E_{\mathrm{C}}\left(N - N_{\mathrm{g}}\right)^2 - E_{\mathrm{J}}\cos\delta. \tag{3.23}$$

This circuit's Hamiltonian is derived under a standard classical procedure in [48].

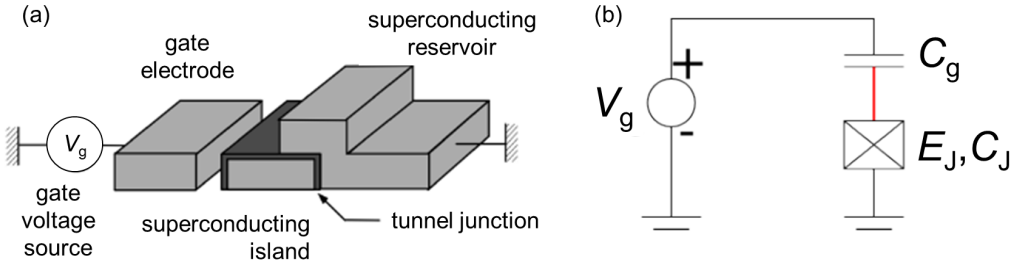

Figure 3.2: (a) The Cooper Pair Box, containing a superconducting island that is isolated by a thin tunnel oxide layer (see Josephson Junction, Sec. 3.2.1). The island is electrically connected by a Josephson tunneling current to the superconducting reservoir and capacitively to the gate electrode. (b) Circuit schematic of the Cooper Pair Box. The island is highlighted in red. Reprinted from [49, 55].

3.2.3 The Shunted Cooper Pair Box

Increasing the ratio $E_{\mathrm{J}}/E_{\mathrm{C}}$ is of special interest; why will be explained in Sec. 3.2.4. The standard way to change $E_{\mathrm{J}}/E_{\mathrm{C}}$ is to add a *shunt* capacitance across the Josephson junction (see Fig. 3.3). C_{J} adds in parallel with the much larger C_{B}. The Hamiltonian $\mathcal{H}_{\mathrm{CPB}}$ remains the same with $C_{\mathrm{J}} \to C_{\mathrm{B}}$ and all of the previous discussion holds valid [56, 57].

Before shunting the CPB, control gates could be performed via the gate voltage and readout was feasible by measuring the charge in the island. Since the shunted Hamiltonian is no longer dominated by the charging energy, such electrostatic charge-based methods are not effective any more. The previously discussed resonator will soon come in handy to save the day [49].

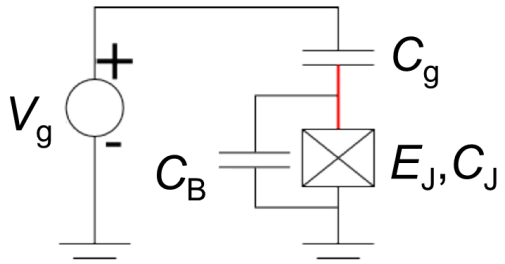

Figure 3.3: An additional capacitor with C_B across the junction reduces E_C and *shunts* the circuit. The superconducting island is again highlighted in red. Reprinted from [49].

As a side remark, many such qubits are designed with a split Josephson junction. Effectively the split junction acts like a single one, but it suddenly allows for tuning E_J by application of an external flux Φ_e from a bias line. Such a direct control of the energy levels and therefore the resonance frequencies proves handy for multi-qubit architectures. This thesis does not use a tunable transmons.

3.2.4 The Transmon Regime and Energy Levels

An exact solution to the Hamiltonian of Eq. (3.23) can be obtained in the *phase basis* by using Mathieu functions. They are shown in Fig. 3.4 and will be analyzed shortly. For circuits where the energy is mainly capacitive ($E_C \gg E_J$), it is useful to work with *charge basis* eigenstates $\{|N\rangle\}$ with $\hat{N}|N\rangle = N|N\rangle$. Here the number operator $\hat{N}$ has discrete eigenvalues and the phase operator $\hat{\delta}$ is a compact variable such that the wavefunction satisfies $\psi(\delta + 2\pi) = \psi(\delta)$. The commutation between conjugate variables N and δ reads

$$[N, \delta] = i \qquad \text{or, equivalently,} \qquad \left[N, e^{\pm i\delta}\right] = \pm e^{\pm i\delta}. \tag{3.24}$$

Since $e^{i\delta}$ is manifestly unitary, we can choose phases such that $e^{\pm i\delta}|N\rangle = |N \pm 1\rangle$, that is

$$e^{\pm i\delta} = \sum_N |N \pm 1\rangle\langle N|. \tag{3.25}$$

The $e^{\pm i\delta}$ are basically raising and lowering operators for charge [58].

The energy level diagram of Fig. 3.4 is reproduced, when the Hamiltonian

is solved by exact diagonalization in a *truncated* charge basis

$$\mathcal{H}_{\mathrm{CPB}} = 4E_{\mathrm{C}} \sum_{N=-N_{\mathrm{t}}}^{N_{\mathrm{t}}} (N - N_{\mathrm{g}})^2 |N\rangle\langle N| - \frac{E_{\mathrm{J}}}{2} \sum_{N=-N_{\mathrm{t}}}^{N_{\mathrm{t}}-1} |N+1\rangle\langle N| + |N-1\rangle\langle N|. \quad (3.26)$$

Typically, the truncation at $N_{\mathrm{t}} \approx 10$ charge basis states is enough to obtain good accuracy for the lowest energy levels in the transmon regime, where $10 \lesssim E_{\mathrm{J}}/E_{\mathrm{C}} \lesssim 100$ [50].

As mentioned earlier, the choice of the ratio $E_{\mathrm{J}}/E_{\mathrm{C}}$ is essential. If it increases, the device's anharmonicity and the sensitivity to charge noise decrease. Therefore it is a tradeoff between desirable anharmonicity and undesirable sensitivity to charge noise. In a charge qubit the energy levels are strongly dependent on the offset charge N_{g}. Low-frequency charge fluctations (the ubiquitous $1/f$ noise) will perturb the transition frequency of the qubit and reduce phase coherence. At the *sweet spot* of $N_{\mathrm{g}} = 1/2$, the degeneracy point, the frequency is first order insensitive to offset charge noise [59].

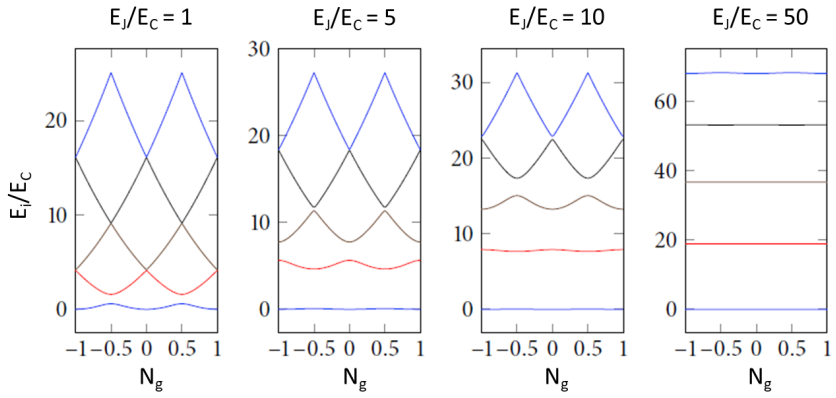

Figure 3.4: The energies E_{i} of the five lowest energy levels of the transmon Hamiltonian in units of the charging energy E_{C}. For different ratios of $E_{\mathrm{J}}/E_{\mathrm{C}}$ the Eq. (3.26) was solved. Is the ratio low, the energies are parabolic functions of the offset charge N_{g} with avoided crossings. As the ratio increases the levels become exponentially flatter. Adapted from [54].

One could ask, what the optimal condition for the trade-off in the ratio $E_{\mathrm{J}}/E_{\mathrm{C}}$ is. The charge dispersion ϵ_{m} for the m^{th} energy level is defined as the peak-to-peak energy range when N_{g} is varied. From [60] one finds in the transmon regime the approximation

$$\epsilon_{\mathrm{m}} \propto e^{-\sqrt{8E_{\mathrm{J}}/E_{\mathrm{C}}}}. \quad (3.27)$$

The anharmonicity α_m is the difference of two neighboring transition energies $E_{m\text{-}1,m}$ and $E_{m,m+1}$, where $E_{i,j} = E_j - E_i$. It holds that approximately

$$\alpha_m \simeq -E_C. \tag{3.28}$$

Compared to the transition energy of the qubit $E_{01} \simeq \sqrt{8E_J E_C}$, the relative anharmonicity is then still

$$\alpha_m^r = \alpha_m / E_{01} \propto -\frac{1}{\sqrt{E_J/E_C}}. \tag{3.29}$$

Compared to the exponential decay of the charge dispersion, the anharmonicity decreases only slowly. Thus, higher E_J/E_C is desirable [49, 54]. As stated previously, shunting the CPB with a parallel capacitor effectuates that.

3.2.5 Truncation to Qubit Space

Close to the sweet spot, where $N_g \approx 1/2$ the charging term (first term in Eq. (3.26)) is equal for $|N = 0\rangle$ and $|N = 1\rangle$. For $E_J \ll E_C$ other levels are well separated from the first two and the CPB becomes the pursued two-level system, the *qubit*. $\mathcal{H}_{CPB}$ is then off-diagonal with eigenstates $|\pm\rangle = \frac{1}{\sqrt{2}}(|0\rangle \pm |1\rangle)$ and a splitting of $E_J = \hbar\omega_a$. The characteristic frequency ω_a is the transition frequency of the artificial atom from ground state $|g\rangle$ to excited state $|e\rangle$. In accordance with the conventional choice of Pauli matrices $\sigma_z = |g\rangle\langle g| + |e\rangle\langle e|$, the atom's Hamiltonian reads simply

$$\mathcal{H}_a = \frac{\hbar\omega_a}{2}\sigma_z. \tag{3.30}$$

3.3 The Interaction $\mathcal{H}_{int}$

So far, resonator and qubit have been investigated separately. In this section, their interaction will be motivated, starting from a very general context of quantum electrodynamics (QED). The interaction model of choice will be the dipole coupling, which is also consulted when working with atoms in cavities in conventional cavity QED [61].

3.3.1 Quantum Electrodynamics: Dipole Coupling

The minimal coupling Hamiltonian describes an electron with unit charge e and mass m_e in an electromagnetic field with the vector and scalar potentials

$\mathbf{A}(\mathbf{r},t)$ and $U(\mathbf{r},t)$, the canonical momentum operator $\mathbf{p} = -i\hbar\nabla$ and the electrostatic potential $V(r)$:

$$\mathcal{H}_{\text{min}} = \frac{1}{2m_{\text{e}}}\big(\mathbf{p} - e\mathbf{A}(\mathbf{r},t)\big)^2 + eU(\mathbf{r},t) + V(r). \tag{3.31}$$

It can be derived from the Schrödinger equation of a free electron

$$-\frac{\hbar^2}{2m_{\text{e}}}\nabla^2\psi = i\hbar\frac{d\psi}{dt} \tag{3.32}$$

and the requirement of local gauge (phase) invariance, such that both the electron wave functions $\psi(\mathbf{r},t)$ and also $\psi(\mathbf{r},t)e^{i\chi(\mathbf{r},t)}$, with the arbitrary, locally varying phase $\chi(\mathbf{r},t)$, are valid solutions [62, 63]. While the probability density $P(\mathbf{r},t) = |\psi(\mathbf{r},r)|^2$ of finding an electron at position $\mathbf{r}$ at time t remains unaffected by a change of phase, the Schrödinger equation, Eq. (3.32), is not invariant under such a transformation. It needs to be modified to

$$\mathcal{H}_{min}\psi = i\hbar\frac{d\psi}{dt}. \tag{3.33}$$

For long wavelength compared to the size of the particle, the dipole approximation is valid. Further, using the radiation gauge [62–64] leads to a simplified version of the minimal coupling Hamiltonian $\mathcal{H}_{\text{dip}}$. For an electron at position $\mathbf{r}_0$ of Eq. (3.31) this is

$$\mathcal{H}_{\text{dip}} = \frac{p^2}{2m_{\text{e}}} + V(r) + \mathcal{H}_{\text{int}} \tag{3.34}$$

with an interaction term

$$\mathcal{H}_{\text{int}} = -\mathbf{d}\cdot\mathbf{E}(\mathbf{r}_0,t) \tag{3.35}$$

that is the well-known dipole coupling with the dipole operator $\mathbf{d} = e\cdot\mathbf{r}$.

3.3.2 Circuit Quantum Electrodynamics

In the case of a microwave resonator with an integrated transmon qubit, it is more natural to express the dipole coupling in terms of voltages instead of electric fields. If the transmon is positioned at an antinode of the resonator's standing wave electric field mode with resonance frequency ω_{r}, the AC gate voltage obeys

$$V_{\text{g}} = \frac{q}{C} = \sqrt{\frac{\hbar\omega_{\text{r}}}{2C}}(a + a^\dagger) = \mathcal{V}(a + a^\dagger), \tag{3.36}$$

where q is proportional to the previously used charge operator, and $\mathcal{V}$ is the root-mean-squared vacuum voltage of the LC oscillator. Also the gate charge

$$N_\mathrm{g} = \frac{C_\mathrm{g} V_\mathrm{g}}{2C} \tag{3.37}$$

can be expressed in terms of the AC gate voltage. The first term in the Hamiltonian of the CPB, see Eq. (3.23), can be expressed using the AC gate voltage V_g and gate charge N_g. If the square is expanded, a coupling term can be read off and simplified to

$$\mathcal{H}_{\mathrm{CPB,\,int}} = \hbar g (a + a^\dagger) N \tag{3.38}$$

with the coupling strength

$$g = \frac{C_\mathrm{g}}{C_\Sigma} \frac{e\mathcal{V}}{\hbar}. \tag{3.39}$$

The expression $2\hbar g$ represents the necessary energy to move one Cooper pair across a portion C_g/C_Σ of the root-mean-square vacuum voltage fluctuations $\mathcal{V}$ in the resonator.

3.3.3 Truncation to Qubit Space

Once again, if only a two-level subspace is considered, the charge operator N can be replaced by the Pauli spin operator $\sigma_\mathrm{z}/2$, which is identical to a sum of two atom transition operators

$$\sigma_\mathrm{x} \equiv \sigma_{ge} + \sigma_{eg} \equiv \sigma_+ + \sigma_-, \qquad \sigma_\mathrm{ij} = |i\rangle\langle j|, \tag{3.40}$$

where σ_+ and σ_- are yet just another common way of writing the atom's transition operators. Regarding all this, the interaction Hamiltonian reads

$$\mathcal{H}_\mathrm{int} = \hbar g (\sigma_+ + \sigma_-)(a + a^\dagger). \tag{3.41}$$

3.3.4 Rotating Wave Approximation (RWA)

Applying this approximation, in detail introduced in [65, 66], the rapidly rotating terms $a^\dagger\sigma_+$ and $a\sigma_-$ that are both not energy-conserving, are neglected. Finally, the applicable interaction Hamiltonian results to be

$$\mathcal{H}_\mathrm{int} = \hbar g \left(a\sigma_+ + a^\dagger\sigma_-\right). \tag{3.42}$$

3.3.5 The Jaynes-Cummings Hamiltonian

Before adding the last ingredient, the drive, to the gourmet soup $\mathcal{H}$, it is advisable to taste the thus-far concocted cuisine

$$\mathcal{H}_{\mathrm{JC}} = \mathcal{H}_{\mathrm{r}} + \mathcal{H}_{\mathrm{a}} + \mathcal{H}_{\mathrm{int}}, \tag{3.43}$$

a widely used model consisting of the preivously derived Hamiltonians of the cavity Eq. (3.11), the transmon qubit (3.30) and the coupling between them (3.42). Due to its broad application in cavity QED it has deserved a name on its own: The *Jaynes-Cummings Hamiltonian* [67] is

$$\mathcal{H}_{\mathrm{JC}} = \hbar\omega_{\mathrm{r}}\left(a^{\dagger}a + \frac{1}{2}\right) + \frac{\hbar\omega_{\mathrm{a}}}{2}\sigma_{\mathrm{z}} + \hbar g\left(a\sigma_{+} + a^{\dagger}\sigma_{-}\right). \tag{3.44}$$

The corresponding circuit is shown in Fig. 3.5.

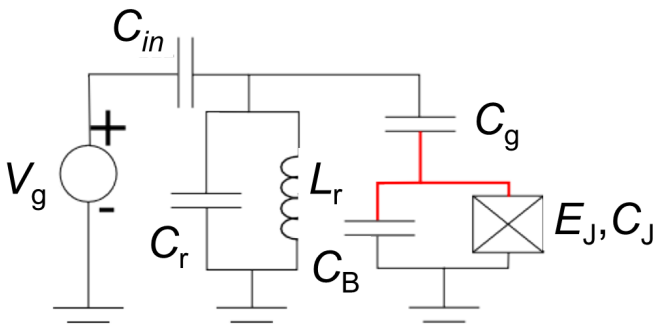

Figure 3.5: The effective circuit of the transmon. To the shunted Cooper Pair Box on the right, a resonator (LC oscillator) has been added in the center. The island is once more highlighted in red. Reprinted from [49].

The Jaynes-Cummings Hamiltonian Eq. (3.44) describes the system well, if cavity losses κ and interactions with other cavity modes γ are negligibly small $g \gg \kappa, \gamma$. It is instructive to look at the matrix form of the Jaynes-Cummings Hamiltonian, omitting constants,

$$\mathcal{H}_{\mathrm{JC}} = \hbar\begin{pmatrix} \omega_{\mathrm{r}}\left(a^{\dagger}a + \frac{1}{2}\right) + \frac{\omega_{\mathrm{a}}}{2} & -ga \\ -ga^{\dagger} & \omega_{\mathrm{r}}\left(a^{\dagger}a + \frac{1}{2}\right) - \frac{\omega_{\mathrm{a}}}{2} \end{pmatrix}. \tag{3.45}$$

Diagonalization yields a set of solutions, which mix the atomic eigenstates with the cavity eigenstates. The ground state is $|g, 0\rangle$ and the excited states are [68]

$$\begin{aligned} |+, n\rangle &= +\cos\theta_{\mathrm{n}}\,|e, n\rangle + \sin\theta_{\mathrm{n}}\,|g, n+1\rangle \\ |-, n\rangle &= -\sin\theta_{\mathrm{n}}\,|e, n\rangle + \cos\theta_{\mathrm{n}}\,|g, n+1\rangle \end{aligned} \tag{3.46}$$

with the mixing angle θ_n

$$\theta_n = \frac{1}{2}\tan^{-1}\left(\frac{2g\sqrt{n+1}}{\Delta}\right), \tag{3.47}$$

where the detuning Δ is

$$\Delta = |\omega_a - \omega_r|. \tag{3.48}$$

The eigenenergies are given by

$$\begin{aligned} E_{g,0} &= -\frac{\hbar}{2}\Delta, \\ E_{\pm,\,n} &= (n+1)\hbar\omega_r \pm \frac{\hbar}{\omega_r}\sqrt{4g^2(n+1)+\Delta^2}. \end{aligned} \tag{3.49}$$

In the two subsequent sections, two limiting cases, the *resonant* and the *dispersive* limit are explored.

3.3.6 The Resonant Limit ($\Delta \ll g$)

If the detuning is very small, which means effectively that $\omega_r \simeq \omega_a$, the artificial atom and the cavity are resonant. From the mixing angle in Eq. (3.47) it is evident that $\theta_n \simeq \pi/4$ and the eigenstates, Eq. (3.46), are equal combinations of "excited atom, n photons in the cavity mode" and "ground state atom, n+1 photons in the cavity mode". The spectrum is a set of doublets, which are all split by the coupling energy $2g\hbar\sqrt{n}$ (see Fig. 3.6).

In this case the absorption of cavity photons by the atom and the emission of them back to the cavity are energy-conserving. If an initally excited atom is prepared in the cavity, the combined system will be in equal superposition of the lowest doublet. It will oscillate with characteristic frequency $g\pi$, the *Rabi frequency*, between the two states $|g,1\rangle$ and $|e,0\rangle$. The process is called *vaccum Rabi oscillations* or *Rabi flopping* [50].

3.3.7 The Dispersive Limit ($\Delta \gg g$)

Here, the atom is considerably detuned from any cavity mode. No atomic transitions occur. Instead, virtual photons mediate dispersive interactions, which lead to energy level shifts proportional to

$$\chi = \frac{g^2}{\Delta} \tag{3.50}$$

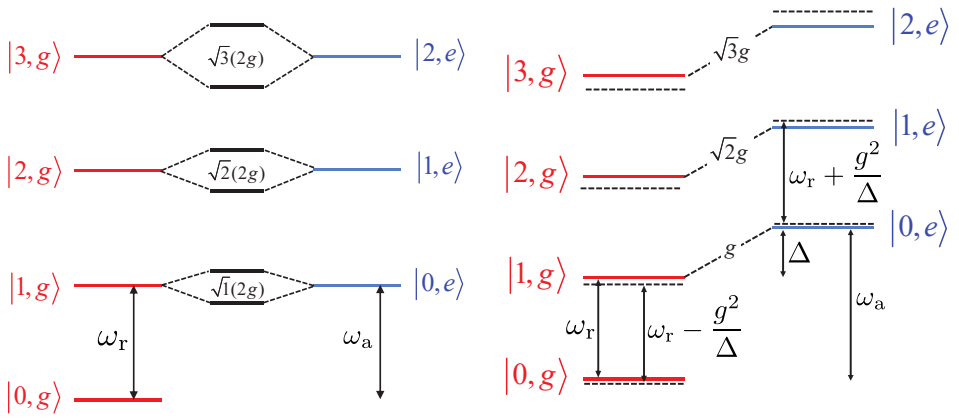

Figure 3.6: Energy spectrum in units of $\hbar$ of the Jaynes-Cummings Hamiltonian $\mathcal{H}_{\mathrm{JC}}$ of Eq. (3.44) in the resonant (left) and dispersive regime (right). Adapted from [51].

of the coupled system. More rigorously, the small argument suggests the approximation of Eq. (3.47) by

$$\sin\theta_{\mathrm{n}} \approx \frac{g\sqrt{n+1}}{\Delta}. \tag{3.51}$$

The eigenstates of Eq. (3.46) are then the ones from the unperturbed atomic Hamiltonian $\mathcal{H}_{\mathrm{a}}$ with a shifting term

$$\begin{aligned} |+,n\rangle &\approx |e,n\rangle + \frac{g\sqrt{n+1}}{\Delta}|g,n+1\rangle, \\ |-,n\rangle &\approx |g,n+1\rangle - \frac{g\sqrt{n+1}}{\Delta}|e,n\rangle. \end{aligned} \tag{3.52}$$

The Hamiltonian can be approximated with second-order time independent perturbation theory of the Jaynes-Cummings Hamiltonian in Eq. (3.44). To start with, it is transformed with the unitary transformation

$$U = e^{\frac{g}{\Delta}(a\sigma_+ + a^\dagger\sigma_-)}. \tag{3.53}$$

Then, the effective Hamiltonian is, to second-order in g/Δ,

$$U\,\mathcal{H}_{\mathrm{JC}}\,U^\dagger \approx \hbar\,(\omega_{\mathrm{r}} + \chi\sigma_{\mathrm{z}})\left(a^\dagger a + \frac{1}{2}\right) + \frac{\hbar\omega_{\mathrm{a}}}{2}\sigma_{\mathrm{z}}. \tag{3.54}$$

Like before, the first term is concerned with the cavity, whereas the second one is the qubit. Looking at the first part only, this arrangement of $\mathcal{H}_{\mathrm{JC}}$

illustrates nicely how the cavity frequency ω_r is shifted depending on the state of the qubit (σ_z-term). The cavity's resonance frequency is shifted to

$$\omega_r^{(g/e)} = \omega_r \pm \chi. \tag{3.55}$$

This qubit dependent frequency shift χ is detectable and the essential property for measurements of superconducting qubits. By probing the cavity's resonance frequency, the qubit state can be read out. For a qubit in $|g\rangle$ state, the resonance is at $\omega_r^{(g)} = \omega_r - \chi$ and for $|e\rangle$ it is at $\omega_r^{(e)} = \omega_r + \chi$.

Before investigating this possibility more closely, another way of writing Eq. (3.54) is educational. Simply rearranging the terms gives

$$U\,\mathcal{H}_{JC}\,U^\dagger \approx \hbar\omega_r\left(a^\dagger a + \frac{1}{2}\right) + \frac{\hbar}{2}\left(\omega_a + 2\chi a^\dagger a + \chi\right)\sigma_z. \tag{3.56}$$

In atomic physics this form is familiar. It emphasizes on the dual effect of the dispersive interaction. While before, the cavity frequency ω_r was shifted dependent on the qubit state (ground/excited state), now the qubit frequency ω_a is shifted according to the cavity state (photon number $n = a^\dagger a$). This is called the *AC Stark shift*. In analogy to before, where the qubit state was probed through the cavity's resonance frequency, here, the photon number state of the cavity can be probed through the qubit's resonance frequency [69, 70].

Another term has yet to be explained, namely, the additional shift of the qubit frequency by $\chi = g^2/\Delta$. It is constant and called *Lamb shift* in reminiscence of its origin in atomic physics [49]. The complete shift of the qubit frequency is, once again,

$$\omega_a^{(n)} = \omega_a + \chi(2n+1). \tag{3.57}$$

3.4 The Drive $\mathcal{H}_d$

The target is to find a way to access the qubit state for control and readout. In order to do so, a classical drive in form of another resonator

$$\mathcal{H}_r^{(2)} = \hbar\omega_d d^\dagger d, \tag{3.58}$$

with frequency ω_d and ladder operators $d^\dagger$ and d, is added to the model. Conceptually, this is a transmission line for microwave signals from the outside to the sample. Since the qubit is integrated in the cavity, it is not addressed directly. The control must act *through* the cavity due to its interaction with

the qubit. The external line will therefore be coupled to the cavity, with the interaction term

$$\mathcal{H}_\mathrm{d} = g_\mathrm{d}(a + a^\dagger)(d + d^\dagger), \tag{3.59}$$

where g_d is the coupling rate between the drive and the cavity. The qubit and the cavity are of interest and not the dynamics of the $\mathcal{H}_\mathrm{r}^{(2)}$, the complete Hamiltonian with all its ingredients can be written without it. That is

$$\mathcal{H} = \underbrace{\mathcal{H}_\mathrm{r} + \mathcal{H}_\mathrm{a} + \mathcal{H}_\mathrm{int}}_{\mathcal{H}_\mathrm{JC} \text{ of } (3.44)} + \mathcal{H}_\mathrm{d}. \tag{3.60}$$

The specific form of $\mathcal{H}_\mathrm{d}$ will be discussed in the following.

3.4.1 Modelling $\mathcal{H}_\mathrm{d}$

Assuming the drive cavity to be in a very highly-excited coherent state $|\beta\rangle$ and the coupling g_d to be very small, we can treat this cavity as remaining in $|\beta\rangle$ for all time[14]. The drive Hamiltonian then reads

$$\mathcal{H}_\mathrm{d} = (a + a^\dagger)(\xi e^{-i\omega_\mathrm{d} t} + \xi^* e^{i\omega_\mathrm{d} t}), \tag{3.61}$$

where $\xi = \epsilon\beta$ defines the strength of the drive, and β is referred to as displacement amplitude [71]. In the case that the driving is not too strong, it is possible to apply the rotating wave approximation again[15] [54] and get

$$\mathcal{H}_\mathrm{d} = a\xi^* e^{i\omega_\mathrm{d} t} + a^\dagger \xi e^{-i\omega_\mathrm{d} t}. \tag{3.62}$$

Because it is inconvenient to have a time-dependent Hamiltonian, the first unitary transformation will bring the Hamiltonian into the rotating frame of the drive. With the second unitary transformation, the *Glauber displacement transformation*, the action of the drive is directly shifted onto the transmon with the Glauber operator $d(\alpha) = e^{\alpha(t)d^\dagger - \alpha^*(t)d}$ for some time-dependent function $\alpha(t)$ [54, 71, 72]. For sufficient detuning Δ between cavity and transmon, the approximation of the dispersive limit applies, as was shown in Sec. 3.3.7. Finally, the discussion is truncated to the qubit space, ignoring far-detuned higher energy levels, analogous to the truncations in Sec. 3.2.5 and Sec. 3.3.3.

[14] A coherent state with complex amplitude β has the defining property of being an eigenstate of the lowering operator $\hat{d}|\beta\rangle = \beta|\beta\rangle$.

[15] That is, $\xi \ll \omega_{m,n}$ for all relevant transition frequencies $\omega_{m,n}$, e.g. $\langle m|(a + a^\dagger)|n\rangle \neq 0$.

3.4.2 The Finished Tincture $\mathcal{H}$

The complete Hamiltonian bouillon, destilled from all its constitutive ingredients and reasonably approximated, is then served as [73]

$$\mathcal{H} \simeq \hbar\left(\omega_\mathrm{r} - \omega_\mathrm{d}\right)\left(a^\dagger a + \frac{1}{2}\right) + \frac{\hbar}{2}\left(\omega_\mathrm{a} + 2\chi n + \chi - \omega_\mathrm{d}\right)\sigma_\mathrm{z} + \frac{\hbar\Omega_\mathrm{R}(t)}{2}\sigma_\mathrm{x}, \quad (3.63)$$

where $\Omega_\mathrm{R}(t)$ denotes the Rabi frequency. The Rabi frequency is the rate at which the state vector oscillates in the Bloch sphere. It will be used as the control parameter for acting quantum gates on the qubit, see Sec. 3.5. The dispersive shift of the cavity will be used for the readout, see Sec. 3.6.

3.4.3 The Transmonian Reality

It should be said that in the actual experiment the frequencies ω_r and ω_a itself may be shifted due to the large coupling strengths as well as the multilevel structure specific for the transmon. Substantially larger dispersive shift terms are obtained [50]. In a transmon, the dispersive shift is

$$\chi = \chi_{01} - \frac{\chi_{12}}{2} \qquad \text{with} \qquad \chi_\mathrm{ij} = \frac{g_\mathrm{ij}^2}{\omega_\mathrm{ij} - \omega_\mathrm{r}} \quad \text{and} \quad \omega_\mathrm{ij} = \omega_\mathrm{j} - \omega_\mathrm{i}, \quad (3.64)$$

rather than $\chi \approx g^2/\Delta$ from Eq. (3.50). For large detunings $\Delta \gg g$ the shift can be approximated by

$$\chi \approx \frac{g^2\alpha}{\Delta(\Delta - \alpha)}. \quad (3.65)$$

The characteristic frequencies are given by

$$\omega_\mathrm{r}' = \omega_\mathrm{r} - \frac{\chi_{12}}{2} \qquad \text{and} \qquad \omega_\mathrm{a}' = \omega_\mathrm{a} + \chi_{01}, \quad (3.66)$$

where ω_r' is shifted by $\pm\chi$ depending on the qubit state, as in Eq. (3.55), and ω_a' is (AC Stark) shifted by 2χ per cavity photon, as in Eq. (3.57).

3.5 Qubit Control

If the qubit frequency ω_a is well detuned from the cavity frequencies ω_r, driving the cavity with a frequency $\omega_\mathrm{d} \simeq \omega_\mathrm{a}$ far away from its frequencies $\omega_\mathrm{r} \pm \chi$ does not leak information about the qubit state. This poses an usable control port to the qubit.

One might wonder, why the signal even reaches the qubit, as the cavity is not resonant with the drive. Indeed, most of the radiation of the driving

microwave tone is reflected at the resonator input port, as can be seen in the expression for the reflection coefficient [74]

$$r(\omega_\mathrm{d}) = \frac{i\,(\omega_\mathrm{d} - \omega_\mathrm{r}) - (\kappa_\mathrm{in} - \kappa_\mathrm{ext})\,/2}{i\,(\omega_\mathrm{d} - \omega_\mathrm{r}) - (\kappa_\mathrm{in} + \kappa_\mathrm{ext})\,/2}. \tag{3.67}$$

However, a small portion of the power will enter the resonator and drive qubit transitions at the Rabi frequency $\Omega_\mathrm{R} \propto \sqrt{n_\mathrm{d}}$, where $n_\mathrm{d} = d^\dagger d$ is the number of drive photons inside the resonator. For large detunings of the drive frequency ω_d from the cavity frequency ω_r, that is $\Delta_\mathrm{d} = |\omega_\mathrm{d} - \omega_\mathrm{r}| >> \kappa/2$, the average number of drive photons is $\sqrt{n_d} \approx \epsilon_\mathrm{d}/\Delta_\mathrm{d}$. The coherent driving field can be considered a classical field with an amplitude ϵ_d and frequency ω_d [50].

The Rabi frequency $\Omega_\mathrm{R}(t)$, decomposed in its quadrature controls, is

$$\Omega_\mathrm{R}(t) = X(t)\,\cos(\omega_\mathrm{d} t) + Y(t)\,\sin(\omega_\mathrm{d} t). \tag{3.68}$$

This control parameter allows to rotate the qubit state vector on the Bloch sphere around an axis. Nothing objects the definition of this axis as x-axis. By shifting the phase of the drive signal, rotations around other axes with angle ϕ_R are feasible, most importantly around the y-axis with $\phi_\mathrm{R} = \pi/2$. In any case, the overall rotation angle θ_R will depend on the strength of the drive ϵ_d, or, in case of constant power, on the length of the applied drive t_d

$$\theta_\mathrm{R} = \int_0^{t_\mathrm{d}} dt\,\Omega_\mathrm{R}(t). \tag{3.69}$$

For instance, if $Y(t) = 0$, the rotation will be around the x-axis and vice versa. If such a rotation is applied for a time $t_\mathrm{d} = t_\pi$, the pulse will excite the qubit into $|e\rangle$, meaning the pulse is effectively a π-pulse or bit-flip gate. For a time $t_\mathrm{d} = t_{\pi/2}$ it is a $\pi/2$-pulse and the state becomes an equal superposition $(|0\rangle + |1\rangle)/\sqrt{2}$ [75]. For arbitrary angles, it is

$$|\psi\rangle = \cos\left(\frac{\theta_\mathrm{R}}{2}\right)|0\rangle + e^{i\phi_\mathrm{R}}\sin\left(\frac{\theta_\mathrm{R}}{2}\right)|1\rangle, \tag{3.70}$$

which proves universal control over a single qubit, when cross-checked with Eq. (2.5) [28]. However, there are further protocols for more efficient implementation of phase gates (rotations around z-axis). The AC-Stark gate or the flux gate are described in [75]. In practice, with careful calibration and pulse shaping, single qubit gates exceed fidelities, calculated from randomized benchmarking, of 99.9% routinely [7]. For this thesis similar protocols yielded > 99.85%, see Chap. 6.

3.6 Qubit Readout

As mentioned above, the dispersive shift of the cavity provides means to determine the state of the superconducting qubit. The question is now, how to efficiently detect the shift of the resonator's frequency. The change is for instance apparent in the *phase shift* between the sent and the received microwave signal[16]. A key feature of the readout mechanism is the possibility of a *Quantum Non-Demolition* (QND) measurement. The qubit collapses onto the measured state when the cavity is probed, but remains in this state thereafter, in contrast to being destroyed by the measurement procedure completely (e.g. photon polarization detection).

3.6.1 Readout in Transmission

The amplitude of the transmission coefficient shows the profile of Fig. 3.7. In the frequency range between $\omega_r' - \chi$ and $\omega_r' + \chi$, the two scenarios of $|g\rangle$ and $|e\rangle$ are well-distinguishable, in the amplitude of the transmission coefficient $|t|$, but even more so in the phase of the returned signal. In this region the phase shifts differ by π, giving maximum distance in the I-Q-quadrature plane.

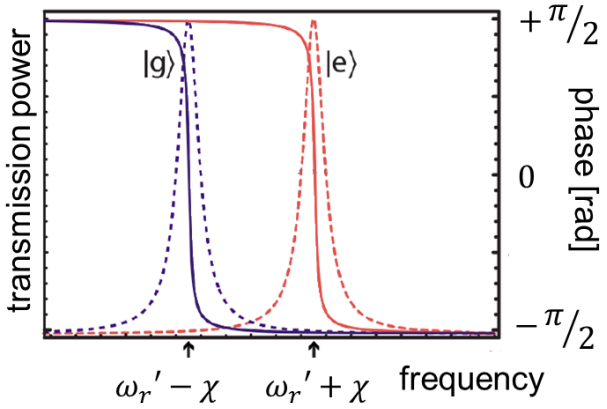

Figure 3.7: Readout in transmission. The peak profile is shifted conditioned on the qubit state. For drives near $\omega_r' \pm \chi$ the information is encoded in the transmission amplitude. Near ω_r' the phase shift of maximally π provides distinguishability. The linewidth of the peaks corresponds to the losses $\kappa = \kappa_{\text{int}} + \kappa_{\text{ext}}$. Adapted from [73].

[16] It is also apparent in the amplitude, which can be used for readout as well.

3.6.2 Readout in Reflection

The reflective readout differs only slightly from the above discussion. As can be seen in Fig. 3.8, the amplitude of the reflection coefficient $|r|$ exhibits dips instead of peaks. More interestingly, the maximal phase shifts differ by 2π, which poses a complication. Due the 2π-periodicity of the phase, the signals become indistinguishable. For vanishing internal losses κ_{int}, ideally, the dispersive shift χ equals the external losses κ_{ext}. Since the spectrum is narrower than before, the two dips are overlapping in a way, that the phase shifts differ by π in a well-accessible range of frequencies [45].

Generally, for any κ_{ext}, κ_{int} and χ values

$$\arg\big(r(\omega_{\text{ro}}, \omega_{\text{g}}')\big) - \arg\big(r(\omega_{\text{ro}}, \omega_{\text{e}}')\big) = \pi \tag{3.71}$$

should be solved for the optimized readout frequency ω_{ro}.

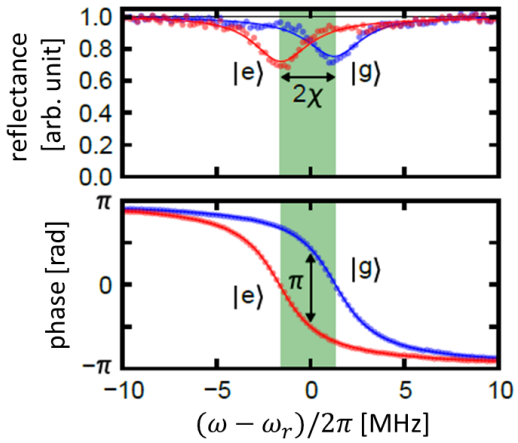

Figure 3.8: Readout in reflection. With measurements in transmission, the phase shift is always smaller than π, while for measurements in reflection, one can for optimize for the ideal phase difference of π at frequency ω_{ro}. The squared amplitude (reflectance) and the phase shift of the cavity reflection coefficient are plotted as a function of the probe frequency, with the qubit being in the ground state (blue) or the excited state (red). Dots are experimental results, continuous lines represent the fitted curves. Reprinted from [45].

3.7 Enlightning Remarks

At this point it is noteworthy, that although this thesis uses a transmon qubit integrated in a 3D cavity measured in reflection, the derivation holds true also for coplanar waveguide (2D) architecture with transmission line resonator. The dynamics of both are covered with the Jaynes-Cummings Hamiltonian $\mathcal{H}_{\mathrm{JC}}$ in Eq. (3.44).

Another comment about dissipation and the strong dispersive limit. Cavity and qubit suffer from dissipation, giving them certain linewidths. For the cavity the linewidth is $\kappa/2\pi$, which is related to its lifetime $T_{\mathrm{cav}} = 1/\kappa$. The qubits lifetime is its coherence time $T_1 = 1/\gamma$, often set by the off-resonant decay through the cavity known as the *Purcell effect* [75].

The strong dispersive limit is defined as the regime, where $\chi > \gamma, \kappa$. The cavity will shift there more than a linewidth according to the qubit state, hence, yielding highly projective measurement.

Chapter 4 Experimental Setup

The wiring diagram in Fig. 4.1 used for single shot measurements is also representative for the averaged ensemble measurements of this thesis. All communication between the computer and the experimental devices is done via their GPIB interface. LABrad software is used to automate the measurement procedures. Long term phase stability and synchronization is achieved by phase locking all signal generators, arbitrary wave generators (AWG) and acquisition cards with the ultra low phase noise 10 MHz Rubidium frequency standard Model FS725 from *Stanford Reserach Systems*.

4.1 Dilution Refrigerator

For the Josephson junction to work as well as to see quantization in the circuit in the first place, the sample, comprising cavity and qubit, must be cooled to cryogenic temperatures. For this a Triton 200 Cryofree dilution refrigerator from *Oxford Instruments* was used. Its base temperatures are < 10 mK, however, the experiments in this thesis were carried out at a temperature $60 \sim 75\,\mathrm{mK}$ due to unwanted, but unknown continuous warming.

The primary cryogenic design concern is to minimize the amount of heat and noise that reach the sample. There are four lines, three of them input and one output. The input lines are for qubit control, JPA control and readout. The output line is for the reflected signal of the readout pulse that holds the information about the state of the qubit. While the first three must be attenuated carefully to transform room temperature signals to very low power scales of −140 dBm, the output signal must be amplified accordingly.

Thermal Johnson noise coming down the cables would constitute an unacceptable noise source and must be filtered by lowering its effective temperature via cold attenuation. In the low effective-temperature limit, voltage noise is linear in temperature $S_\mathrm{V}(\omega) \approx 4k_\mathrm{b}TR$ [76]. At the cold stage, one can just attenuate by a factor $T_\mathrm{hot}/T_\mathrm{cold}$.

Attenuators at the lowest temperature stage dissipate the energy there and cause heating of the fridge, when chosen carelessly. One wants to attenuate the signal in previous stages of the refrigeration in a way that it matches the temperature of the subsequent chamber. For instance, a signal in the 4 K segment should be attenuated by -10dB to continue into the coolest chamber of 40 mK (also called OCV chamber). In the setup, for going from room temperature (290 K) to liquid helium temperature (4 K), a 16 dB attenuation is used. Proceeding from 4 K to 20 mK, the linear dependance breaks

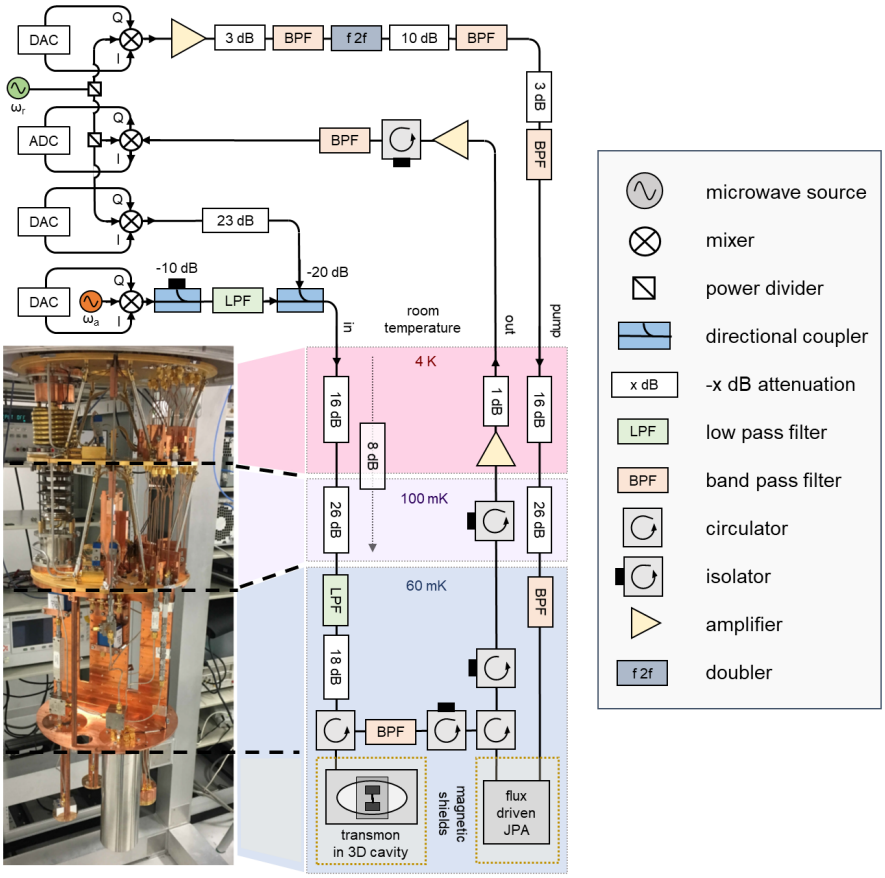

Figure 4.1: Schematic wiring diagram of the experimental setup at room temperature (top) and inside the dilution refrigerator (bottom). A photograph of the dilution refrigerator shows the stages of descending temperature. The shown setup works for averaged and single shot readout, where the latter uses the JPA.

down [50], and another 26 dB attenuation is used. The cables leading down the dilution refrigerator provide additional 8 dB attenuation, for a total of 50 dB. Measurement needs only a few photons, corresponding to approximately −128 dBm, and 12 ns control pulses typically involve a few thousand photons in the range of −80 to −90 dBm.

To filter out unwanted frequencies the *RLC Electronics* standard low pass filter F-30-12.4-R and the *Marki Microwave* bandpass filter F19614 are used. To protect the sample from noise that could enter the resonator from the output side, the signal is directed through two *Aerotek* shunted circulator isolators XTE0812KI and XTE0812KS. One of the three ports is termi-

nated, which makes the circulators acting similar to a one-way microwave valve called isolator. It uses a ferrite component to break time reversal symmetry [76]. The circulators have about 20 dB isolation and, in this setup, a bandwidth of $8 \sim 12$ GHz.

The signal power after the interaction with the sample is very small, especially considering the presence of thermal photons and amplifier noise. In averaged measurements, a croygenic high electron mobility transistor (HEMT) amplifier at the 4 K stage in the output line with an additional isolator suffices to acquire a sufficient signal-to-noise ratio.

For single shot measurements on the other hand an additional flux-driven Josephson parametric amplifier (JPA) is required that works near the quantum limit. The JPA resonance frequency is tuned to the cavity resonance frequency ω_r by applying a DC magnetic field into the SQUID loop. The JPA is pumped via a separate input line at $2\omega_\mathrm{r}$ for the operation in the degenerate mode.

4.2 Pulse Generation

The goal is to quickly change electromagnetic signals at a well-defined microwave frequency, which is equivalent to send nanosecond long microwave pulses. The microwave sources, also referred to as radio frequency (RF) sources, are E8257D PSG analog signal generators from *Agilent Technologies*. In Fig. 4.1, they are labeled as *DAC* or *ADC*, digital-to-analog or analog-to-digital convertes, respectively. Such sources cannot supply the necessary fast switching. Their high GHz frequency signals from the local oscillator (LO) are modulated with an intermediate frequency (IF) signal (≈ 100 MHz) from the AWG, *Agilent Technologies* PNA-L network analyzer N5232A Keysight[17],

$$V_\mathrm{ct} = A_\mathrm{LO}\ \cos(\omega_\mathrm{LO} t)\big(A_\mathrm{IF}\cos(\omega_\mathrm{IF} t) + V_\mathrm{IF}\big). \tag{4.1}$$

The AWG is capable of generating pulses with 1 ns resolution [76]. Pulse sequences are designed in Mathematica and loaded into the AWG memory. The control pulses are Gaussian shaped, because of the minimum bandwidth of Gaussian envelopes. In a more elaborate scheme, derivative reduction by adiabatic gates (DRAG) pulses will be used instead for this thesis, see Sec. 5.3. The readout pulses are squared pulses of considerable bigger pulse width.

The intermediate frequency is generated by a digital-to-analog converter (DAC) at 1 GHz sampling rate and filtered with a low-pass filter with a cut-off frequency of ≈ 100 MHz. The modulation is done by mixers IQ0318L

[17] Also referred to as vector network analyzer (VNA).

from *Marki Microwave*, with three input ports. One is the local oscillator, the other two are for the quadratures I and Q

$$I = \frac{2}{T}\int_T dt\, S_{\mathrm{IF}}(t)\cos(\omega_{\mathrm{IF}}t), \tag{4.2}$$

$$Q = \frac{2}{T}\int_T dt\, S_{\mathrm{IF}}(t)\sin(\omega_{\mathrm{IF}}t), \tag{4.3}$$

of the intermediate frequency signal

$$S_{\mathrm{IF}}(t) = I\cos(\omega_{\mathrm{IF}}t) - Q\sin(\omega_{\mathrm{IF}}t) = A\cos(\omega_{\mathrm{IF}}t + \theta), \tag{4.4}$$

where T is any chosen period interval. Here, the amplitude and the phase of the IF signal are

$$A = \sqrt{I^2 + Q^2}, \qquad \theta = \tan^{-1}\left(\frac{I}{Q}\right). \tag{4.5}$$

The amplitude and phase of the RF signal can be adjusted by simply changing the applied voltages to the I and Q ports of the mixer. The intermediate frequency can now be chosen to be zero, $\omega_{\mathrm{IF}} = 0$ (homodyne mode or direct modulation) or finite $\omega_{\mathrm{IF}} \neq 0$ (heterodyne mode or sideband modulation). Heterodyne mode is chosen with an IF frequency of 100 MHz [50].

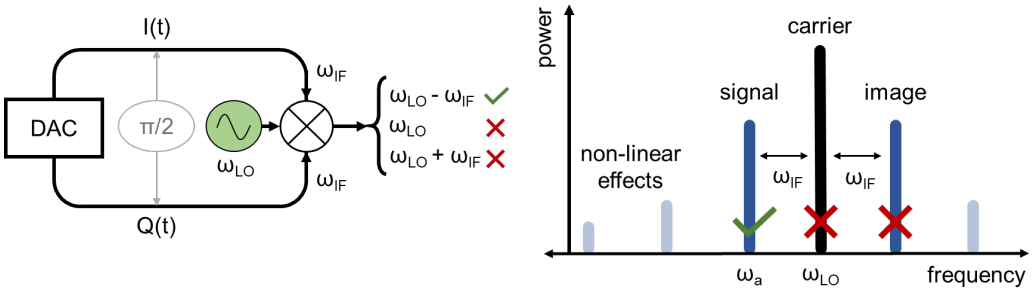

Figure 4.2: (Left) The pulse generation in the mixing process of the local oscillator ω_{LO} and the intermedie frequencies ω_{IF}. (Right) Schematic of mixing result before DAC calibration. After calibration spurious carrier and image frequencies are suppressed, non-linear effects of the mixer are negligible. The signal frequency dominates. Notation follows Fig. 4.1.

The resultant signal has three portions: a centered carrier at $\approx$ 7.9 GHz and two symmetric sidebands $\approx 7.9 \pm 0.1$ GHz, see Fig. 4.2. In heterodyne

mode, one of the sidebands is chosen (7.9−0.1 GHz) to be the qubit frequency ω_a to control the qubit. The carrier and the other sideband must then be suppressed.

With the DC offset of the I and Q channels, the tone at the LO frequency due to IQ leakage can be cancelled. This suppresses the *carrier*. The other sideband, called *image*, is present due to the existence of either skewness, where the quadratures are not perfectly phase-separated by $\pi/2$, or amplitude imbalance between the quadrature components. It can be suppressed by setting the quadrature amplitudes I and Q and the phase difference $\theta = \pi/2$ with the techniques described in [71].

A DAC calibration renders these optimal values for a given span of control and sideband frequencies. It is recommended to run a calibration check in the beginning of a measurement series in order to confirm the suppression and the experimental relation between pulse amplitude and signal power. Preferably, the relative suppression of carrier and image is in the order of 30 dB relative to the microwave signal. This suppression value would cause a maximal rotation error of $\pi/1000$ in a π-rotation.

It is recommendable to choose the sideband frequency in a way that neither carrier nor image fall onto another resonance of the sample. In the given system, the anharmonicity $\alpha \approx 300$ MHz endangers for instance a sideband frequency of 150 MHz, as the image would fall exactly onto the transition frequency for the higher transmon states, hence, cause unwanted leakage. The same accounts for other frequencies, generated by non-linear effects of the IQ mixer. The choice of 100 MHz is herewith underpinned.

4.3 Demodulation

The state of the qubit is encoded in the phase and the amplitude of a pulse reflected at ≈ 10 GHz. The eventual goal is to acquire the values digitally on the computer, but unfortunately no acquisition board can stably work at 10 GHz. The signal is therefore mixed down to an intermediate frequency by an IQ demodulator. The two quadratures of this IF signal can subsequently be down-converted to anywhere below 500 MHz and are then amplified before being processed by an *Acqiris* data acquisition board. With this board, extremely large amounts of data can be processed in short time at the given high sampling rates. For any measurement which studies ensembles (averaged measurement), the acquisition board will allow up to $2^{16} \approx 65.000$ averages to be taken without having to transfer the buffer to memory [76].

Ensemble measurements average over the voltage signal to cancel out certain noises such as additional photons in the cavity, additional photons due to amplification, etc. The demodulation happens after the averaging.

With the Josephson Parametric Amplifier (JPA) it is possible to amplify a microwave signal at cryogenic temperatures with minimal photon noise of approximately 0.5 photons. Room temperature HEMT amplifiers, in comparison, contribute circa 20. In single shot measurement every signal is demodulated separately, which renders post-selection protocols possible.

In reflective measurements, the demodulation window must be chosen accordingly to avoid demodulation of a purely reflected signal that has not impinged the cavity and therefore does not hold any information about the qubit. Also, in the experiments of the thesis, the demodulation was unweighed, meaning that in a given temporal window, all voltage signals were equally taken into account.

4.4 Cavity and Qubit

The present transmon qubit of "batmon" design is mounted at the center of a 3D superconducting cavity. The qubit with an aluminium/aluminium oxide/aluminium Josephson junction is fabricated on a sapphire substrate ($5 \times 5\,\mathrm{mm}$). The cavity is made of aluminium (A1050) and has a single SMA-connector[18] port connected with a coaxial cable, see Fig. 4.3. Such a setup would suffice for averaged measurement, but in order to execute single shot measurements, the cavity output is connected to the JPA. The JPA is fabricated on a silicon substrate of the size $2.5 \times 5\,\mathrm{mm}$ [45] and not shown in this section.

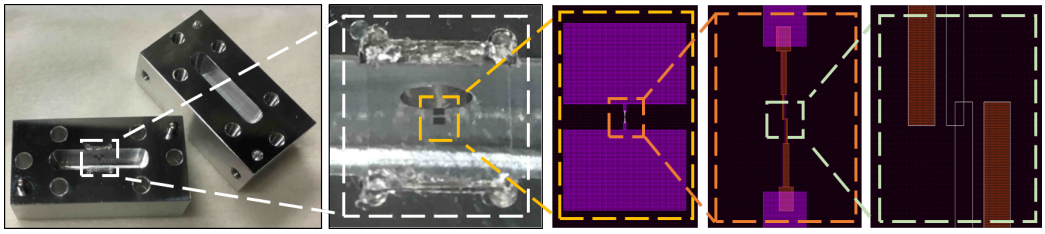

Figure 4.3: From left to right: (1) Photo of an opened 3D cavity. (2) Photo of the mounted silicon waver with the qubit in the center. (3) Digital sketches of the qubit with two squared capacitor pads (purple), from which (4) filigrane lines (auburn) lead to the Josephson junction (5).

[18] SubMiniature Version A are coaxial RF connectors with a $50\,\Omega$ impedance and a typical passband of $0 - 18\,\mathrm{GHz}$.

Chapter 5 Sample Characterization

5.1 Continuous Wave (CW)

After a sample is put in the dilution refrigerator (see Sec. 4.1) and cooled down, the basic device parameters must be determined. The suite of experiments is

- **Cavity reflection**: bare $\omega_{\mathrm{r}}^{\mathrm{bare}}$ and dressed $\omega_{\mathrm{r}}^{\mathrm{g}} \equiv \omega_{\mathrm{r}}$ cavity frequency.
- **Qubit spectroscopy**: qubit transition frequencies $\omega_{ge} \equiv \omega_{01} \equiv \omega_{\mathrm{a}}$ and $\omega_{ef} \equiv \omega_{12}$; from these the anharmonicity α.
- **Dressed cavity spectroscopy**: Cavity resonances for a qubit in ground $\omega_{\mathrm{r}}^{\mathrm{g}}$ and excited state $\omega_{\mathrm{r}}^{\mathrm{e}}$; the dispersive shift $\chi = (\omega_{\mathrm{r}}^{\mathrm{g}} - \omega_{\mathrm{r}}^{\mathrm{e}})/2$; the coupling g between cavity and qubit.
- **Cavity linewidth**: losses/linewidth κ of the cavity at qubit frequency $\omega_{\mathrm{r}}^{\mathrm{g}}$; for reflection measurement, internal κ_{int} and external losses κ_{ext}; the single photon power P_{single} and the coupling regime through the ratio of external and internal losses $\kappa_{\mathrm{ext}}/\kappa_{\mathrm{int}}$ (overcoupling, critical coupling or weak coupling).
- **(Dressed qubit spectroscopy AC Stark shift)**: Qubit shifts due to photons in the cavity modes, called the AC Stark shift. Not treated in this thesis.

The experiments are ordered in the Tab. 3, depending on which parameter on which device is swept. The parameters are frequency f or power P; the sources are the vector network analyzer (VNA) for the cavity or RF source for the qubit. This chapter profited from the structure of [71].

5.1.1 Cavity Reflection

The most basic measurement is to find the resonance frequencies of the cavity by measuring the absolute value of the reflection coefficient $|r|$ from Eq. (3.67) as a function of frequency[19]. Obviously, knowing the resonator's frequencies is necessary for qubit measurements. It also verifies a correct setup in terms of powered amplifiers, wiring, etc. A fast option is to use the VNA.

[19] For the widely used transmission line resonator the transmission amplitude $|t|$ through the ports is measured instead.

	VNA		RF	
	frequency	power	frequency	power
Cavity reflection	swept	stepped	–	–
Qubit spectroscopy	fixed	fixed	swept	swept
Dressed cavity spectroscopy	swept	fixed	fixed	fixed
Cavity linewidth	swept	fixed	–	–
AC Stark Shift	fixed	swept	swept	fixed

Table 3: Continuous wave (CW) experiments and the parameters that are changed on the respective device. They are either kept constant (fixed), chosen to be certain values in different orders of magnitude (stepped) or continuously changed over a defined range (swept).

The power that should be used is rather important, because of the cavity anharmonicity that is inherited from the qubit. For low power (roughly 1 photon mean excitation of the cavity) a Lorentzian reflection dip is centered at the dressed cavity frequency ω_r^g (Fig. 5.1a). For high VNA power of about +50 dB to the previous settings the bare cavity frequency $\omega_r^{bare} < \omega_r^g$ will be visible as another Lorentzian dip. The cavity is then *undressed*, meaning that the cavity shows resonance as though there was no qubit. In between these power orders, the cavity reveals a strongly nonlinear response. It indicates the presence of a qubit that is hybridizing with the cavity (Fig. 5.1b).

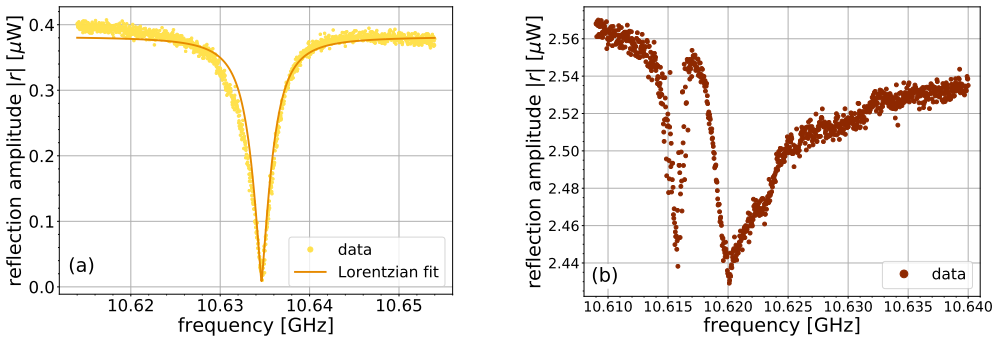

Figure 5.1: Cavity reflection with different VNA powers. (a) Low power of −20 dBm for the dressed cavity resonance. (b) Medium power of 15 dBm, with a spectrum in the bifurcation between dressed and bare cavity. For higher power this would turn into a single dip at the bare cavity frequency.

5.1.2 Qubit spectroscopy

The simplest conceptual version of spectroscopy is known as pulsed spectroscopy. The pulse could either be some fast gaussian rotation or a long continuous-wave (CW) microwave tone. In the CW-spectroscopy the frequency of a long saturation tone (longer than T_2) is swept. It will drive some equilibrium incoherent population of the qubit in the excited state. The population is relatively insensitive to pulse power.

However, there is an equilibrium population of photons in the cavity. Qubit transitions that depend on the number of photons will be visible. The condition for this to happen is that the shift per photon $2\chi \gg \kappa, \Delta f$ is much larger than the cavity and the qubit linewidth. From the part of the Hamiltonian in Eq. (3.56), which is affecting the qubit, it can be seen that the qubit transition frequency changes with the number of photons in the cavity. For this, the factors in front of the qubit σ_z operator are

$$\frac{\hbar}{2}(\underbrace{\omega_a + \chi}_{\omega_a'} + 2n\chi) \tag{5.1}$$

and reveal a qubit transition frequency of $\omega_a' + 2\chi$ for one photon, $\omega_a' + 4\chi$ for two photons and so on. If there is a superposition of photon number states, the qubit transition frequency suffers *number splitting*. It is either resolved or broadens the qubit response.

When using long saturation tones for spectroscopy, the drive strength is of importance. For low drive power, the qubit linewidth Δf is set as $1/T_2$. For higher powers the behavior is

$$2\pi\Delta f = \sqrt{\frac{1}{T_2^2} + 4\Omega_R^2 \frac{T_1}{T_2}}, \tag{5.2}$$

where qubit lifetime T_1 and dephasing time T_2 are described in Sec. 5.2, and Ω_R is the drive Rabi rate from Eq. (3.63). The drive causes stimulated emission of the qubit, causing a reduction of T_1, hence also T_2, which broadens the linewidth as exhibited. Power broadening is a convenient effect though. Without it the narrow qubit responses of today's 3D architectures would be difficult to spot. Through measurements with different drive powers, one can find the *genuine* qubit linewidth by extrapoliting the behavior according to Eq. (5.2), depicted in Fig. 5.2b.

A larger spectroscopy power can also drive higher qubit transitions. For substantially higher power, a two photon transition, directly from ground state to the second excited state $|g\rangle \rightarrow |f\rangle$ happens at the transition frequency $\omega_{gf} \equiv \omega_{02}$. The effect is very useful to determine the anharmonicity α, because

the transition frequencies are related with $\omega_{02/2} = (\omega_{01} + \omega_{12})/2$ and therefore

$$\alpha = 2(\omega_{02/2} - \omega_{01}). \tag{5.3}$$

The higher transition resonances can be seen in Fig. 5.2a, from which the power broadening of Fig. 5.2b is already evident.

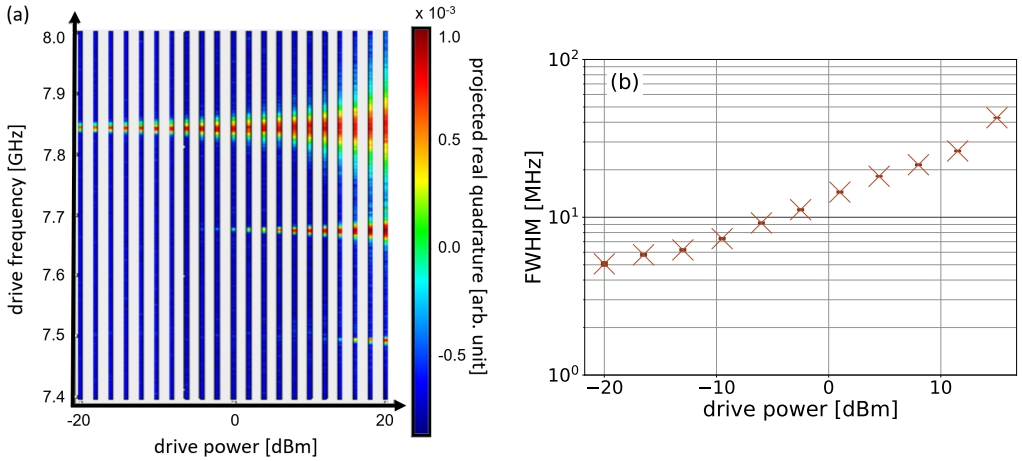

Figure 5.2: (a) Qubit spectroscopy for various RF drive powers and frequencies. The color indicates the amplitude of the reflection coefficient. The top spike is at the qubit resonance frequency $\omega_a \equiv \omega_{01}$, the bottom one is the transition $|1\rangle \rightarrow |2\rangle$ at ω_{12}. Between them lies $\omega_{02/2}$, at which the two-photon transition $|0\rangle \rightarrow |2\rangle$ occurs. (b) The FWHM from the main transition $|0\rangle \rightarrow |1\rangle$ plotted against the drive power to find the *genuine* qubit linewidth in the limit case of a zero-power excitation pulse. The bars in the center of the data points are the uncertainties of the fitted model.

5.1.3 Dressed cavity spectroscopy

Due to the qubit state the cavity frequency is given a dispersive shift

$$\omega_r^{e,g} = \omega_r \pm \chi, \tag{5.4}$$

visible in Fig. 5.3. The simple dispersive shift from Eq. (3.50) of $\chi \approx \frac{g^2}{\Delta}$ has been approximated in the more realistic setting of the transmon by Eq. (3.65). In this thesis χ is determined experimentally through the two distinct dips.

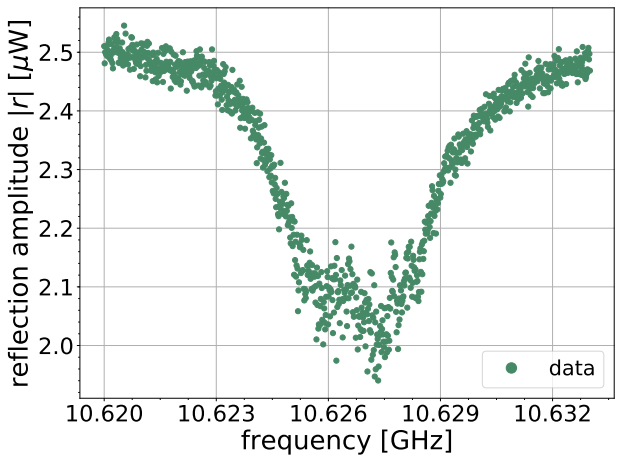

Figure 5.3: Smeared dispersive shift. The two small dips indicate the dispersive shift of the cavity dependent on the qubit state.

5.1.4 Cavity linewidth

From the Lorentzian fit in Fig. 5.1a, the cavity linewidth κ is determined. The single photon power P_{single} follows straight from it through

$$P_{\text{single}} \approx \hbar\omega_{\text{r}}^{\text{g}}\kappa, \tag{5.5}$$

and the components of $\kappa = \kappa_{\text{ext}} + \kappa_{\text{int}}$ are given in [76]. The mean photon lifetime in the resonator is the inverse of κ. The experimental situation for $\kappa_{\text{ext}} \gg \kappa_{\text{int}}$ is called *strong coupling regime*, in contrast to *weak coupling* for $\kappa_{\text{ext}} \ll \kappa_{\text{int}}$ or *critical coupling* at $\kappa_{\text{ext}} = \kappa_{\text{int}}$.

The internal losses κ_{int} consist of defects in the superconducting material of the cavity (e.g. Al) and the surface (e.g. AlO). Small resistances cause heating and this energy is dissipated into the environment. The external losses κ_{ext} are energy losses into connection lines (wires). They are modified by the manual positioning of the cavity pin before putting the sample into the fridge.

For critical coupling the phase shifts in the readout differs by 2π, impeding distinction between ground and excited state, see Sec. 3.6.2. However, in the reflection measurement a reference signal level is given and from the Lorentzian fit it is possible to calculate both κ_{ext} and κ_{int}. In a transmissive measurement on the other hand, the maximal signal is not known and therefore only κ can be determined; internal and external losses have to be estimated otherwise.

The coupling strength g is found by massaging Eq. (3.65) into

$$g = \sqrt{-\chi \frac{\Delta(\Delta - \alpha)}{\alpha}}, \tag{5.6}$$

where Δ is the detuning from Eq. (3.48). The critical photon number n_{crit}, above which the assumption of the dispersive regime breaks down, is then given by

$$n_{\text{crit}} = \left(\frac{g}{2\Delta}\right)^2. \tag{5.7}$$

5.2 Time Domain (TD)

All the experiments discussed thus far, have been CW measurements and spectroscopic in their nature. In time domain experiments well-timed pulses in lieu of continuous microwave tones are used.

5.2.1 Rabi measurements

One of the simplest TD experiments with a qubit is a *Rabi oscillation*. The state of the qubit is rotated about the x-axis of the Bloch sphere via the application of a resonant microwave pulse as outlined in Sec. 3.5. The projective measurement on the z-axis reveals the oscillation.

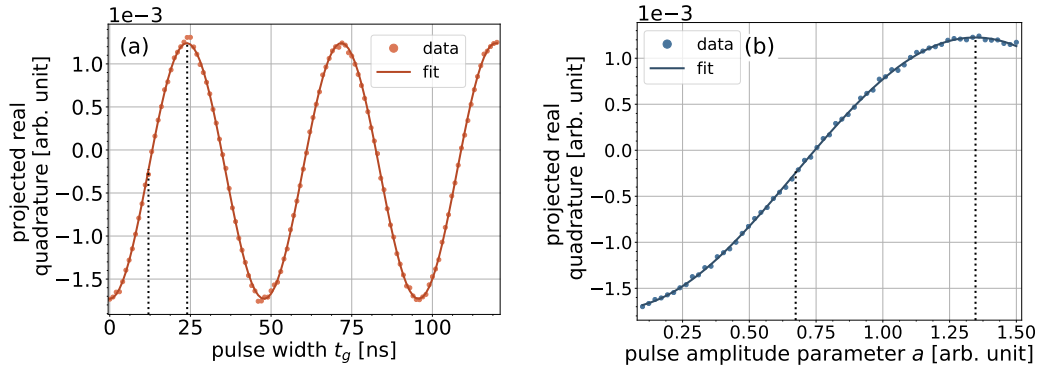

Figure 5.4: (a) Rabi oscillations in time with constant amplitude that corresponds to a $\pi/2$-rotation in 12 ns. (b) Rabi oscillations in pulse amplitude for a constant pulse width of 12 ns. The dotted lines indicate $\pi/2$- and π-rotations of the fitted sine curve.

There are two common versions of Rabi oscillations, a "time Rabi" and a "power Rabi", showcased in Fig. 5.4. In the first one, the amplitude of the

pulse is fixed and the driving time t_d, pulse length, is increased. A longer pulse corresponds to a longer rotation, yielding a greater rotation angle θ_R. From this, the Rabi rate Ω_R can be fitted according to the probability of finding the state $|\psi\rangle$ in the excited state $|e\rangle$

$$|\langle\psi|e\rangle|^2 = \sin^2\left(\frac{\Omega_R\, t_d}{2}\right). \tag{5.8}$$

For a fixed amplitude, the length $t_{\pi/2}$ for a $\pi/2$-rotation is obviously half of the gate time t_π for a π-rotation. For certain protocols it is however desirable to have $t_{\pi/2} = t_\pi$ for both control pulses; furthermore, the amplitude resolution of the AWG is typically much better than its time resolution. For this purpose, in the "power Rabi" the pulse length t_d is fixed to a constant and the amplitude of the pulse is varied. Now, the $\pi/2$-rotation will require a pulse with half the amplitude of the π-rotation, but both of them are equally long. The two Rabi versions are equivalent in terms of their underlying physics, both confirming the sinusoidal response.

The Rabi oscillation serves also as an overall check. Generally, a good Rabi oscillation stands for carefully tuned parameters and it will be perfectly uniform over time in the limit of a true two-level system. Other disruptive factors are a qubit's bandwidth Δf close to the anharmonicity α of the system, or the hybridization of the qubit with some other degree of freedom (quasiparticles on the superconducting island). The latter results in beating signals, that is a additional decaying modulation of the signal.

5.2.2 Ramsey

The Ramsey measurement serves two purposes. First, it improves the rough qubit frequency estimate, which is used for the control; and second, it gives the decoherence time T_2^*, as explained later in Sec. 5.2.5. The Ramsey oscillation is the gold-standard of frequency calibration for qubits [71] as well as for precision instruments like atomic clocks [77].

The idea is to utilize that the detuning of the qubit frequency δ of the qubit from the RF generator frequency reference looks like a z-gate being continuously applied at a rate δ. Even smallest detunings of a few kilohertz are detectable, thus, correctable. In order to distinguish between the exponential decay caused by dephasing and the oscillation caused by the detuning, it is desirable to have a few oscillations in the first two $1/e$ times. Practically, the control frequency is intentionally detuned from your estimate by $\approx 1\,\mathrm{MHz}$. The frequency of a 3D transmon was recently measured to better than 100 Hz [78]. Experiments in this thesis have an accuracy better than 1 kHz, see Tab. 4.

5.2.3 Energy relaxation time T_1

The processes of energy relaxation and decoherence are typically described by timescales referred to as T_1 and T_2, respectively. However, more advanced measures like T_2^* and T_2^{echo} have even made their way into tutorials [79] and will be shortly outlined here.

The protocol to determine T_1 is to apply a π-pulse for excitation, e.g. a X_{180}-gate. Between pulse and measurement there is a delay time t, which is increased to multiples of the expected coherence time. A fit to the expenontial decay $I(t) = c_1 \exp(-t/T_1) + c_2$ in quadrature signal I gives an estimate on T_1. The coherence time is expected to be in the order of 20 µs, so idle time is increased up to 100 µs, see Fig. 5.5a.

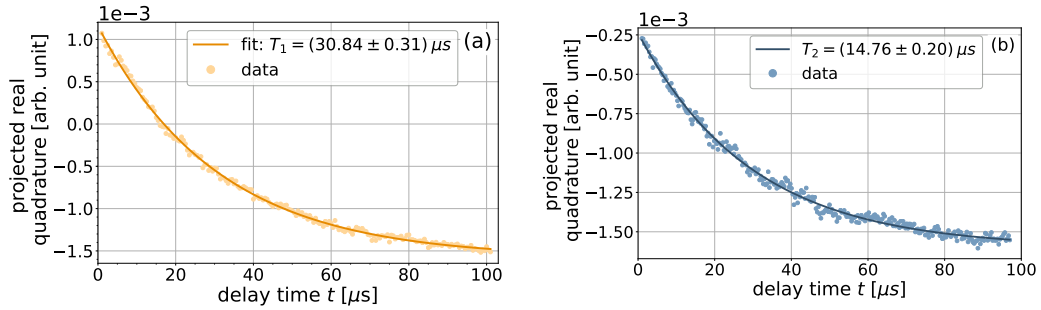

Figure 5.5: Fit of (a) the energy relaxation rate T_1 and (b) the coherence time T_2 as exponential decays.

5.2.4 Coherence time T_2

The qubit is prepared in a superposition state $|x+\rangle$ with a Y_{90}-gate, which is a $\pi/2$-rotation around the y-axis, and later measured in the x-direction. If another Y_{90}-gate was applied immediately after the first, the excited state $|1\rangle$ would be acquired. It would have been a Y_{180} operation in two steps. If the time until the second operation is increased, the qubit looses some of the phase information in decoherence processses. Slowly, the measurement results will converge towards 50% ground state and 50% excited state, which is the result of a measurement in any basis of a maximally mixed state. The continuous cooling process of the sample will push the maximally mixed state back to ground state. The curve for the decoherence process is the exponential decay in Fig. 5.5b, from which the rate T_2 is evaluated.

5.2.5 The more accurate coherence time T_2^*

There exists an inherent issue with the above procedure about measuring T_2. If it was followed as described, a decay of characteristic time T_2 is observed, but with a strong dependence of the control frequency ω_a. If the control frequency is only slightly detuned, subtle Ramsey oscillation occurs. Since the detuning is very small, the first Ramsey fringe would be very long and weak and affecting the model of the exponential decay severely. By increasing the detuning deliberately, Ramsey oscillations become clearer and the errors in estimating the coherence time are mitigated.

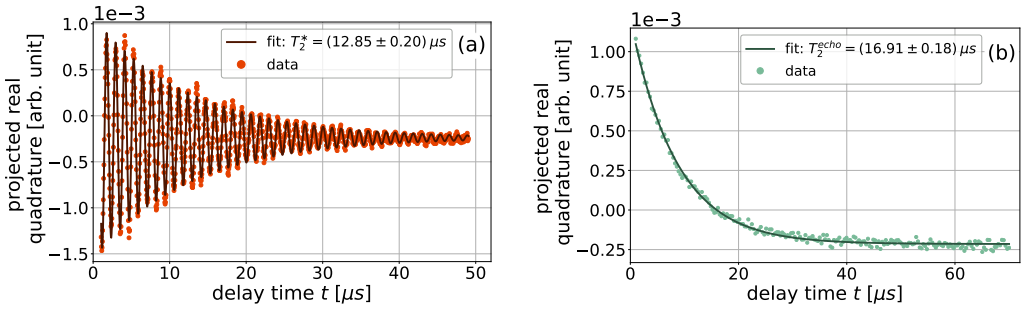

Figure 5.6: (a) Experimental Ramsey fringes and the fit of an exponential decay with T_2^* enveloping the negative sine curve. (b) Hahn echo measurement: The values on the x-axis are the delay time before and after the π-pulse, therefore only half of the actual delay time between preparation and measurement. This must be taken into account when evaluating T_2^{echo}.

In the actual experiment, the frequency

$$f_{\text{ct}} = f_{\text{signal}} - f_{\text{sideband}} = 8.075\,85\,\text{GHz} - 155\,\text{MHz} = 7.920\,85\,\text{GHz}$$

of the control pulse is shifted by a small detuning $\delta f = 0.5\,\text{MHz} \ll f_{\text{ct}}$.[20] The prepared superposition state will then rotate with the frequency of the detuning around the z-axis $nd = \delta f\,\sigma_z$ on the equator of the Bloch sphere, which are the Ramsey oscillations from Sec. 5.2.2.

Due to decoherence this circular trajectory will actually be a spiral one, slowly approaching the center of the sphere. As before, measurement is along x-axis, which means acting a Y_{90}-gate and project onto the z-axis. Now, the exponential decay is the envelope of a sine oscillation. The experimental data is shown in Fig. 5.6a. Often, T_2^* will be used instead of T_2 without explicitly saying so, since T_2^* is simply a better estimate on the same physical quantity.

[20] Further conditions are that the anharmonicity $\alpha \gg \omega_{\text{rw}} = 2\pi/T_{\text{rw}}$.

5.2.6 Hahn Echo Decay Time T_2^{echo}

Due to the broadening of the control frequency, the qubit is with a range of frequencies put into a superposition, all close to similar, but still not identical. Hence, during the Ramsey oscillations, different frequency components cause decoherence. There is a way to get rid of the low frequency effects: echoing them away.

Think of an ensemble of states precessing on the equator rather than a single state. Due to broadening, each state precesses with a slightly different Larmor frequency. This certainly affects the observed coherence time of the ensemble, because the average of them all is not on the convex surface of the Bloch sphere anymore. The resultant state is below the surface.

It is possible to echo this low-frequency decoherence process away by applying a π-pulse to the system halfway through the delay. The sudden flip of the ensemble and the states, which have deferred more than others, show the same behavior, but in the opposite direction. By this means, the unwanted effects are canceled. Except for other, higher-frequency decoherence mechanisms all states of the ensemble recover the initial coherence[21]. By running the T_2^{echo} sequence, it is possible to remove low-frequency components of the decoherence. Results from the experiment are shown in Fig. 5.6b.

It should be noted that figures in this section are single runs from various cool-downs, exemplary for the respective method. For the estimate on the parameters in Tab. 4 in the chapter *Results* several experiments from the relevant cool-down were consulted.

5.3 Calibrating Quantum Gates

Before discussing the optimization of the gates, readout and control settings are shortly reviewed.

For readout, a 1500 ns squared pulse at frequency $f_{\text{ro}} = 10.626\,761\,824\,\text{GHz}$ was used[22]. This was the frequency with a ideal phase difference of π between $|g\rangle$ and $|e\rangle$ reflection coefficient, as seen in Fig. 5.7.

The readout power is notable, because it connects to the average number of photons inside the cavity. Ideally, this should be very low, but than the signal-to-noise ratio (SNR) is unfavorable. Also, above the critical photon number n_{crit} of Eq. (5.7) the assumption of the dispersive regime breaks down. It is therefore recommendable to work at a power that yields $\bar{n} \approx n_{\text{crit}}/10$.

[21] The process is well animated on the English Wikipedia article on NMR relaxation.

[22] The DAC output was at $f_{\text{DAC}} = 10.676\,761\,824\,\text{GHz}$ with a sideband frequency of $f_{\text{sb}} = -50\,\text{MHz}$.

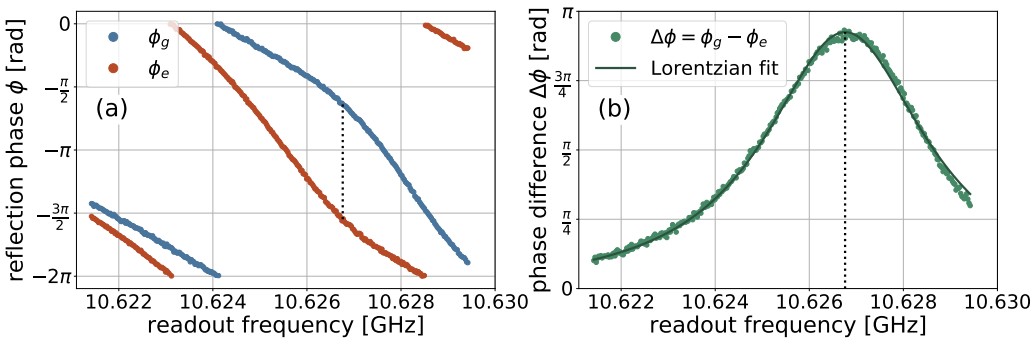

Figure 5.7: Optimization of readout frequency. (a) Phase ϕ of reflection coefficient r for the qubit in $|g\rangle$ and $|e\rangle$ state. (b) Phase difference $\Delta\phi$ with optimal point close to π at $f_{\mathrm{ro}} = 10.626\,761\,824\,\mathrm{GHz}$ (dotted line).

In the setup, up to the entry of the dilution refrigerator the signal had a power of −43 dBm, determined via DAC calibration, another −50 dB in the transmission line down to the coolest stage and a −20 dB attenuation at cryogenic level. The readout signal at the sample was hence −113 dBm.

Control pulses are modulated Gaussian pulses at qubit frequency ω_{a} of variable width σ, power and phase. In this thesis, the pulse widths are fixed at 12 ns due to hardware limitations. Distinction between $\pi/2$- and π-rotations is made on grounds of control power (see Rabi oscillations in Sec. 5.2.1).

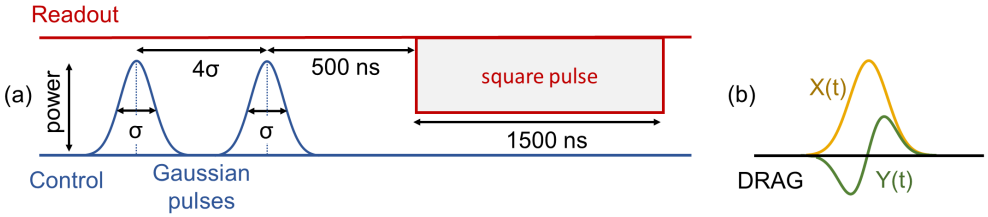

Figure 5.8: (a) Separation of control and readout pulses guarantees interference-free pulse actions. For a control pulse of width σ = 12 ns, a separation of 4σ is chosen. The gate action time t_{g} = 48 ns results. (b) To further improve short control pulses, Derivative Reduction by Adiabatic Gate (DRAG) pulses are employed, where quadrature $Y(t)$ is proportional to the derivate of $X(t)$.

Successional pulses should not interfere with each other. It is therefore advisable to leave a 4σ separation, measuring from one center to another, see Fig. 5.8a.

Increasing the number of gates can either be achieved by longer coherence

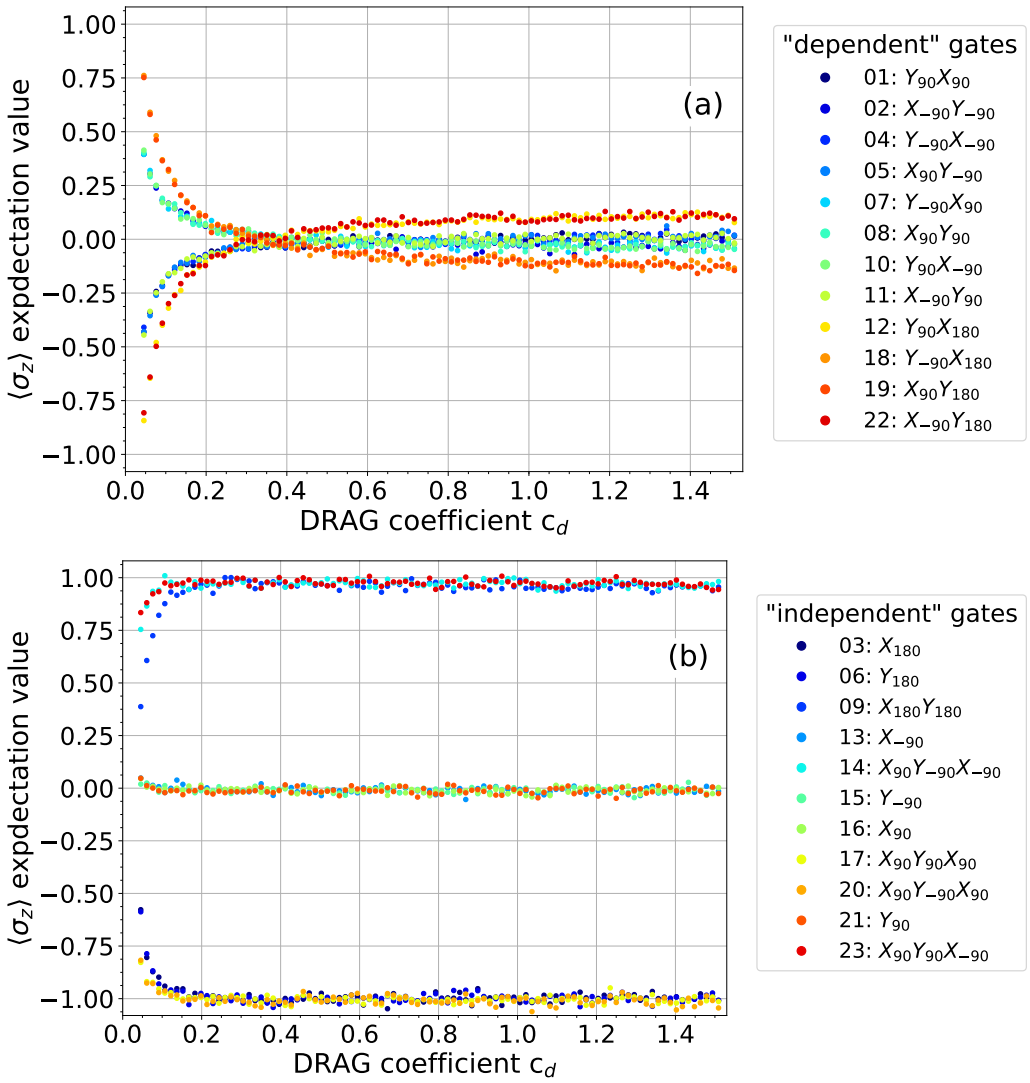

Figure 5.9: DRAG optimization. (a) Half of the 24 Clifford gates from Tab. 1 have a $1/c_\mathrm{d}$-dependence to the DRAG coeffient c_d, with an optimal point close to the anharmonicity $c_\mathrm{d} = 0.5$. For the actual experiments, individual DRAG coefficients for every Clifford gate were chosen, each optpimizing the respective gate. (b) The other half is mostly unaffected by a change of the DRAG coefficient. It was chosen to be $c_\mathrm{d} = 0.61$ for them, because analysis showed minimal fluctuation there.

times or shorter gate times. The transmon qubit exhibits non-computational levels above the qubit submanifold. The weak anharmonicity α of superconducting qubit ($\approx 2\pi \cdot 330\,\mathrm{MHz}$ here) sets a lower limit on the control pulse

width σ, because as $1/(2\pi\sigma) \approx \alpha$ the leakage into non-computational levels starts to occur. Such gate errors can be separated into amplitude and phase errors. *Virtual excitations* to higher levels above $\{|0\rangle, |1\rangle\}$ during the gate action result in *phase errors*, which are an unwanted z-rotation. *Real excitations* after the gate produce *amplitude errors*, that are leakage errors, which change the rotation axis [75, 80]. Apart from constant detuning of the control frequency from the qubit frequency, the use of Derivative Reduction by Adiabatic Gate (DRAG) pulses decrease such errors [71, 75, 80–82].

If the drive quadrature $Y(t)$ of Eq. (3.68) is chosen as the time derivative of the Gaussian in-phase component $X(t)$, schematically shown in Fig. 5.8b,

$$Y(t) = -c_\mathrm{d} \frac{\dot{X}(t)}{\alpha}, \tag{5.9}$$

with a constant c_d (optimal at $c_\mathrm{d} = 1/2$ [82, 83]), leakage errors are reduced to the order $\mathcal{O}(X^4/\alpha^3)$. This can be seen in the effective Hamiltonian of the system [81]. For the ideal c_d fast-gate actions are optimized to higher precision than is possible without the use of DRAG pulses.

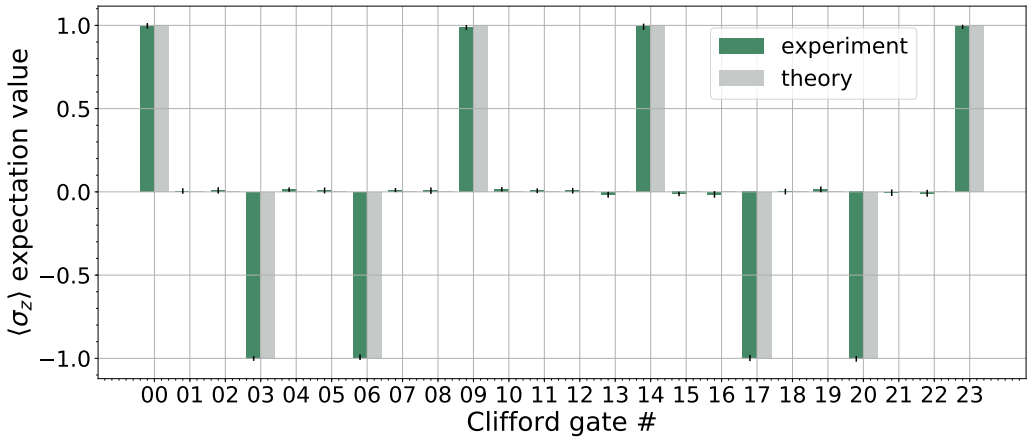

Figure 5.10: Result of the gate optimization of all Clifford gates (see Tab. 1), using DRAG pulses and gate time $t_\mathrm{g} = 48\,\mathrm{ns}$.

In Fig. 5.9, the action of all Clifford gates is shown, dependent on the DRAG coefficient. Clifford gates that yield states at the equator of the Bloch sphere, where $\langle\sigma_\mathrm{z}\rangle = 0$, are prone to be more sensitive to the DRAG coefficient than the other gates. In the experiment, individual DRAG parameters c_d for each respective gate were chosen, because a multi-parameter optimization for a single c_d did not yield satisfactory results; $c_\mathrm{d} = 0.61$ was chosen for the insensitive gates, since analysis showed least fluctations around this point.

It should be noted that DRAG pulses prove necessary at control pulse widths $\sigma < 10\,\text{ns}$. In this thesis, hardware limitations prohibited higher powers of the control pulse and therefore shorter pulses. At $\sigma = 12\,\text{ns}$ the DRAG shaping has only minor impact, as was confirmed also for this work.

The last quality certification of control pulses (pulse amplitude, DRAG coefficient), readout pulses, demodulation window and spacing between pulses, is the full Clifford gate check. In Fig. 5.10 expectation values of all 24 Clifford gates are confirmed to be close to perfect accuracy. This is the point, at which more elaborate characterization schemes become necessary to find ways to push accuracies into even smaller orders of magnitude. The results of the characterization methods are presented in the next chapter.

Chapter 6 Results

Experimental results come from ensemble measurements with $N = 10^4$ in contrast to the single-shot measurements of Sec. 7.5. The package QuTiP was used in much of the analysis [84].

Cavity resonant frequency	$\omega_\mathrm{r}/2\pi$	10.626 761 0(40) GHz
Cavity bare resonant frequency	$\omega_\mathrm{r}^\mathrm{bare}/2\pi$	10.6193(11) GHz
Cavity external losses	$\kappa_\mathrm{ext}/2\pi$	3.0312(86) MHz
Cavity internal losses	$\kappa_\mathrm{int}/2\pi$	(4.0 ± 4.0) kHz
Qubit resonant frequency	$\omega_\mathrm{a}/2\pi$	7.888 553 28(42) GHz
Qubit anharmonicity	$\alpha/2\pi$	≈ -328 MHz
Dispersive shift	$\chi/2\pi$	≈ 1.5 MHz
Single photon power	P_single	≈ -135 dBm
Critical photon number	n_crit	≈ 50
Coupling	$g/2\pi$	≈ 198 MHz
Relaxation time	T_1	(27.8 ± 2.3) µs
Dephasing time	T_2	(14.8 ± 2.0) µs
Dephasing time (Ramsey)	T_2^*	(15.1 ± 2.3) µs
Dephasing time (echo)	T_2^echo	(16.9 ± 1.8) µs
Dephasing time, beating	T_2^beating	(13.6 ± 2.1) µs
Dephasing time, beating (Ramsey)	$T_2^{*\mathrm{beating}}$	(14.0 ± 2.3) µs

Table 4: Collected parameters of the sample. Statistics on a collection of identical experiments led to the given values.

6.1 Quantum Process Tomography (QPT)

QPT was carried out for each Clifford gate, averaging over 10^5 runs for every experimental configuration. Gate fidelities are given in Fig. 6.5. The Pauli transfer matrices of the three most important Clifford gates Id, X_{90} and Y_{90} are visualized in Fig. 6.1 with average gate fidelities of ≥ 0.99.

6.1.1 Decoherence Model

QPT was also employed to confirm the decoherence model from Sec. 2.6. After a variable idle time, ranging up to 52 µs, the process that has occured

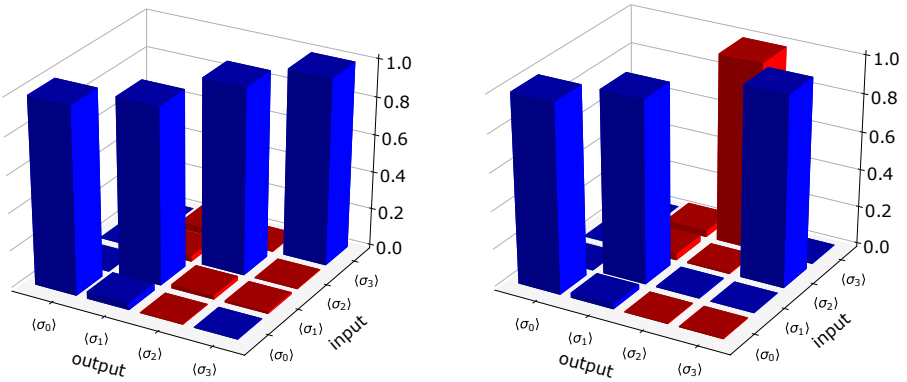

(a) Idle: $\mathcal{F} = 0.990$ (b) X_{90}: $\mathcal{F} = 0.994$

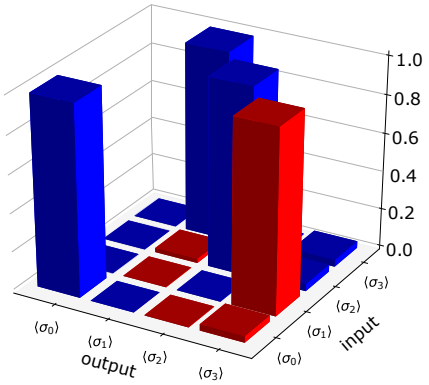

(c) Y_{90}: $\mathcal{F} = 0.991$

Figure 6.1: QPT estimate of the Hilbert-Schmidt matrix of the three Clifford gates Id, X_{90} and Y_{90} with their respective gate fidelity $\mathcal{F}$. Red bars symbolize a negative value.

was evaluated by QPT. From the χ-matrix, the average gate fidelity $\mathcal{F}^{\text{avg}}$ was calculated with Eq. (2.90) and plotted in Fig. 6.3.

The theoretical curve from the decoherence model is calculated with $T_1 = 27.33\,\mu\text{s}$ and $T_2^* = 12.28\,\mu\text{s}$, which are different values from the ones in Tab. 4, but stem from the Ramsey experiment in Fig. 6.2. Another two-level system with coherence time $T_2^{*(\text{beating})} = (12.17 \pm 0.53)\,\mu\text{s}$ couples to the qubit, modulating the Ramsey oscillation additionally. This data was taken at the day of the decoherence QPTs with several weeks distance to the majority of experiments of the work. The small errors on the coherence times in Tab. 4 must therefore be taken with utter care.

From a weak beating signal in the Ramsey measurement (Sec. 5.2.5) it was already evident that a second unknown two-level system interacted with the transmon qubit, which happens in some cool-downs by coinci-

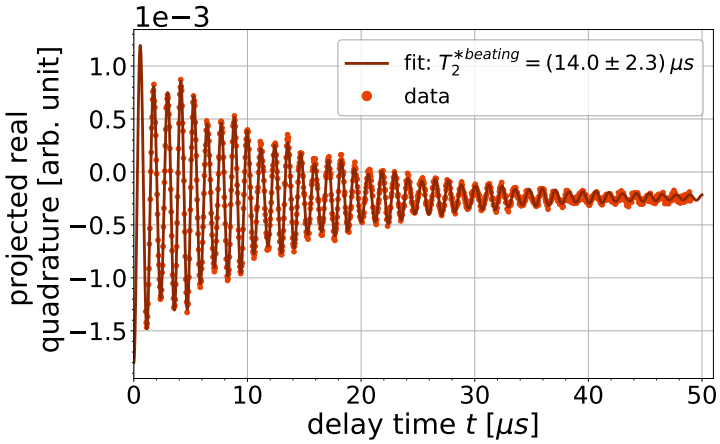

Figure 6.2: Ramsey experiment to determine the qubit coherence time $T_2^{*\text{beating}}$. Another two-level system couples to the qubit, resulting in an additional cosine modulation that is exponentially decaying with rate $(12.1 \pm 1.1)\,\mu s$.

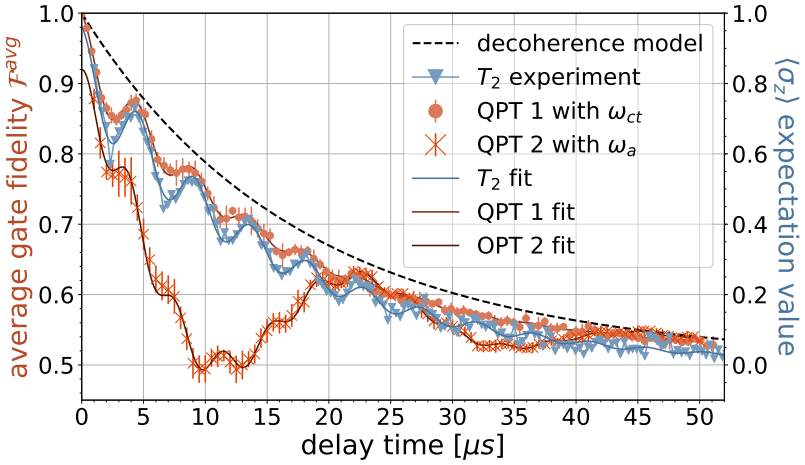

Figure 6.3: Slow Ramsey oscillation (red) from a series of QPTs with control frequency ω_{ct} that is detuned from the actual qubit frequency ω_{a}. When this effect is accounted for by $\Delta\omega = 45.57\,\text{kHz}$ (brown), the expected exponential decay shows only a small beating signal with $\omega_{\text{b}} \approx 220\,\text{kHz}$. A conventional T_2-measurement (blue) confirms the result with good precision.

dence [85]. Thus, at first, the optimization of ω_{ct} yielded a mean value of the actual qubit frequency ω_{a} and the frequency of the disrupting system $\omega_{\text{a}}^{\text{beating}}$ at $\omega_{\text{ct}} = 7.843\,553\,28(42)\,\text{GHz}$. In the experiment, this resulted in a low-frequency oscillation around the z-axis with $(43.51 \pm 0.22)\,\text{kHz}$. With a

Fourier analysis of the Ramsey oscillations the qubit frequency was found to be $\omega_a = 7.888\,553\,28(42)\,\text{GHz}$, which corrected ω_{ct} by $\Delta\omega = 45.57\,\text{kHz}$, cancelling the low-frequency oscillations as expected.

The oscillating decay of the average gate fidelity in the QPT measurement confirms the standard T_2-measurement, showing a similar oscillating decay in the $\langle\sigma_z\rangle$ expectation value. The fitting gives coherence time values of $T_2^{\text{QPT}} = 15.9\,\mu\text{s}$ and $T_2 = 15.4\,\mu\text{s}$; and beating frequencies $\omega_b^{\text{QPT}} = 219\,\text{kHz}$ and $\omega_b^{T_2} = 218\,\text{kHz}$ respectively.

6.2 Randomized Benchmarking (RB)

State-of-the-art interleaved randomized benchmarking (IRB) uses gate sequences that exceed multiple hundred gates [7, 25]. Although the sample's coherence times allow such numbers, hardware limitations in the setup (FPGA memory of only 6 µs, input pulse power) reduced it to 23 gates[23]. For standard RB (SRB) 8 different sequence lengths $m = \{2, 5, 8, 11, 14, 17, 20, 23\}$ were chosen. For each m 50 different random sequences were run experimentally, see Fig. 6.4. The same was repeated for IRB for all 24 Clifford gates, yielding the decay rates p_i and gate fidelities $\mathcal{F}_i$, depicted in Fig. 6.5.

The fidelities of IRB are constantly higher than the ones of QPT. That IRB over-estimates due to insensibility to coherent errors was recently reported in [36].

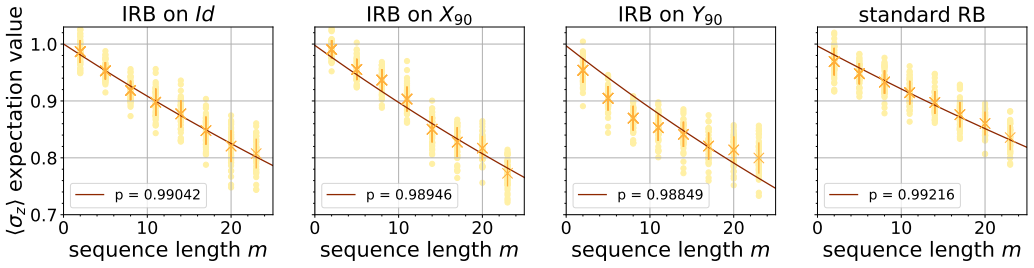

Figure 6.4: Interleaved randomized benchmarking (IRB) for Clifford gates. Out of 23, the three most important ones are shown. The reference of standard RB is shown on the right. Experimental data (yellow dots) is averaged (orange crosses) and fitted with an exponential decay (red line) for sequence lengths of up to 23.

[23] The average Clifford gate has $\bar{t}_g = 1,875 \cdot 48\,\text{ns} = 90\,\text{ns}$. If a three-fold Clifford gate is chosen for IRB, the length of the protocol is $t = m(3 \cdot 48 + 90)\text{ns} \leq 6\,\mu\text{s}$. The inequality breaks for $m = 25.6$, but because gates are chosen randomly $m = 23$ is feasible in 98% of the cases.

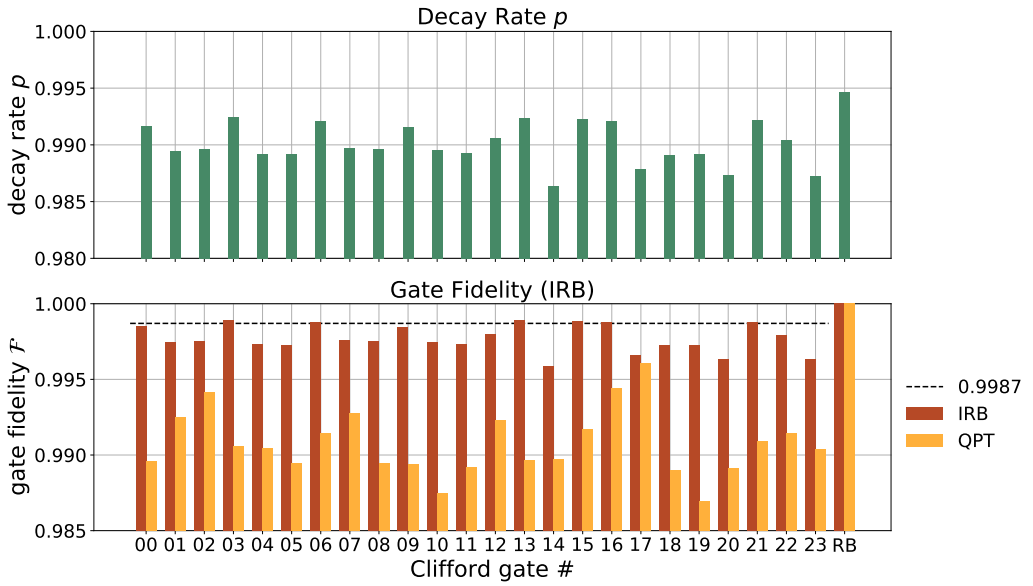

Figure 6.5: Decay rates and gate fidelities of IRB and QPT. Standard RB is the reference on the utmost right. Only few values excel the threshold of the decoherence model for $t_g = 48\,\text{ns}$.

6.3 Gate Set Tomography (GST)

The most basic GST consists of 40 experiments, each is here carried out $N = 10^6$ times. The provided python package pyGSTi [86] gives the initial linear estimate (LGST), Tab. 7, and the gauge-fixed and, due to physicality, projected estimate (PGST), Tab. 8, both given in the supplementary Sec. A.1.

The LGST estimate does not meet the condition that the first row of a Hilbert-Schmidt matrix is always $(1, 0, 0, 0)$. Nevertheless, deviations from the ideal are considerably smaller than at the other entries. The projection clearly solves this problem for the PGST estimate. In both cases, the other element of the POVM is omitted since it is exactly $\mathbb{1} - E$.

6.4 Self-Consistent Quantum Tomography (SCQT)

The SCQT consists of 49 experiments, see Fig. 2.6. SCQT estimates in the thesis were calculated using numerical codes provided by T. Sugiyama. A software package for constraint nonlinear optimization problems, called IPOPT [87], is used for solving minimization in the codes.

Fig. 6.6a shows that the β-parameter from Eq. (2.80) does not alter the results significantly for different data sizes ranging from $N = 10^3$ to 10^6,

therefore $\beta = 1$ was chosen. In the same range, the convergence behavior for $N \to \infty$ of LGST, PGST and SCQT were analyzed. Theory claims that the estimate of SCQT converges to a gauge-equivalent class of the true gate set, which clearly may not be the true gate set. The probability distributions $\mathbf{p}_i$ from SCQT, see Eq. (2.78), and the ones from LGST converge to the true, empirically determined probability distribution $\mathfrak{f}_i$. PGST's probability distribution does not necessarily converge to the true one [23, 26, 29].

The experimental results in Fig. 6.6b attest that SCQT not only converge to the experimental probability distribution, but converges faster. However, the convergence of the LGST estimate in opposition to the PGST estimate is not visible from the experiment.

For the final analysis $N = 10^6$ were chosen. The results are in Tab. 9, where deviations of up to $\mathcal{O}(10^{-1})$ from the ideal can already be found. A discussion in detail follows in the next chapter.

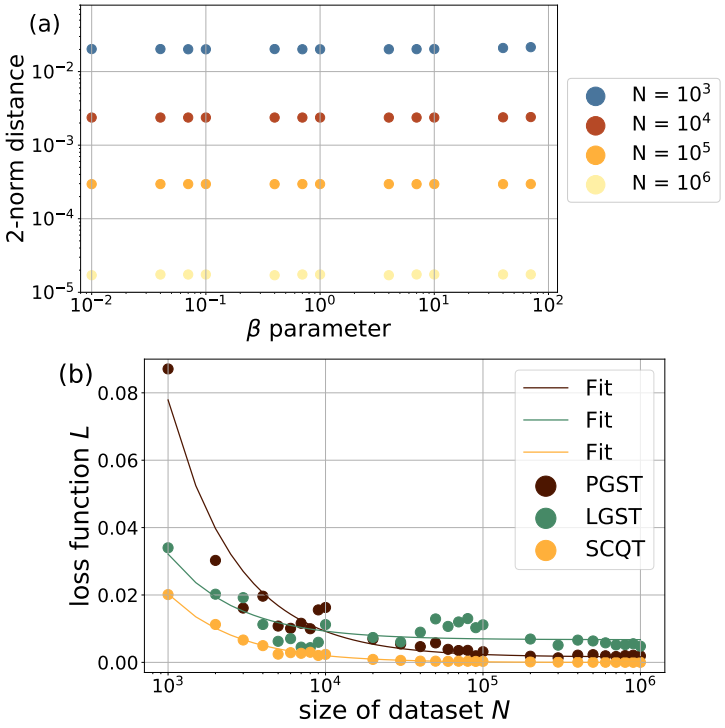

Figure 6.6: (a) Behavior of SCQT estimate with the β-parameter, which itself shows little effect on the 2-norm distance between the SCQT estimate and the experimental data from Eq. (2.82). (b) Convergence behavior of characterization methods. Experiment confirms SCQT's convergence, fails however to ratify the convergence of LGST in constrast to PGST.

Chapter 7 Discussion

In this chapter, results of various characterization methods and their derived quantities are compared to SCQT and analyzed in detail. At last, a proof-of-principle with single shot readout is provided.

7.1 Gate Fidelity $\mathcal{F}$

Basic GST and SCQT estimate only the gates Id, X_{90} and Y_{90}, thus, these three were picked for comparison from the IRB and QPT results in Fig. 6.5. With the values of T_1 and T_2^* (see Tab. 4), an upper limit of 0.9987 was calculated, caused simply by effects of decoherence in the 48 ns long gate action.

Both GST fidelities exceed the decoherence bound, where the LGST is even greater than one, hence, unreasonable. IRB produces results close to error rater of 10^{-3}, but whether conventional IRB over-estimates or really reflects gate fidelity is in question [36, 37]. QPT and SCQT values are well below that threshold and vary significantly, with SCQT continuously giving a higher estimate. It is noteworthy though that there is no reasonable explanation for a Id-gate to be less accurate than a $\pi/2$-rotation of same gate action time, as seen in the QPT results.

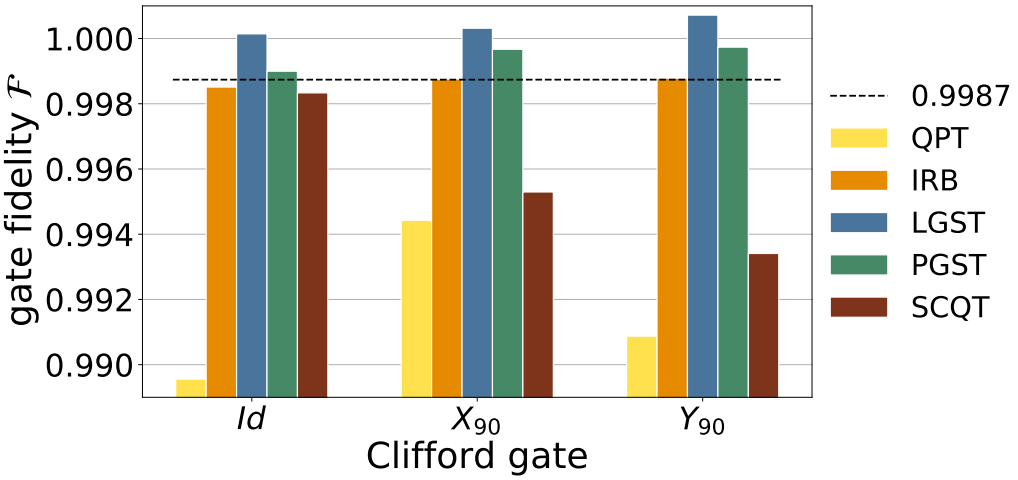

Figure 7.1: Gate fidelities of different characterization methods for Clifford gates Id, X_{90} and Y_{90}. The dashed line shows the theoretical limit for $\mathcal{F}^{\text{avg}}$ from the decoherence model for gate time $t_g = 48$ ns.

7.2 Error Generators

With the formalism from Sec. 2.7 derived expressions for T_1 and T_2 of the Id-gate are compared to the direct experimental values in Tab. 5. The accuracy is drastically mitigated, because the calculation involves the inverse of a very small number, see Eq. (2.97). Both GST methods produce unreasonable results as one includes a negative coherence time and the other one $T_2 > T_1$, which reflects previous shortcomings of the estimate in terms of gate fidelity. QPT and SCQT are closer, but still far away from quantative importance.

Direct	**QPT**	**LGST**	**PGST**	**SCQT**
$T_1 = 28\,\mu s$	$13\,\mu s$	$37\,\mu s$	$17\,\mu s$	$41\,\mu s$
$T_2^* = 15\,\mu s$	$8\,\mu s$	$(-231\,\mu s)$	$30\,\mu s$	$11\,\mu s$

Table 5: Derived coherence times from different estimates on the Id-gate.

7.3 Physicality

Gate sets were estimated by the various characterization methods and then analyzed concerning their physicality. Physicality criteria for the intial state ρ and POVM Π are described in Sec. 2.1.2; for the processes, their CJ representation from Sec. 2.4.4 was calculated and the positivity of their eigenvalues checked. The results are listed in Tab. 6.

QPT only presents estimates on the processes. These were physical. The linear GST does not result in physical gate estimates. This is not surprising, since the additional projection protocol in PGST warrants physicality. Therefore, both PGST and SCQT yield physical gate sets.

	QPT	**LGST**	**PGST**	**SCQT**
ρ	—	✓	✓	✓
Id	✓	2 EV: $-\mathcal{O}(10^{-3})$	✓	✓
X_{90}	✓	2 EV: $-\mathcal{O}(10^{-2})$	✓	✓
Y_{90}	✓	1 EV: $-\mathcal{O}(10^{-2})$	✓	✓
Π	—	✓	✓	✓

Table 6: Physicality of the estimated gate sets of quantum process tomography (QPT), linear (LGST) and projected gate set tomography (PGST), and the self-consistent quantum tomography (SCQT).

7.4 Noise Identification

IRB cannot distinguish between different errors, because it only provides a single parameter, the gate fidelity $\mathcal{F}$. SCQT estimates the whole gate set and finds the origin of error even for already high precision experiments - an invaluable information for further improvement of gate accuracy. Here, intentional amplitude damping and unitary errors were implemented and characterized with the two protocols.

Amplitude Damping. When there is additional idle time added to the gate time t_g, decoherence takes place, causing amplitude damping of the quantum state. Experiments were executed with a collection of different idle times $\{0.1t_g, 0.5t_g, 1.0t_g, 3.0t_g\}$. Results are shown in Fig. 7.2. As expected, for longer idle times, more amplitude damping is visible and lower gate fidelity is too.

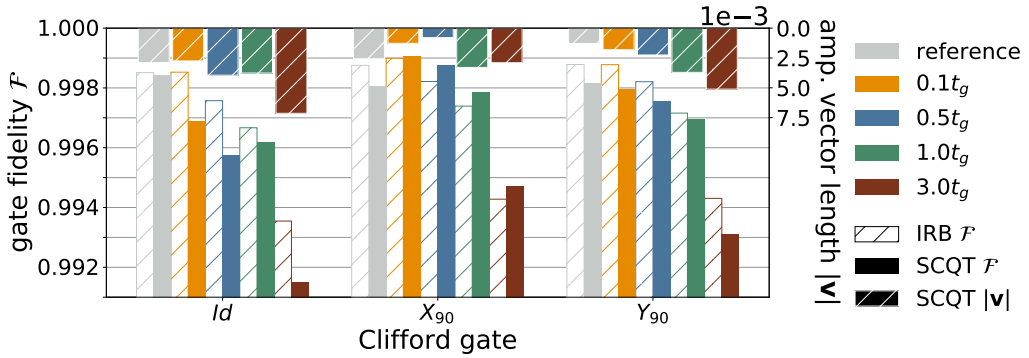

Figure 7.2: Noise identification of amplitude damping. Gate fidelities for increased idle times between gates for IRB and SCQT, testing the three gates Id, X_{90} and Y_{90}. From above, the length of the amplitude vector is depicted, showing weak correlation with the decreasing gate fidelity.

Unitary errors. They are over/under-rotations, easily implemented by a longer control pulse. In SCQT, the gates X_{90} and Y_{90} were both equipped with an extra rotation of

$$\{\pi/90, \pi/40, \pi/25, \pi/20, \pi/10\} = \{2.0°, 4.5°, 7.2°, 9.0°, 18.0°\}$$

around their respective axis, chosen with consideration of Eq. (2.99), labeled ++. The experiments were repeated for positive unitary error (= over-rotation) in X_{90} and negative unitary error (= under-rotation) in Y_{90}, which is labeld +−.

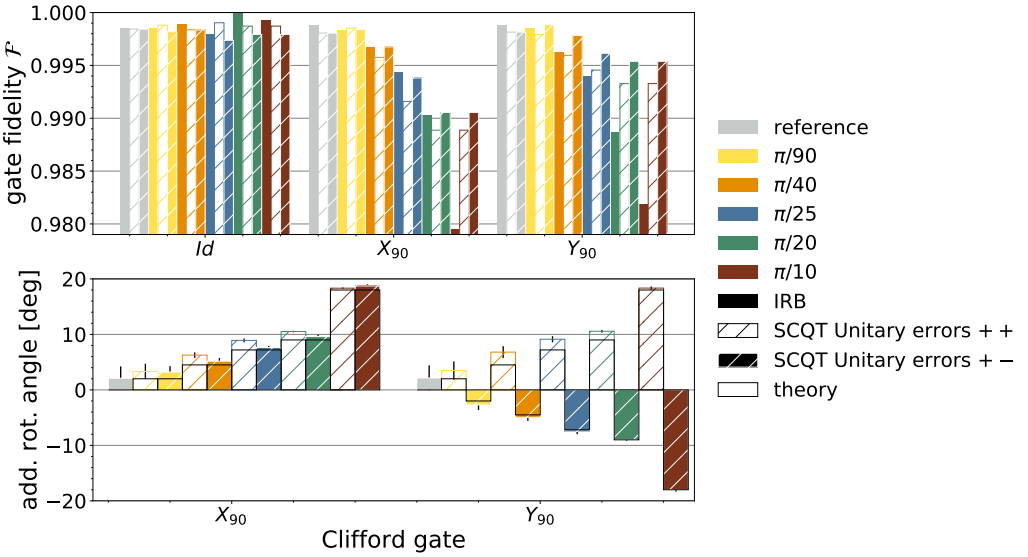

Figure 7.3: Noise identification of unitary errors. (Top) Gate fidelities for gates with unitary error, characterized by IRB and SCQT, testing the three gates Id, X_{90} and Y_{90}. (Bottom) Angles of additional rotation in experiments with intentional unitary errors. The SCQT estimate predicts the error cause well.

In IRB, $\pi/2$-rotations were given such over-rotations. Since all Clifford gates are combinations of $\pi/2$-rotations respective unitary errors trickled-down. Gate fidelities are compared in Fig. 7.3. In accordance with the expectation, bigger unitary errors led to a smaller gate fidelity and the idle gate is unaffected within statistical fluctations.

To determine the experimental angle of over-rotation, first, the axis of rotation is confirmed. Indeed, the (faulty) axis of over-rotation of the lower 3×3 submatrix of the Pauli transfer matrix is sufficiently close to the ideal axis that the approximation by the ideal one is reasonable. Second, the angles of over-rotation are evaluated, see bottom of Fig. 7.3, from where it is clear that SCQT can predict the error cause of over-rotation even for small angles.

Furthermore, SCQT predicts the angle of over/under-rotation more accurate than IRB. Even if the rotation axis and the sign of the erronous angle is assumed to be known, calculations from IRB's gate fidelity do not reproduce the angles as precisely.

If IRB gives low gate fidelity, it is impossible to infer, whether amplitude damping, unitary error or other reasons are the source. In SCQT, the gate estimates are Pauli transfer matrices, from which it is possible to deduce the origin of error.

7.5 Single Shot Proof-of-Principle

Averaged measurement is the default measurement scheme in this thesis, yet quantum information processing requires single shot measurements. This section provides evidence that averaged and single shot mode concur in their conclusions, if not quantitatively, then qualitatively.

Every experiment was repeated $N = 10^5$ times, followed by a post-selection that picked only runs, where the initial state was (non-destructively) measured to be in ground state. The reference spots of $|g\rangle$ and $|e\rangle$ in the IQ plane where determined by previous measurements, where fluctations were negligible when compared to measurement noise. After postselection each of the 49 runs maintained a statistical wealth of circa $9.3 \cdot 10^4$ datapoints. Gaussian control pulses without DRAG of 15 ns (not 12 ns as before) were employed.

The gate fidelities for the gates Id, X_{90} and Y_{90} are 0.9983, 0.9978 and 0.9972 respectively, which corresponds well to the previous values in Fig. 7.1. Concerning the physicality of the estimate, single shot SCQT reproduces the physicality of the SCQT results from Tab. 6. Thus, it is fair to judge the analysis, done on results from averaged measurements, representative for future single shot experiments.

Chapter 8 Conclusion

The novel scheme of self-consistent quantum tomography (SCQT) [26] was experimentally examined using a single superconducting qubit of transmon type in a 3D architecture. On grounds of the estimated gate set vital parameters of quantum information processing as well as measures used in validation and verification protocols were discussed. The results analyzed the agreement with the outlined decoherence model; gate fidelity; error generators and their predictive power for coherence times; the physicality of all gate set elements; and the power to distinguish between noise channels of over/under-rotation and amplitude damping as well as to quantify these errors. This was compared with results from well-established characterization methods, that are quantum process tomography (QPT), interleaved randomized benchmarking (IRB) and two variants of gate set tomography, linear (LGST) and projected (PGST).

SCQT reproduces many of the promised advantages, especially when contrasted with QPT and IRB. It provides a complete gate set of initial state, gates in question and POVM, does so without SPAM errors and is fairly easy to implement.

While GST does not meet both criteria of gauge-equivalence and physicality, SCQT fulfills them simultaneously. The experimental data confirms this. The GST package [86] offers, after years of development, a vast source of tutorials, explanations and extensions to higher orders of precision by error amplification, higher dimension of quantum systems and number of qubits. Unsurprisingly, the applied version of SCQT is the first of its generation and therefore succinct. Extensions to qutrits, multiple qubits and their crosstalk are currently in development.

As the night is dark and full of errors, sophisticated characterization protocols are needed to better understand various types of noise. Real laboratory scenerios include also non-Markovian and time-dependent noise, which have been neglected in this thesis. It will be indispensible to address them in future QCVV protocols for the rise of full-fledged quantum computing.

Chapter A Appendix

A.1 Gate set estimates from GST and SCQT

Here, the results of the gate sets from linear (LGST) and projected gate set tomography (PGST) from Sec. 6.3 as well as self-consistent quantum tomography (SCQT) from Sec. 6.4 are shown. Each of the gate sets consists of an initial state ρ, three gates G_0, G_1 and G_2, which are targetting Id, X_{90} and Y_{90}, and the POVM elements E and $\mathbb{1} - E$. For GST estimates, only E is shown, as the experimental results for $\mathbb{1} - E$ are identical with the theoretical values of this expression. In SCQT, this is not the case, which is why both elements are listed.

ρ	$\begin{pmatrix} 1 & 0 \\ 0 & 0 \end{pmatrix}$
G_0	$\begin{pmatrix} 1+\mathcal{O}(10^{-7}) & -\mathcal{O}(10^{-7}) & \mathcal{O}(10^{-6}) & -\mathcal{O}(10^{-7}) \\ -\mathcal{O}(10^{-3}) & 1+\mathcal{O}(10^{-4}) & \mathcal{O}(10^{-3}) & \mathcal{O}(10^{-3}) \\ \mathcal{O}(10^{-3}) & -\mathcal{O}(10^{-2}) & 1+\mathcal{O}(10^{-3}) & -\mathcal{O}(10^{-3}) \\ \mathcal{O}(10^{-3}) & -\mathcal{O}(10^{-4}) & -\mathcal{O}(10^{-4}) & 1-\mathcal{O}(10^{-3}) \end{pmatrix}$
G_1	$\begin{pmatrix} 1+\mathcal{O}(10^{-6}) & -\mathcal{O}(10^{-6}) & \mathcal{O}(10^{-6}) & -\mathcal{O}(10^{-6}) \\ -\mathcal{O}(10^{-4}) & 1-\mathcal{O}(10^{-3}) & -\mathcal{O}(10^{-4}) & \mathcal{O}(10^{-4}) \\ -\mathcal{O}(10^{-3}) & \mathcal{O}(10^{-3}) & -\mathcal{O}(10^{-3}) & -1+\mathcal{O}(10^{-3}) \\ \mathcal{O}(10^{-3}) & \mathcal{O}(10^{-2}) & 1+\mathcal{O}(10^{-3}) & -\mathcal{O}(10^{-3}) \end{pmatrix}$
G_2	$\begin{pmatrix} 1+\mathcal{O}(10^{-6}) & -\mathcal{O}(10^{-6}) & \mathcal{O}(10^{-6}) & -\mathcal{O}(10^{-6}) \\ -\mathcal{O}(10^{-2}) & -\mathcal{O}(10^{-2}) & -\mathcal{O}(10^{-3}) & 1+\mathcal{O}(10^{-2}) \\ \mathcal{O}(10^{-3}) & -\mathcal{O}(10^{-2}) & 1+\mathcal{O}(10^{-3}) & -\mathcal{O}(10^{-3}) \\ -\mathcal{O}(10^{-2}) & -1+\mathcal{O}(10^{-2}) & \mathcal{O}(10^{-3}) & \mathcal{O}(10^{-2}) \end{pmatrix}$
E	$\begin{pmatrix} 0.997 & 0.006+0.005i \\ 0.006-0.005i & 0.003 \end{pmatrix}$

Table 7: LGST gate set estimate.

ρ	$\begin{pmatrix} 0.998 & 0.002 - 0.005i \\ 0.002 + 0.005i & 0.002 \end{pmatrix}$
G_0	$\begin{pmatrix} 1 & 0 & 0 & 0 \\ 0 & 1 - \mathcal{O}(10^{-3}) & -\mathcal{O}(10^{-2}) & \mathcal{O}(10^{-3}) \\ 0 & -\mathcal{O}(10^{-2}) & 1 - \mathcal{O}(10^{-3}) & -\mathcal{O}(10^{-3}) \\ 0 & -\mathcal{O}(10^{-4}) & \mathcal{O}(10^{-4}) & 1 - \mathcal{O}(10^{-3}) \end{pmatrix}$
G_1	$\begin{pmatrix} 1 & 0 & 0 & 0 \\ 0 & 1 - \mathcal{O}(10^{-4}) & -\mathcal{O}(10^{-3}) & \mathcal{O}(10^{-4}) \\ 0 & -\mathcal{O}(10^{-5}) & -\mathcal{O}(10^{-3}) & -1 + \mathcal{O}(10^{-4}) \\ 0 & \mathcal{O}(10^{-3}) & 1 - \mathcal{O}(10^{-4}) & -\mathcal{O}(10^{-3}) \end{pmatrix}$
G_2	$\begin{pmatrix} 1 & 0 & 0 & 0 \\ 0 & -\mathcal{O}(10^{-3}) & -\mathcal{O}(10^{-3}) & 1 - \mathcal{O}(10^{-4}) \\ 0 & \mathcal{O}(10^{-3}) & 1 - \mathcal{O}(10^{-4}) & \mathcal{O}(10^{-3}) \\ 0 & -1 + \mathcal{O}(10^{-4}) & \mathcal{O}(10^{-3}) & -\mathcal{O}(10^{-3}) \end{pmatrix}$
E	$\begin{pmatrix} 0.999 & 0.007 - 0.001i \\ 0.007 + 0.001i & 0.001 \end{pmatrix}$

Table 8: PGST gate set estimate.

ρ	$\begin{pmatrix} 0.9993 & 0.0030+0.0014i \\ 0.0030-0.0014i & 0.0007 \end{pmatrix}$
G_0	$\begin{pmatrix} 1 & 0 & 0 & 0 \\ \mathcal{O}(10^{-4}) & 1-\mathcal{O}(10^{-3}) & \mathcal{O}(10^{-2}) & \mathcal{O}(10^{-4}) \\ \mathcal{O}(10^{-3}) & -\mathcal{O}(10^{-2}) & 1-\mathcal{O}(10^{-3}) & -\mathcal{O}(10^{-3}) \\ \mathcal{O}(10^{-3}) & \mathcal{O}(10^{-7}) & \mathcal{O}(10^{-4}) & 1-\mathcal{O}(10^{-3}) \end{pmatrix}$
G_1	$\begin{pmatrix} 1 & 0 & 0 & 0 \\ \mathcal{O}(10^{-3}) & 1-\mathcal{O}(10^{-4}) & {}^{\bigstar}\mathcal{O}(10^{-1}) & \mathcal{O}(10^{-2}) \\ -\mathcal{O}(10^{-4}) & \mathcal{O}(10^{-2}) & \mathcal{O}(10^{-3}) & -1+\mathcal{O}(10^{-3}) \\ -\mathcal{O}(10^{-3}) & -{}^{\bigstar}\mathcal{O}(10^{-1}) & 1-\mathcal{O}(10^{-3}) & \mathcal{O}(10^{-3}) \end{pmatrix}$
G_2	$\begin{pmatrix} 1 & 0 & 0 & 0 \\ \mathcal{O}(10^{-4}) & \mathcal{O}(10^{-2}) & -{}^{\bigstar}\mathcal{O}(10^{-1}) & 1-\mathcal{O}(10^{-3}) \\ -\mathcal{O}(10^{-4}) & -\mathcal{O}(10^{-2}) & 1-\mathcal{O}(10^{-2}) & {}^{\bigstar}\mathcal{O}(10^{-1}) \\ -\mathcal{O}(10^{-3}) & -1+\mathcal{O}(10^{-3}) & -\mathcal{O}(10^{-2}) & \mathcal{O}(10^{-3}) \end{pmatrix}$
E	$\begin{pmatrix} 0.99758 & 0 \\ 0 & 0.00050 \end{pmatrix}$
$\mathbb{1}-E$	$\begin{pmatrix} 0.00242 & 0 \\ 0 & 0.99950 \end{pmatrix}$

Table 9: SCQT gate set estimate. Large errors are highlighted by ${}^{\bigstar}$.

A.2 Classical Hamiltonian of Cooper Pair Box

The following calculation follows [49]. The kinetic part T of the Cooper Pair Box Lagrangian is

$$T = \frac{C_g}{2}\dot{\phi}_J^2 + \frac{C_j}{2}\dot{\phi}_J^2 = \frac{C_\Sigma}{2}\dot{\phi}_J^2, \tag{A.1}$$

where $C_\Sigma = C_g + C_j$ is the total island capacitance and ϕ_J is the node flux variable.

The potential term U in the Lagrangian includes the Josephson term and the external source energy. The latter is the voltage V_g times the charge on the supply-side of the capacitor. This charge can be written as the voltage across the gate capacitor $-\dot{\phi}_J$ times the gate capacitance C_g

$$U = -E_J \cos\delta + V_g C_g \dot{\phi}_J. \tag{A.2}$$

The conjugate momentum is the charge in the island plus an effective offset charge

$$Q_J = \frac{\partial \mathcal{L}}{\partial \dot{\phi}_J} = C_\Sigma \dot{\phi}_J + V_g C_g. \tag{A.3}$$

It follows that

$$\mathcal{H} = Q_J \dot{\phi}_J - \mathcal{L} = \frac{(Q_J - C_g V_g)^2}{2C_\Sigma} - E_J \cos\delta. \tag{A.4}$$

Chapter 9 References

[1] L. K. Grover. A fast quantum mechanical algorithm for database search. In *Proceedings of the 28th Annual ACM Symposium on Theory of Computing*, STOC '96, pages 212–219, New York, NY, USA, 1996.

[2] P. W. Shor. Polynomial-time algorithms for prime factorization and discrete logarithms on a quantum computer. *SIAM J. Comput.*, 26(5):1484–1509, 1997.

[3] R. Feynman. Simulating physics with computers. *Int. J. Theor. Phys.*, 21, 1982 (Online access: 23.07.2018).

[4] S. Lloyd. Universal quantum simulation. *Science*, 273:1073–1078, 1996.

[5] I. M. Georgescu, S. Ashhab, and F. Nori. Quantum simulation. *Rev. Mod. Phys.*, 86:153–185, 2014.

[6] R. Jozsa. Panel discussion: Approximate quantum computing: From advantage to applications. *THINK Q Conference*, 2017.

[7] R. Barends, J. Kelly, A. Megrant, A. Veitia, D. Sank, E. Jeffrey, T. C. White, J. Mutus, A. G. Fowler, B. Campbell, Y. Chen, Z. Chen, B. Chiaro, A. Dunsworth, C. Neill, P. O'Malley, P. Roushan, A. Vainsencher, J. Wenner, A. N. Korotkov, A. N. Cleland, and J. M. Martinis. Superconducting quantum circuits at the surface code threshold for fault tolerance. *Nature*, 508:500–503, 2014.

[8] U.S. Army Contracting Command Aberdeen Proving Ground RTP Division, U.S. Army Research Office (ARO), and National Security Agency (NSA). Research in quantum computing. *Broad Agency Announcement (BAA), W911NF-13-R-0010*, 2013 (Online access: 23.07.2018).

[9] S. Lloyd, D. Englund, K. Klemio, and J. Zeigler. Future directions of quantum information processing: A workshop on the emerging science and technology of quantum computation, communication, and measurement. 2016 (Online access: 23.07.2018).

[10] U. Fano. Description of states in quantum mechanics by density matrix and operator techniques. *Rev. Mod. Phys.*, 29:74–93, 1957.

[11] D. T. Smithey, M. Beck, M. G. Raymer, and A. Faridani. Measurement of the wigner distribution and the density matrix of a light mode using optical homodyne tomography: Application to squeezed states and the vacuum. *Phys. Rev. Lett.*, 70:1244–1247, 1993.

[12] D. Leibfried, D. M. Meekhof, B. E. King, C. Monroe, W. M. Itano, and D. J. Wineland. Experimental determination of the motional quantum state of a trapped atom. *Phys. Rev. Lett.*, 77:4281–4285, 1996.

[13] Z. Hradil. Quantum-state estimation. *Phys. Rev. A*, 55:R1561–R1564, 1997.

[14] K. Banaszek, G. M. D'Ariano, M. G. A. Paris, and M. F. Sacchi. Maximum-likelihood estimation of the density matrix. *Phys. Rev. A*, 61:010304, Dec.

[15] I. L. Chuang and M. A. Nielsen. Prescription for experimental determination of the dynamics of a quantum black box. *J. Mod. Opt.*, 44(11-12):2455–2467, 1997.

[16] J. F. Poyatos, J. I. Cirac, and P. Zoller. Complete characterization of a quantum process: The two-bit quantum gate. *Phys. Rev. Lett.*, 78:390–393, 1997.

[17] A. Luis and L. L. Sánchez-Soto. Complete characterization of arbitrary quantum measurement processes. *Phys. Rev. Lett.*, 83:3573–3576, 1999.

[18] J. Emerson, R. Alicki, and K. Zyczokoski. Scalable noise estimation with random unitary operators. *J. Opt. B*, 7, 2005.

[19] J. Emerson, M. Silva, O. Moussa, C. Ryan, M. Laforest, J. Baugh, D. G. Cory, and R. Laflammes. Symmetrized characterization of noisy quantum processes. *Science*, 317(5846):1893–1896, 2007.

[20] E. Knill, D. Leibfried, R. Reichle, J. Britton, R. B. Blakestad, J. D. Jost, C. Langer, R. Ozeri, S. Seidelin, and D. J. Wineland. Randomized benchmarking of quantum gates. *Phys. Rev. A*, 77:012307, 2008.

[21] E. Magesan, J. M. Gambetta, and J. Emerson. Scalable and robust randomized benchmarking of quantum processes. *Phys. Rev. Lett.*, 106:180504, 2011.

[22] E. Magesan, J. M. Gambetta, and J. Emerson. Characterizing quantum gates via randomized benchmarking. *Phys. Rev. A*, 85:042311, 2012.

[23] R. Blume-Kohout, J. K. Gamble, E. Nielsen, J. Mizrahi, J. D. Sterk, and P. Maunz. Robust, self-consistent, closed-form tomography of quantum logic gates on a trapped ion qubit. *arXiv preprint: 1310.4492*, 2013.

[24] D. Greenbaum. Introduction to quantum gate set tomography. *arXiv: 1509.02921*, 2015.

[25] R. Blume-Kohout, J. K. Gamble, E. Nielsen, K. Rudinger, J. Mizrahi, K. Fortier, and P. Maunz. Demonstration of qubit operations below a rigorous fault tolerance threshold with gate set tomography. *Nat. Comm.*, 8(14485), 2017.

[26] T. Sugiyama, S. Imori, and F. Tanaka. Reliable characterization of super-accurate quantum operations. *arXiv preprint: 1806.02696*, 2018.

[27] D. P. DiVincenzo. The physical implementation of quantum computation. *Fortschritte der Physik*, 48(9-11):771–783, 2000.

[28] M. A. Nielsen and I. L. Chuang. *Quantum Computation and Quantum Information: 10th Anniversary Edition*. Cambridge University Press, New York, NY, USA, 10th edition, 2011.

[29] R. J. Blume-Kohout, J. K. Gamble, E. Nielsen, P. L. W. Maunz, R. L. Scholten, and K. M. Rudinger. Turbocharging quantum tomography. *Sandia National Laboratories Public Release*, 2015 (Online access: 28.07.2018).

[30] D. Gottesmann and I. L. Chuang. Demonstrating the viability of universal quantum computation using teleportation and single-qubit operations. *Nature*, 402:390–393, 1999.

[31] E. Knill. Quantum computing with realistically noisy devices. *Nature*, 434:39–44, 2005.

[32] R. Raussendorf, J. Harrington, and K. Goyal. Topological fault-tolerance in cluster state quantum computation. *New J. Phys.*, 9(6):199, 2007.

[33] D. P. DiVincenzo. Fault-tolerant architectures for superconducting qubits. *Phys. Scr.*, 2009(T137):014020, 2009.

[34] G. Torlai, G. Mazzola, J. Carrasquilla, M. Troyer, R. Melko, and G. Carleo. Neural-network quantum state tomography. *Nat. Phys.*, 14:447–450, 2018.

[35] S. T. Merkel, J. M. Gambetta, J. A. Smolin, S. Poletto, A. D. Córcoles, B. R. Johnson, C. A. Ryan, and M. Steffen. Self-consistent quantum process tomography. *Phys. Rev. A*, 87:062119, 2013.

[36] T. Proctor, K. Rudinger, K. Young, M. Sarovar, and R. Blume-Kohout. What randomized benchmarking actually measures. *Phys. Rev. Lett.*, 119:130502, 2017.

[37] J. Qi and H. K. Ng. Randomized benchmarking does not measure average infidelity of gates. *arXiv preprint: 1805.10622*, 2018.

[38] S. Kimmel, M. P. da Silva, C. A. Ryan, B. R. Johnson, and T. Ohki. Robust extraction of tomographic information via randomized benchmarking. *Phys. Rev. X*, 4:011050, 2014.

[39] A. Carignan-Dugas, J. J. Wallman, and J. Emerson. Characterizing universal gate sets via dihedral benchmarking. *Phys. Rev. A*, 92:060302, 2015.

[40] Y. Suzuki, K. Fujii, and M. Koashi. Efficient simulation of quantum error correction under coherent error based on the nonunitary free-fermionic formalism. *Phys. Rev. Lett.*, 119:190503, 2017.

[41] H.-J. Briegel and B.-G. Englert. Quantum optical master equations: The use of damping bases. *Phys. Rev. A*, 47(3311), 1993.

[42] K. L. Geerlings. Improving coherence of superconducting qubits and resonators. *Yale University Doctoral Thesis*, 2013.

[43] W. Knight. IBM raises the bar with a 50-qubit quantum computer. *MIT Technology Review*, 2017 (Online access: 31.07.2018).

[44] C. M. Quintana, Yu Chen, D. Sank, A. G. Petukhov, T. C. White, Dvir Kafri, B. Chiaro, A. Megrant, R. Barends, B. Campbell, Z. Chen, A. Dunsworth, A. G. Fowler, R. Graff, E. Jeffrey, J. Kelly, E. Lucero, J. Y. Mutus, M. Neeley, C. Neill, P. J. J. O'Malley, P. Roushan, A. Shabani, V. N. Smelyanskiy, A. Vainsencher, J. Wenner, H. Neven, and John M. Martinis. Observation of classical-quantum crossover of $1/f$ flux noise and its paramagnetic temperature dependence. *Phys. Rev. Lett.*, 118:057702, 2017.

[45] S. Kono, K. Koshino, Y. Tabuchi, A. Noguchi, and Y. Nakamura. Quantum non-demolition detection of an itinerant microwave photon. *Nat. Phys.*, 2018.

[46] M. H. Devoret and R. J. Schoelkopf. Superconducting circuits for quantum information: An outlook. *Science*, 339(6124):1169–1174, 2013.

[47] M. H. Devoret, A. Wallraff, and J. M. Martinis. Superconducting qubits: A short review. *arXiv: cond-mat/0411174*, 2008.

[48] J. Koch, T. M. Yu, J. M. Gambetta, A. A. Houck, D. I. Schuster, J. Majer, A. Blais, M. H. Devoret, S. M. Girvin, and R. J. Schoelkopf. Charge-insensitive qubit design derived from the cooper pair box. *Phys. Rev. A*, 76:042319, 2007.

[49] S. Bader. The transmon qubit. *Unpublished term paper*, 2013 (Online access: 05.08.2018).

[50] J. Fink. Quantum nonlinearities in strong coupling circuit QED. *ETH Zurich Doctoral Thesis*, 2010.

[51] S. M. Girvin. Circuit qed: Supercondcuting qubits coupled to microwave photons. *Proceedings of the 2011 Les Houches Summer School (unpublished)*, 2011.

[52] E. Thuneberg. Quantum optics in electrical circuits. *University of Oulu Lecture Notes (unpublished)*, 2017.

[53] W. D. Oliver and P. B. Welander. Materials in superconducting quantum bits. *MRS Bulletin*, 38(10):816–825, 2013.

[54] L. S. Bishop. Circuit quantum electrodynamics. *Yale University Doctoral Thesis*, 2010.

[55] R. Fazio, V. F. Gantmakher, and Y. Imry. New directions in mesoscopic physics (towards nanoscience). *Springer*, 2003.

[56] J. Majer, J. M. Chow, J. M. Gambetta, J. Koch, B. R. Johnson, J. A. Schreier, J. Frunzio, D. I. Schuster, A. A. Houck, A. Walraff, A. Blais, M. H. Devoret, S. M. Girvin, and R. J. Schoelkopf. Coupling superconducting qubits via a cavity bus. *Nature*, 449:443–447, 2007.

[57] L. DiCarlo, J. Chow, J. M. Gambetta, L. S. Bishop, B. R. Johnson, D. Schuster, J. Majer, A. Blais, L. Frunzio, S. Girvin, and R. J. Schoelkopf. Demonstration of two-qubit algorithms with a superconducting quantum processor. *Nature*, 460:240–4, 2009.

[58] D. A. Rodrigues. Superconducting charge qubits. *University of Bristol Doctoral Thesis*, 2003.

[59] D. Vion, A. Aassime, A. Cottet, P. Joyez, H. Pothier, C. Urbina, D. Esteve, and M. H. Devoret. Manipulating the quantum state of an electrical circuit. *Science*, 296(5569):886–889, 2002.

[60] D. V. Averin, A. B. Zorin, and K. K. Likharev. Bloch oscillations in small josephson junctions. *Zh. Eksp. Teor. Fiz.*, 88:692–703, 1985 (Online access: 27.07.2018).

[61] S. Haroche and J.-M. Raimond. *Exploring the Quantum. Atoms, Cavities and Photons.* Oxford University Press, 2006.

[62] C. Cohen-Tannoudji, J. Dupont-Roc, and G. Grynberg. Atom-photon interactions: Basic processes and applications. *Wiley*, 1998.

[63] M. O. Scully and M. S. Zubairy. Quantum optics. *Amer. J. Phys.*, 67(7):648–648, 1999.

[64] Y. Yamamoto and A. Imamoglu. Mesoscopic quantum optics. *ADS*, 1999.

[65] Y. Wu and X. Yang. Strong-coupling theory of periodically driven two-level systems. *Phys. Rev. Lett.*, 98:013601, 2007.

[66] K. Fujii. Introduction to the rotating wave approximation (rwa): Two coherent oscillations. *J. Mod. Phys.*, pages 2042–2058, 2017.

[67] E. T. Jaynes and F. W. Cummings. Comparison of quantum and semiclassical radiation theories with application to the beam maser. *Proceedings of the IEEE*, 51(1):89–109, 1963.

[68] A. Blais, R.-S. Huang, A. Wallraff, S. M. Girvin, and R. J. Schoelkopf. Cavity quantum electrodynamics for superconducting electrical circuits: An architecture for quantum computation. *Phys. Rev. A*, 69:062320, 2004.

[69] D. Schuster, A. A. Houck, J. A. Schreier, A. Wallraff, J. M. Gambetta, A. Blais, L. Frunzio, J. Majer, B. Johnson, M. H. Devoret, S. M. Girvin, and R. J. Schoelkopf. Resolving photon number states in a superconducting circuit. *Nature*, 445:515–518, 2007.

[70] D. Lachance-Quirion, Y. Tabuchi, S. Ishino, A. Noguchi, T. Ishikawa, R. Yamazaki, and Y. Nakamura. Resolving quanta of collective spin excitations in a millimeter-sized ferromagnet. *Sc. Adv.*, 3(7), 2017.

[71] M. D. Reed. Entanglement and quantum error correction with superconducting qubits. *Yale University Doctoral Thesis*, 2013.

[72] J. M. Gambetta, A. Blais, D. I. Schuster, A. Wallraff, L. Frunzio, J. Majer, M. H. Devoret, S. M. Girvin, and R. J. Schoelkopf. Qubit-photon interactions in a cavity: Measurement-induced dephasing and number splitting. *Phys. Rev. A*, 74:042318, 2006.

[73] A. Blais, J. M. Gambetta, A. Wallraff, D. I. Schuster, S. M. Girvin, M. H. Devoret, and R. J. Schoelkopf. Quantum-information processing with circuit quantum electrodynamics. *Phys. Rev. A*, 75:032329, 2007.

[74] D. Lachance-Quirion. Dispositifs quantiques hybrides basés sur les systèmes de spins et les circuits supraconducteurs. *Université de Sherbrooke Doctoral Thesis*, 2018.

[75] J. Chow, L. DiCarlo, M. J. Gambetta, F. Motzoi, L. Frunzio, S. Girvin, and J. R. Schoelkopf. Optimized driving of superconducting artificial atoms for improved single-qubit gates. *Phys. Rev. A*, 82(040305), 2010.

[76] D. Schuster. Circuit quantum electrodynamics. *Yale University Doctoral Thesis*, 2007.

[77] L. Essen and J. V. L. Parry. An atomic standard frequency and time interval: A caesium resonator. *Nature*, 176:280–282, 1955.

[78] H. Paik, D. I. Schuster, L. S. Bishop, G. Kirchmair, G. Catelani, A. P. Sears, B. R. Johnson, M. J. Reagor, L. Frunzio, L. I. Glazman, S. M. Girvin, M. H. Devoret, and R. J. Schoelkopf. Observation of high coherence in josephson junction qubits measured in a three-dimensional circuit qed architecture. *Phys. Rev. Lett.*, 107:240501, 2011.

[79] Quantum Research Team IBM. Quantum information software kit tutorial: 3, qcvv.relaxation and decoherence.ipynb. 2017.

[80] Z. Chen, J. Kelly, C. Quintana, R. Barends, B. Campbell, Y. Chen, B. Chiaro, A. Dunsworth, A. Fowler, E. Lucero, E. Jeffrey, A. Megrant, J. Mutus, M. Neeley, C. Neill, J. J. P. O'Malley, P. Roushan, D. Sank, A. Vainsencher, and J. M. Martinis. Measuring and suppressing quantum state leakage in a superconducting qubit. *Phys. Rev. Lett.*, 116, 2015.

[81] F. Motzoi, J. M. Gambetta, P. Rebentrost, and K. F. Wilhelm. Simple pulses for elimination of leakage in weakly nonlinear qubits. 103:110501, 2009.

[82] E. Lucero, J. Kelly, R. C. Bialczak, M. Lenander, M. Mariantoni, M. Neeley, A. D. O'Connell, D. Sank, H. Wang, M. Weides, J. Wenner, T. Yamamoto, A. N. Cleland, and J. M. Martinis. Reduced phase error through optimized control of a superconducting qubit. *Phys. Rev. A*, 82:042339, 2010.

[83] J. M. Martinis and M. R. Geller. Fast adiabatic qubit gates using only σ_z control. *Phys. Rev. A*, 90:022307, 2014.

[84] J.R. Johansson, P.D. Nation, and F. Nori. Qutip 2: A python framework for the dynamics of open quantum systems. *Comp. Phys. Comm.*, 184(4):1234 – 1240, 2013.

[85] S. Gustavsson, F. Yan, G. Catelani, J. Bylander, A. Kamal, J. Birenbaum, D. Hover, D. Rosenberg, G. Samach, A. P. Sears, S. J. Weber, J. L. Yoder, J. Clarke, A. J. Kerman, F. Yoshihara, Y. Nakamura, T. P. Orlando, and W. D. Oliver. Suppressing relaxation in superconducting qubits by quasiparticle pumping. *Science*, 354(6319):1573–1577, 2016.

[86] Erik, J. Saldyt, L. Gross, kmrudin, T. Scholten, pmaunz, tjproct, R. Blume-Kohout, pyIonControl, and D. Nadlinger [*sic*]. pygstio/pygsti: Version 0.9.4.4, 2018.

[87] R. Wächter and L. T Biegler. On the implementation of an interior-point filter line-search algorithm for large-scale nonlinear programming. *Math. Program.*, pages 25–27, 2006.